

# Development of a test DAQ system for the CMS Phase-2 outer tracker upgrade

## Dissertation

zur Erlangung des Doktorgrades

an der Fakultät für Mathematik, Informatik und Naturwissenschaften

Fachbereich Physik

der Universität Hamburg

vorgelegt von

**Mykyta Haranko**





## Eidesstattliche Versicherung

Hiermit versichere ich an Eides statt, die vorliegende Dissertationsschrift selbst verfasst und keine anderen als die angegebenen Hilfsmittel und Quellen benutzt zu haben. Die eingereichte schriftliche Fassung entspricht der auf dem elektronischen Speichermedium. Die Dissertation wurde in der vorgelegten oder einer ähnlichen Form nicht schon einmal in einem früheren Promotionsverfahren angenommen oder als ungenügend beurteilt.

Hamburg, den 11.11.2019

Mykyta Haranko

Gutachter der Dissertation:

Prof. Dr. Elisabetta Gallo  
Dr. Andreas Mußgiller

Zusammensetzung der Prüfungskommission:

Prof. Dr. Elisabetta Gallo  
Prof. Dr. Erika Garutti  
Dr. Andreas Mußgiller  
Dr. Carsten Niebuhr  
Prof. Dr. Daniela Pfannkuche

Vorsitzender der Prüfungskommission:

Prof. Dr. Daniela Pfannkuche

Datum der Disputation:

09.01.2020

Vorsitzender Fach-Promotionsausschusses PHYSIK: Prof. Dr. Günter Hans Walter Sigl

Leiter des Fachbereichs PHYSIK:

Prof. Dr. Wolfgang Hansen

Dekan der Fakultät MIN:

Prof. Dr. Heinrich Graener





## **Abstract**

The CMS detector at the LHC is foreseen to experience a major upgrade in order to cope with increased radiation flux due to the high-luminosity operation phase of the accelerator. The CMS tracker will be replaced completely, introducing a new module concept in the outer part of the subsystem, which will exploit the strong magnetic field inside the CMS detector to select high transverse momentum particles locally and send the corresponding information to the triggering system thus enhancing the efficiency of the latter.

In order to allow for module prototyping and production testing, an intermediate DAQ system, referred to as  $\mu$ DTC, was developed in the scope of this thesis. The system allows for prototype configuration, control, monitoring and read-out, and provides all the necessary infrastructure for the module qualification. This thesis describes the upgrade project with a focus on the existing module prototypes and the structure of the FPGA firmware developed for the  $\mu$ DTC. A sequence of test beam measurement campaigns was carried out using the aforementioned DAQ system, and the results obtained from two of them are described in detail in the text.



## **Zusammenfassung**

In den kommenden Jahren wird der Large Hadron Collider aufgerüstet und der sogenannte Hochluminositätsbetrieb beginnen. Aufgrund der erhöhten Strahlenbelastung und Teilchenzahldichten ist geplant ebenfalls alle Experimente entsprechend zu erweitern, damit sie den neuen Bedingungen gewachsen sind. So wird der Spurdetektor des CMS Experiments vollständig ersetzt, wobei ein neues Modulkonzept in der äußeren Region dieses Detektors zum Einsatz kommen wird, um Teilchen mit hohem Transversalimpuls bereits auf dem Modul zu selektieren und die entsprechende Information an das Triggersystem weiterzuleiten.

Um die Prototypenentwicklung und das Testen der Module während der Massenproduktion zu ermöglichen, wurde als Zwischenstufe im Rahmen der vorliegenden Arbeit ein Datenerfassungssystem mit dem Namen  $\mu$ DTC entwickelt. Dieses System erlaubt es, Prototypen zu konfigurieren, zu überwachen und auszulesen. Des Weiteren stellt das System die notwendige Infrastruktur zur Bestimmung der Qualität der Module zur Verfügung. Die vorliegende Arbeit beschreibt das Upgrade des CMS Spurdetektors und befasst sich dabei sowohl mit den bereits existierenden Modulprototypen, als auch mit der Struktur der FPGA Firmware, die für das  $\mu$ DTC entwickelt wurde. Eine Reihe von Teststrahlmessungen wurde durchgeführt, bei denen das zugesandte Datenerfassungssystem benutzt wurde. Die Resultate zweier dieser Teststrahlmessungen werden im Detail beschrieben.



## **Dedication**

I dedicate this thesis to my beloved grandfather, for whom my education has always been something special. Your personal contribution undoubtedly brought me to this moment.



# Contents

|   |           |
|---|-----------|
| <b>Introduction</b>   | <b>1</b>  |
| <b>1. Particle Physics at the LHC</b>                         | <b>3</b>  |
| 1.1. The Standard Model of Particle Physics . . . . .         | 3         |
| 1.2. Experimental Particle Physics . . . . .                  | 5         |
| 1.3. The Large Hadron Collider . . . . .                      | 6         |
| 1.4. The CMS Experiment at the LHC . . . . .                  | 8         |
| 1.5. Silicon Tracking Detectors . . . . .                     | 10        |
| 1.5.1. Basic Concepts . . . . .                               | 11        |
| 1.5.2. The Silicon Tracker of the CMS Detector . . . . .      | 17        |
| <b>2. The High Luminosity LHC</b>                             | <b>23</b> |
| 2.1. Accelerator Upgrade . . . . .                            | 24        |
| 2.2. CMS Phase-2 Upgrade . . . . .                            | 26        |
| 2.3. Outer Tracker Upgrade . . . . .                          | 27        |
| <b>3. <math>\mu</math>DTC System Design</b>                   | <b>35</b> |
| 3.1. Module Prototypes . . . . .                              | 35        |
| 3.2. Structure of the Read-out and Control System . . . . .   | 38        |
| 3.3. The FC7 Board . . . . .                                  | 39        |
| 3.4. Digital Design . . . . .                                 | 41        |
| 3.5. Resource Utilisation . . . . .                           | 47        |
| 3.6. Software . . . . .                                       | 50        |
| <b>4. Beam Tests at the DESY-II Synchrotron</b>               | <b>53</b> |
| 4.1. The DESY-II Facility . . . . .                           | 53        |
| 4.2. Beam Test Setup . . . . .                                | 55        |
| 4.2.1. Beam Telescope . . . . .                               | 56        |
| 4.2.2. Timing Reference . . . . .                             | 57        |
| 4.2.3. Triggering and Read-out . . . . .                      | 58        |
| 4.3. Data Acquisition Software . . . . .                      | 58        |
| 4.4. Offline Track Reconstruction and Data Analysis . . . . . | 59        |
| <b>5. Results of the Test Beam Measurements</b>               | <b>65</b> |
| 5.1. 2S Mini-Module Test Beam . . . . .                       | 65        |
| 5.1.1. Module and Test Setup Description . . . . .            | 65        |

|  |            |
|--|------------|
| 5.1.2. Calibration . . . . .                       | 66         |
| 5.1.3. Results . . . . .                           | 69         |
| 5.1.4. Summary . . . . .                           | 77         |
| 5.2. MaPSA Test Beam . . . . .                     | 78         |
| 5.2.1. Module and Test Setup Description . . . . . | 79         |
| 5.2.2. Calibration . . . . .                       | 79         |
| 5.2.3. Results . . . . .                           | 80         |
| 5.2.4. Summary . . . . .                           | 86         |
| <b>Summary and Outlook</b>                         | <b>87</b>  |
| <b>A. TLU Interface</b>                            | <b>89</b>  |
| <b>List of Acronyms</b>                            | <b>93</b>  |
| <b>Bibliography</b>                                | <b>97</b>  |
| <b>Acknowledgements</b>                            | <b>105</b> |



# Introduction

In 1969 Clayton P. Alderfer proposed the Existence, Relatedness and Growth (ERG) theory of human needs [1]. It defines three groups of human motivators with transitions amongst them. The groups have a certain hierarchy: once basic existence needs were satisfied, a person becomes more motivated in satisfying social needs, while the motivation for the personal growth becomes dominant thereafter. Presently, people are balancing between the needs for social and personal growth. A person experiences needs for cognition, aesthetic satisfaction and continuous self-improvement. The desire to learn, study and research grows significantly, and an interest in exploring the surrounding world appears. Exploration and study of nature led to incredible technological developments in the past centuries. This, in turn, provided the possibility to extend the knowledge about nature. Stimulation of this progress loop becomes essential for the evolution processes.

The continuous development of human technology led to the invention of the possibility of accelerating elementary particles around a century ago, with present technologies allowing to reach high energies and collide particles with matter or other accelerated particles. The kinetic energy of such collision processes is available for generation of new particles, allowing to use accelerators to study the inner structure of matter or elementary particles.

One of such experimental tools is the Large Hadron Collider (LHC) [2], which allows to accelerate protons to unprecedented energies of up to approximately 7 TeV. Collisions of two proton beams with these energies are studied using several experiments located around the LHC ring, with one of these experiments being the Compact Muon Solenoid (CMS) [3]. The experiment is comprised of complex detecting systems surrounding the particle interaction point and allows to detect and study byproducts of the particle collisions.

The discovery potential of accelerator-based experiments depends on the energy available for generation of new particles, the rate of particle collisions and the efficiency of the detection systems. Each physical process has a certain occurrence probability, and with the LHC being not the first ever built accelerator, a large number of experiments have already been performed using other accelerators. Most of the processes occurring at relatively low energy and having relatively large occurrence probability have been studied and, as a result, the focus of the LHC are truly rare physics events happening at high energy. One of the most intensively studied nowadays objects is the Higgs boson. The existing accelerator complex allows to create approximately one Higgs boson per second in proton-proton collisions [4]. The Higgs boson can be observed only by detecting its decay products, and due to the complexity of the data reconstruction, the effective detection rate of the Higgs boson signatures

is even lower. Similar problems exist for all other studied and wanted particles, and in order to obtain sensible measurements high statistics have to be collected. The High Luminosity Large Hadron Collider (HL-LHC) project was proposed to increase the particle interaction rate by around four times, which together with continuous radiation exposure of the present experimental setups creates an additional need for an upgrade of the detection systems.

In the CMS experiment almost all subsystems will be upgraded, with the most changes being experienced by the tracking, triggering and calorimetry systems. The Silicon tracker of the CMS experiment will be completely replaced. A dedicated DAQ, Trigger and Control Board (DTC) system will be used to supervise new tracker modules during their operation in the CMS detector. Both the modules and the DTC system are currently being developed and prototyped.

In order to allow for the module prototype testing and qualification during production, an intermediate data acquisition and control system was developed in the scope of this thesis. The functionality of the new system, also referred to as  $\mu$ DTC, and newly developed module prototypes was verified in a sequence of beam test measurement campaigns performed at CERN, DESY and FNAL.

The thesis begins with a brief introduction to particle physics and performed experiments, with a focus on the CMS experiment. These topics are covered in Chapter 1. In Chapter 2, the high luminosity upgrade of the LHC accelerator is motivated and described. The corresponding upgrade of the CMS detector and in particular of its tracking system is described thereafter. The  $\mu$ DTC project is described in Chapter 3. Chapter 4 gives an overview on the test beam experiments performed at DESY. Finally, qualification results obtained from the collected data are presented in Chapter 5.

# 1. Particle Physics at the LHC

The era of particle physics began in the 19th century. Back then, a significant amount of research was focused on cathode rays [5], which have shown interaction with magnetic and electric fields. Sir Joseph John Thomson concluded in 1897 that cathode rays consist of electrons - negatively charged "subatomic" particles with non-zero mass. The electron was the first elementary particle postulated and it was discovered in the first particle physics experiment ever conducted [6]. Later, Ernest Rutherford proved that atoms consist of electrons surrounding a nucleus by performing scattering experiments [7]. Particle physics experiments have rapidly evolved starting from that point. Cathode ray tubes were replaced by particle accelerators allowing for studies of the inner structure of particles.

This chapter will introduce the concepts of modern experimental particle physics. It will describe the basics of the current understanding of nature in Section 1.1 and introduce basic experimental approaches in Section 1.2. Later on, the Large Hadron Collider (LHC) will be introduced in Section 1.3, and one of its largest experiments, the Compact Muon Solenoid (CMS), will be described in Section 1.4. The chapter will be concluded by the overview on Silicon tracking detectors in Section 1.5, which will also include the introduction of the CMS Silicon tracker.

## 1.1. The Standard Model of Particle Physics

The theoretical understanding of particle physics started to rapidly evolve in 1913 when Niels Bohr first introduced a quantisation of the trajectories of electrons surrounding the atomic nucleus [8] allowing to explain the radiation spectrum of an atom. Soon after, quantum mechanics was developed replacing the deterministic description of physical systems by a probabilistic approach. In the early 1960s Murray Gell-Mann and George Zweig independently proposed the quark model [9, 10]. According to this model, neutrons and protons along with many other earlier discovered particles consist of quarks. The model evolved into the Standard Model (SM) of particle physics [11, 12, 13, 14], a theoretical model which explains the nature of matter and the interactions among particles. In the SM each elementary particle has a set of quantum numbers, which are discrete and conserved in particle interactions. The SM divides particles into two categories based on their intrinsic angular momentum - a quantum number also known as spin. Matter is composed of fermions, half spin particles which interact by exchanging bosons, the force mediating particles which have

an integer spin. A list of the SM particles is shown in Figure 1.1. The fermions in the SM are split into three mass generations of leptons and quarks. Leptons are observable in a free state, whereas quarks exist only in bound states. Each fermion has its corresponding anti-particle. The SM describes three interactions: electromagnetism, the weak force and the strong force. The electromagnetic force is mediated by photons, the weak force is mediated by W and Z bosons, and the gluon is the carrier of the strong force. The probability of a fermion to emit or absorb a boson defines the strength of the corresponding interaction. Quantum numbers of a fermion define if it takes part in a given interaction type or not. Quarks experience all three forces, whereas charged leptons (electron, muon and tau) experience only weak and electromagnetic interactions. Neutrinos are only able to interact weakly.

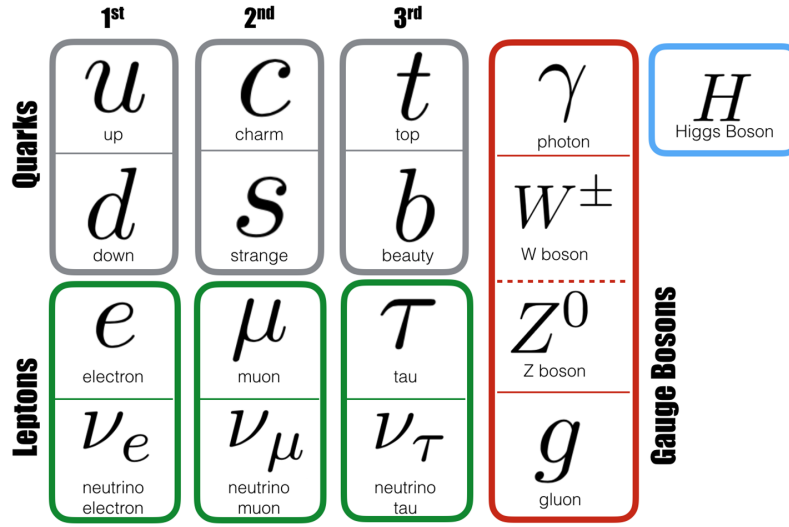


Figure 1.1.: Elementary particles in the Standard Model [15].

The theoretical background of the SM is given by the Quantum Field Theory (QFT) [16], which branches to the Quantum Electrodynamics (QED) and Quantum Chromodynamics (QCD). These theories are referred to as gauge theories due to the fact that they require the Lagrangian of a system to be invariant under symmetry transformation groups.

With such a definition, the SM allows to explain properties of elementary and non-elementary particles. However, this definition does not explain the origin of mass of the elementary particles in general. The weak force has shown a very short interaction radius, which indicated a large mass of the corresponding field mediating bosons. This was confirmed by their observation at the SPS in 1983 [17, 18], having a mass of 80.4 GeV for  $W^{\pm}$  and 91.2 GeV for  $Z^0$  [19]. In order to solve the mass generation problem, the Higgs mechanism was proposed in 1964 [20]. The mechanism introduces a new field with a non-zero vacuum expectation value and an asymmetric potential. The interaction of a system with this field leads to the spontaneous symmetry breaking and generates mass of the weak field mediators. The Higgs field mediating particle, or the Higgs boson, was discovered independently by the CMS [3] and ATLAS [21] experiments in 2012 [22, 23].

The Standard Model (SM) is a very successful theory and covers a wide range of energies from a few eV to the TeV scale. Since its definition in the 20th century, the SM has proven not only the ability to describe existing data, but also the capability to predict new discoveries. Apart from the already mentioned gauge bosons and the Higgs boson, all quarks and remaining leptons were discovered in the second half of the 20th century. The tau-neutrino was discovered in 2000 by the DONUT collaboration [24].

Despite what mentioned above, there is a set of phenomena not covered by the Standard Model. The nature of the gravitational force, the non-zero masses of neutrinos or the mass and energy distribution in the universe are some of the open questions. Moreover, there is no clear understanding of the nature of the fermion mass parametrisation. There are different extension models to the SM, along with fully-independent models, which attempt to answer the remaining questions. In order to prove theoretical predictions, particles and their interactions are studied in dedicated experimental projects.

## 1.2. Experimental Particle Physics

Particle physics studies can be split into two major branches. The first branch is astroparticle physics, which studies the cosmic radiation background and is represented by particles originating from nuclear reactions in stars and star collapse processes. The cosmic radiation background primarily consists of protons and atomic nuclei, with a lower fraction of high energetic gamma rays and neutrinos. Such particles may have energies as high as  $10^{20}$  eV, but have a very low probability to be detected, therefore not allowing to collect enough statistics for precision measurements at high energy scales. Nevertheless, different detecting techniques are used to study the secondary cosmic radiation and weakly interacting cosmic neutrinos.

The second branch of experimental particle physics is accelerator-based. Particle accelerators are comprised of electromagnetic systems, which provide the possibility to accelerate charged particles, confine them in well-defined beams and generate new particles by shooting the accelerated ones into a target or by colliding particle beams with each other. The places where particle interactions happen are typically surrounded with complex detector systems, which allow to reconstruct the occurred physics processes and study the properties of the generated particles. Accelerators provide a precisely controlled energy, timing and spacial distribution of particles, allowing to tune an experiment based on its goals. Significantly higher statistics can be obtained compared to cosmic radiation measurements. The following section will describe the Large Hadron Collider (LHC) being operated for the last decade in Geneva, Switzerland.

### 1.3. The Large Hadron Collider

The Large Hadron Collider (LHC) [2] is at the moment the largest particle accelerator ever built. The accelerator is located in a tunnel 100 m below the ground, which has a circumference of 27 km and was initially excavated for the Large Electron-Positron Collider (LEP) [25], replaced by the LHC in 2008. The LHC is operated by the European Organisation for Nuclear Research (CERN).

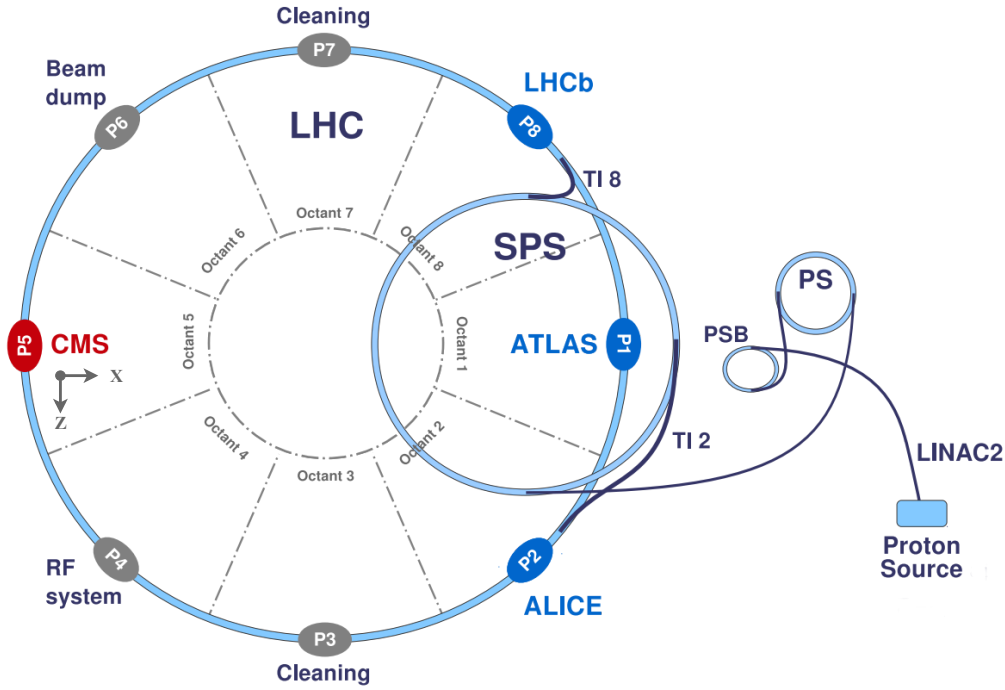


Figure 1.2.: Schematic view of the LHC beam generation in the pre-accelerator complex. From [26].

The LHC is capable of accelerating proton or heavy ion beams. In order to reach the design energy, protons are transported through a sequence of pre-accelerators as shown in Figure 1.2. Particle beams pass through the Linear Accelerator 2 (LINAC2), Proton Synchrotron Booster (PSB), Proton Synchrotron (PS) and Super Proton Synchrotron (SPS) accelerators. The resulting beams of 450 GeV energy are injected into the LHC, which is designed to deliver proton beams with an energy of up to 7 TeV. The beams contain up to 2808 bunches of approximately  $10^{11}$  protons per bunch that circulate in the accelerator [27]. The peak beam crossing rate at the LHC is 40 MHz.

Any particle collider can be characterised by the centre-of-mass energy  $\sqrt{s}$  and rate of delivered interactions. The centre-of-mass energy is defined as the total energy of the colliding particles. The LHC has started from  $\sqrt{s} = 7$  TeV in 2010 and has currently reached  $\sqrt{s} = 13$  TeV. The particle interaction rate, or luminosity, of a particle collider can be

calculated as follows

$$\mathcal{L} = \frac{N_b \cdot N_p^2 \cdot f}{A}, \quad (1.1)$$

where  $N_b$  is the number of bunches present in the accelerator,  $N_p$  is the number of particles in each bunch,  $f$  is the revolution frequency and  $A$  is the cross-sectional area of the particle beams. The latter depends on the size of the particle beams, their crossing angle and beam-beam interaction effects. The instantaneous luminosity of the LHC has been increasing since the beginning of the accelerator operation, and in the end of 2018 the LHC was delivering an instantaneous luminosity of approximately  $\mathcal{L} = 2 \times 10^{34} \text{ cm}^{-2} \text{ s}^{-1}$ .

High energy processes are initiated by partons, which only carry a fraction of the proton momentum, thus the amount of energy available for mass generation is roughly 3 - 10 times lower than the collision energy. Each process is characterised by the cross-section, which defines its occurrence probability. As an example, the calculated cross-sections for Higgs boson pair production for different centre-of-mass energies of the colliding protons are shown in Table 1.1. The rate of particle generation in a given process can be calculated using the following equation

$$\frac{dN}{dt} = \sigma \cdot \mathcal{L}, \quad (1.2)$$

where  $\sigma$  is the cross-section of the process,  $\mathcal{L}$  is the luminosity. Considering the above mentioned, in the end of 2018 one pair of Higgs bosons was generated every 30 minutes in proton-proton collisions at the LHC.

| $\sqrt{s}$    | 13 TeV                      | 14 TeV                      | 27 TeV                      | 100 TeV                   |
|---------------|-----------------------------|-----------------------------|-----------------------------|---------------------------|
| $\sigma$ [fb] | $27.78^{+13.8\%}_{-12.8\%}$ | $32.88^{+13.5\%}_{-12.5\%}$ | $127.7^{+11.5\%}_{-10.4\%}$ | $1147^{+10.7\%}_{-9.9\%}$ |

Table 1.1.: Calculated cross-sections for Higgs boson pair production for different centre-of-mass energies of the colliding protons with scale uncertainties reported as superscript and subscript. From [28].

It is evident that the LHC is a powerful tool for particle physics studies at high energies. The accelerator delivers high energetic and luminous beam collisions to its experiments and allows to collect a tremendous amount of physics data. Among the largest LHC experiments are ALICE [29], ATLAS [21], CMS [3] and LHCb [30]. The ALICE experiment is focused on the studies of heavy ion collisions. The detector is optimised to achieve maximum efficiency for events with a larger amount of the collision products than the one in proton-proton collisions, which are in the focus of the other three experiments. The LHCb experiment is focused on heavy flavour physics, which studies the quarks of the 2nd and 3rd mass generations. One of the core goals of the LHCb experiment is the study of the decays involving B mesons. The detector itself is optimised to detect the collision products which have low transverse momentum and thus decay in the forward region of the detector. Such a scenario is dominant for  $b$  and  $\bar{b}$  hadron production at high energies [30]. ATLAS and CMS are the

general purpose detectors and target precise measurements of the collision products with a high transverse momentum. The experiments allow performing high-precision measurements of the Standard Model parameters and exploring physics beyond it.

## 1.4. The CMS Experiment at the LHC

The Compact Muon Solenoid (CMS) [3] is the heaviest and one of the largest experiments at the LHC. The detector itself is located in the North part of the LHC close to the commune Cessy in France. It is built in the form of cylinder, with a length of 21.5 m, a diameter of 15 m and a total weight of 14 000 t.

The coordinate system of the detector is chosen as follows: the z-axis follows the anti-clockwise direction along the LHC ring (Figure 1.2), the x-axis points towards the centre of the LHC ring and the y-axis points vertically upwards. The detector is symmetrical around the z-axis, which allows to define an additional coordinate system. The azimuthal angle  $\phi$  is measured from the x-axis in the x-y plane and the radial coordinate in this plane is denoted by  $r$ . The polar angle  $\theta$  is measured from the z-axis. The pseudorapidity ( $\eta = -\ln \tan \frac{\theta}{2}$ ) is used to define the momentum coverage of detector systems due to the fact that for highly relativistic particles this parameter is approximately equal to the rapidity, which characterises the transverse energy of a particle. The difference of rapidities is invariant under Lorentz boost transformations, which makes it convenient to be used for kinematic calculations.

One of the key elements of the CMS detector is its superconducting solenoid. This magnet creates a uniform field of 3.8 T inside the coil, which has a bore radius of 3.15 m, a magnetic length of 12.5 m and accommodates several detector subsystems. The magnetic flux is returned through a 10 000 t Iron yoke. The large bending power of the magnet allows to precisely measure the momentum of high energy charged particles.

Particles traverse the detector outwards starting from a parton collision point located in the centre of the detector, with this point also referred to as vertex. The detector consists of several subsystems, each optimised to extract a specific type of information about a traversing particle. Most of the detector subsystems consist of barrel and end-cap parts in order to optimally cover the maximum pseudorapidity range. A schematic view of a CMS detector barrel segment is shown in Figure 1.3. The picture illustrates different subsystems installed in the experiment and several types of particles traversing the detector. The end-caps of the detector are built in the form of disks having the same order of layers as the barrel.

The Silicon tracker [32, 33, 34] is used to reconstruct the vertex positions and momenta of charged particles. As the Silicon tracker is in the focus of this thesis it will be discussed in more detail in Section 1.5.2.



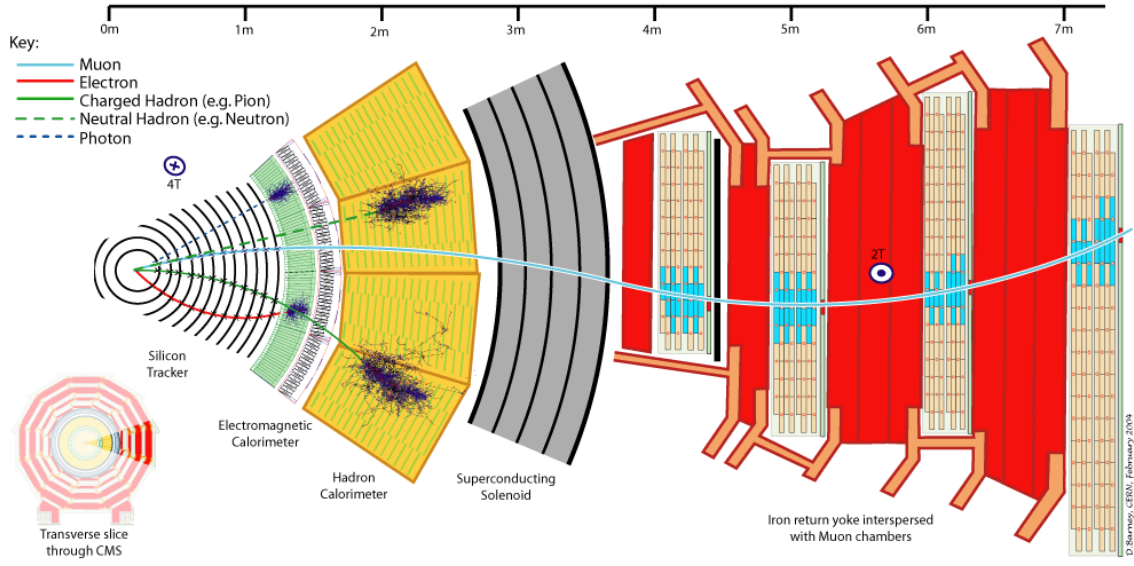


Figure 1.3.: Schematic diagram of the particles traversing the CMS detector [31]. The beam direction is perpendicular to the picture plane.

After passing the volume of the Silicon tracker, particles enter the CMS Calorimeters, where their energies are being measured. The calorimetry system is divided in segments in order to distinguish particles entering it and to match a particle with a track constructed by the tracking detector. A particle passing through the calorimeter leaves a fraction of energy in each segment. A total amount of the deposited energy corresponds to the energy loss, or to the particle energy in case of the full absorption. The calorimeter of the CMS detector consists of the electromagnetic and the hadron calorimeters. Particles which mostly interact via the electromagnetic force, such as photons or electrons, are fully absorbed and measured in the Electromagnetic Calorimeter (ECAL) [35], see Figure 1.3. The particles that were not absorbed reach the Hadron Calorimeter (HCAL) [36], which is dedicated to measure the energy of the hadronic jets.

Both the barrel and end-cap segments of the ECAL consist of lead tungstate ( $\text{PbWO}_4$ ) scintillating crystals, complemented with a pre-shower detector placed in front of the end-cap. The HCAL is a sandwich-type calorimeter built out of alternating high density brass and plastic scintillator layers. The barrel part of the HCAL is complemented by a tail catcher, which is placed behind the superconducting solenoid and used to detect hadron showers not absorbed in the main volume of the calorimeter.

As can be seen in Figure 1.3 most of the particles traversing the CMS detector are being absorbed in the calorimeters. However, high energetic muons have a minimal energy loss in the detector, which makes them traversing the inner detector systems and leaving information in each subsystem without being stopped. In order to identify these particles, the outermost layer of the CMS detector is occupied by the Muon systems [37], which are integrated in the return yoke of the solenoid magnet. The high radial distance of the muon systems decreases

the required granularity of the channels. Gaseous detector chambers of different types are used as the technology for the muon systems.

Neutrinos and some other undiscovered yet weakly interacting particles, which may be dark matter candidates, are not detected in CMS and have to be reconstructed by estimating missing transverse energy during the data analysis.

Data from different subsystems are forwarded to corresponding data acquisition units, and are later combined in the central DAQ system. Given the amount of CMS subsystems and the millions of detector channels, it would be impossible to transfer and store data from each bunch crossing for later analysis. Data selection criteria have to therefore be defined and implemented. The trigger system allows to use the available data transfer bandwidth in an efficient way and to select collisions based on specific signatures, such as the presence of high transverse momentum particles, certain leptons or hadronic jets.

The trigger system of the CMS detector is comprised of the Level-1 Trigger (L1) and the High Level Trigger (HLT) [38]. The decision taking of the L1 trigger is limited in time to  $3.2\,\mu\text{s}$  and is based on the collision characteristics obtained from the Muon systems and the Calorimeters. The L1 trigger is fully realised in hardware using Field Programmable Gate Array (FPGA) and Application Specific Integrated Circuit (ASIC) devices, which execute simplified collision reconstruction algorithms. The L1 trigger applies basic selection criteria, such as high transverse momentum selection or presence of certain particles in the physics event, and allows to reduce the triggered event rate to around  $100\,\text{kHz}$ . Being the first stage of the data selection, the L1 trigger has to provide an optimal selection of data, thus defining the efficiency of the whole CMS detector. An increase of the particle multiplicity in a collision would cause a significant degradation of efficiency of the L1 system.

The subsequent triggering stage is the HLT, which consists of several thousands of CPUs performing event reconstruction from all the CMS subsystems in order to search for interesting event signatures. The HLT procedures are limited in time to  $50\,\text{ms}$  and are based on time-optimised reconstruction algorithms, which process only part of the detector volume indicated by the L1 trigger. At this stage, the event rate is reduced to approximately  $800\,\text{Hz}$  [39] and selected data are finally stored for offline analysis.

### 1.5. Silicon Tracking Detectors

Silicon detectors are widely used in high energy physics experiments. Silicon offers a good compromise in terms of signal-to-noise ratio, radiation hardness and production cost. The latter is caused by the extensive usage of Silicon devices in consumer electronics and, as a result, a tremendous production experience. Silicon detectors are also used in various subsystems of the CMS detector. The tracker is fully built of Silicon detector modules, whereas avalanche photo-diodes are partially used as the sensitive layers in the CMS calorimeters [35].

This section will introduce the basic concepts of Silicon tracking detectors and describe the CMS Silicon tracker thereafter.

### 1.5.1. Basic Concepts

A typical semiconductor detector consists of a sensitive layer, or sensor, and read-out electronics, which perform processing of the analog signals. The following text will focus on the physics principles behind the semiconductor sensors and give an example of a typical read-out electronics chain used for the data sampling.

**Semiconductor Sensors** According to the Pauli exclusion principle [40], two identical fermions cannot reside in a state with the same quantum numbers. The occupancy of energy states in fermion systems is expressed by the Fermi-Dirac distribution

$$f(E) = \frac{1}{e^{(E-E_F)/k_B T} + 1}, \quad (1.3)$$

where  $k_B$  denotes the Boltzmann constant,  $T$  denotes the temperature of the system and  $E_F$  is the Fermi level. The distribution itself yields the probability density of finding a fermion with a given energy, while the Fermi level defines the energy at which the probability of finding a fermion is  $1/2$ .

At  $T = 0$  K all energy states up to  $E_F$  are occupied, whereas for higher temperatures electrons start to occupy excited energy states. In atoms electrons have different orbits with certain binding energies, while in atomic systems energy states of electron shells combine and form energy bands. The band structure of different materials is schematically shown in Figure 1.4. The valence band is the last energy band completely filled with electrons at  $T = 0$  K, whereas the upper energy band, which is only partially filled with electrons, is called the conduction band. The region between the conduction and valence bands does not have any allowed energy states and is called the band gap. The conduction band contains electrons contributing to the electrical conductivity of a material. According to the diagram, there are three basic types of materials: conductors, semiconductors and insulators. Even at a temperature of  $T = 0$  K conductors have electrons in the conduction band, while semiconductors and insulators do not have any free electrons and thus act identically. At higher temperatures, the energy of thermally excited electrons is sufficient to pass the band gap in semiconductors and these materials become conductive. Thermally excited electrons are called intrinsic charge carriers, thus a pure semiconductor material is referred to as intrinsic semiconductor.

The band theory can be explained by the chemical bonds between the atoms. Bonds are formed due to the interaction of the electron shells of the atoms with each other. The electrons in the outermost shell of an atom define the electrical conductivity of the corresponding element. If the outermost (valence) shell is completely filled with electrons, the element does

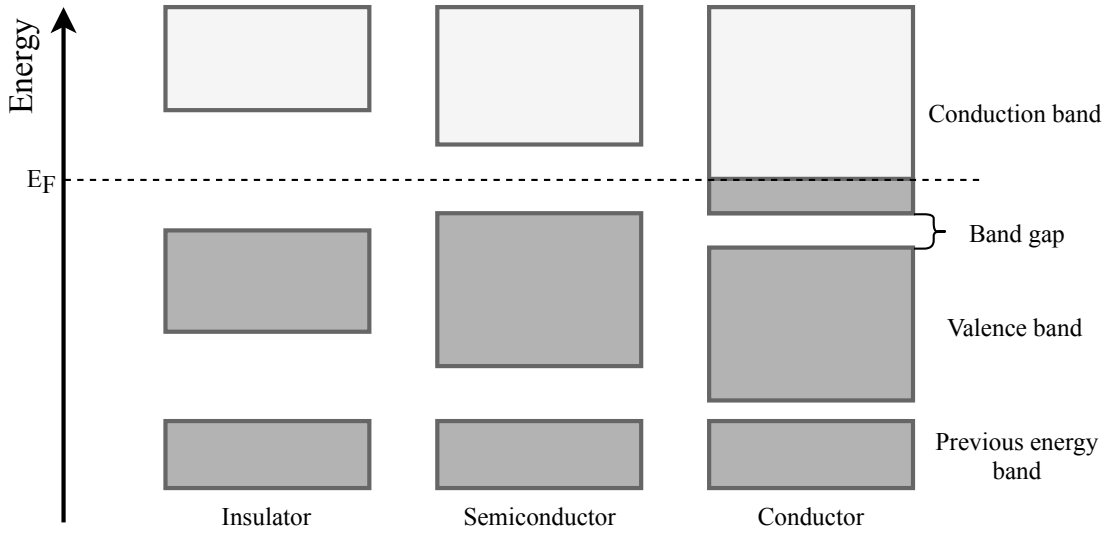


Figure 1.4.: Schematic diagram of the energy band structure for insulators, semiconductors and conductors at  $T = 0$  K. The dark filled areas represent the energy states containing electrons.

not participate actively in chemical reactions, remains gaseous at room temperature and does not conduct electricity well. In elements which have the valence shell almost filled with electrons (F, Cl and Br), it is energetically beneficial to complete the shell when forming chemical bonds, and these elements become non-electrically conductive solids, or insulators. Elements having a single electron in the valence shell (Li, Na and Cu) are conductors due to the fact that the electrons from the outermost shell easily travel between the atoms. Atoms such as C, Si and Ge have four electrons in the valence shell and form elements by sharing electrons with neighbouring atoms without forming ions. This bonding type is referred to as covalent bonding, with the corresponding elements being called semiconductors. These elements have weaker binding of electrons compared to insulators and conduct electricity under certain conditions.

Conductivity is caused by charge carriers, electrons or holes, moving through a crystal lattice. When an electron leaves its initial place a vacancy appears in the lattice. This vacancy is called a hole and soon gets filled by another electron, which in turn leaves a vacancy in another place. In this way holes travel through the lattice resulting in hole conductivity. The mobility and thus the velocity of electrons and holes can be different depending on the material and external electric field applied. In an intrinsic semiconductor, the amount of electrons and holes is equal, which means that there is no dominant charge carrier type. The concentration of the charge carriers in the intrinsic Silicon is  $9.65 \times 10^9 \text{ cm}^{-3}$  at 300 K [41].

In order to modify the conduction properties of semiconductors, impurities can be introduced into the lattice through a doping process, with the resulting lattice diagram being schematically illustrated for Silicon in Figure 1.5. In order to increase the electron conductivity, the atoms with an additional valence electron are introduced into the lattice. Such

doping atoms are called donors, and after doping the resulting semiconductors are referred to as n-doped, or n-type, semiconductors. In the lattice diagram for the n-doped Silicon, a Phosphorus atom which contains five valence electrons is used as a donor. P-doped semiconductors are produced by doping intrinsic semiconductors with acceptor atoms, which contain one less electron in the outer shell. In p-doped semiconductors hole conductivity is dominant. In the corresponding diagram for the p-doped Silicon, a Boron atom is used as an acceptor. Both n-doped and p-doped semiconductors are known as extrinsic semiconductors because of their modified properties. The doping concentration (and thus the charge carrier concentration) is typically increased to  $10^{12} \text{ cm}^{-3}$  -  $10^{18} \text{ cm}^{-3}$ , while further increase leads to the narrowing of the band gap, with the resulting material being called degenerate semiconductor.

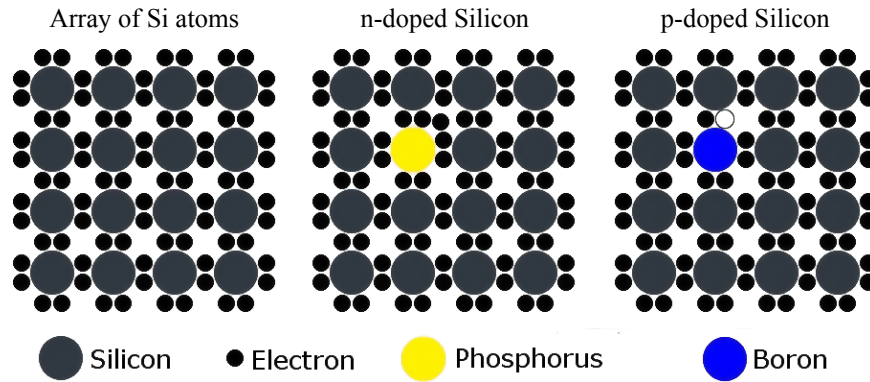


Figure 1.5.: Schematic lattice diagram for intrinsic and extrinsic Silicon.

Semiconductor sensors exploit a pn-junction, which is a combination of p- and n-doped semiconductors. The schematic diagram of the energy states for doped semiconductors and a pn-junction is shown in Figure 1.6. By doping, the Fermi energy level shifts due to an increased amount of electrons or holes in the corresponding extrinsic semiconductor. When creating a junction between the p- and n-doped semiconductors, electrons and holes start to recombine at the boundary, leaving a region with positive space charge on the n-doped side and a negative space charge region on the p-doped side. The resulting electric field opposes charge diffusion, and a zone without free charge carriers is formed, which is also called depletion zone or space charge region. The depletion zone can be enlarged by adding electrodes at either sides of the junction to form the electric contact and applying an external voltage to the pn-junction. A positive voltage applied to the n-side of the junction creates an electric field attracting charge carriers, and at a certain voltage the electric field covers the full thickness of the sensor and the latter becomes fully depleted. The corresponding voltage is typically of the order of  $\mathcal{O}(100 \text{ V})$ , depends on the doping concentration and thickness of the sensor, and is referred to as depletion voltage.

When a charged particle passes through a depleted Silicon sensor, it creates around 70 electron-hole pairs per micrometre of sensor thickness, with an energy of 3.6 eV required to create a single pair [19]. Electrons and holes start to drift in the applied electric field to the corresponding electrodes and, according to the Shockley-Ramo theorem [42], induce

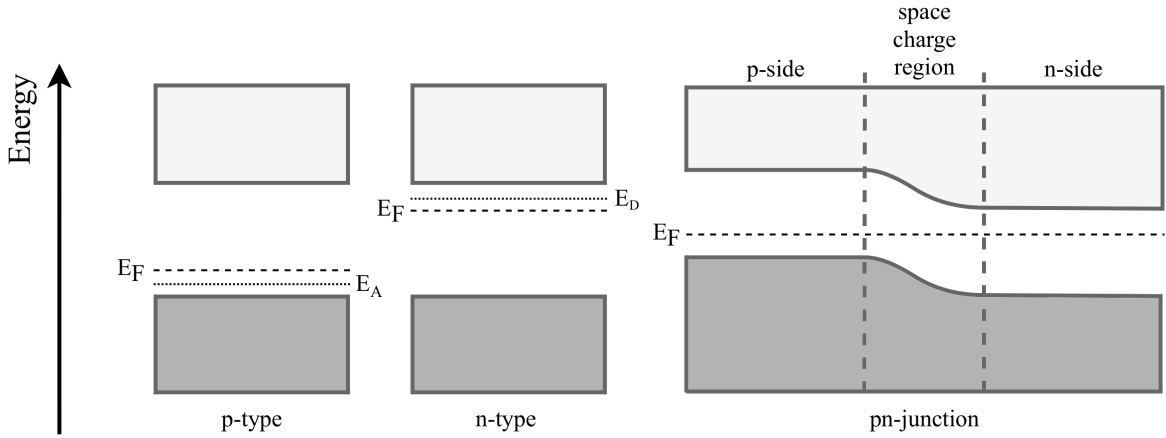


Figure 1.6.: Energy diagram of doped semiconductors and a pn-junction.  $E_A$  and  $E_D$  are the energy levels of acceptor and donor atoms respectively.

an electrical current on the electrodes. The amplitude of the current is proportional to the amount of particles drifting in the electric field, with the time from the beginning of the charge drift until the moment when all the charges were collected being referred to as charge collection time. The latter is used to characterise the sensor, depends on the sensor type and is different for electrons and holes, typically being of the order of  $\mathcal{O}(10\text{ ns})$  for both.

In Figure 1.7, a simplified structure of typical semiconductor sensors is shown. Here,  $p^+$  and  $n^+$  denote implants with a doping concentration larger than in the p-bulk, which allows to improve the electrical junction between the Aluminium electrodes and the semiconductor material. The pn-junction is formed in the interface region between the p-bulk and the  $n^+$  implant. The top electrode is segmented in one dimension to make a strip sensor or in two dimensions to make a pixel sensor, this allows to increase the channel granularity of a semiconductor sensor thus improving its positional resolution. Each channel of a sensor is connected to a read-out ASIC using dedicated conductive bonds in form of wires for strip sensors or tiny balls (bump-bonds) for pixel sensors. Read-out electronics can be integrated in the sensor itself, as in Complementary Metal-Oxide-Semiconductor (CMOS) sensors [43].

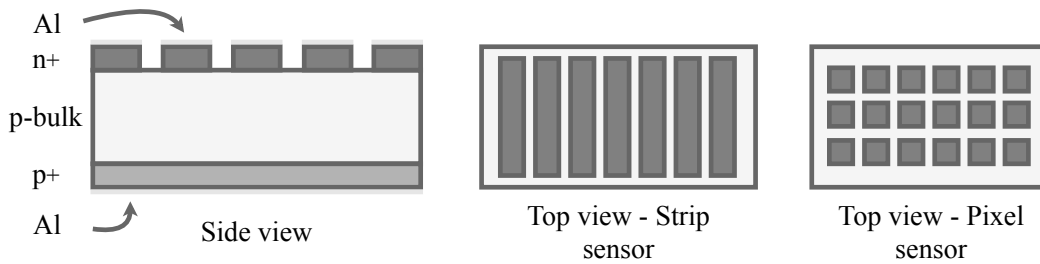


Figure 1.7.: Simplified structure of a semiconductor sensor.

**Read-Out Electronics** The combination of a semiconductor sensor, read-out electronics and mechanical supports forms a semiconductor detector, or front-end module. A schematic diagram of the typical signal processing chain in the front-end module is shown in Figure 1.8. Each sensor channel is connected to an amplifier and a discriminator, allowing to integrate the channel current and compare the resulting charge to a reference voltage also called threshold voltage. If the charge in a given channel is sufficient to pass the discrimination stage, the corresponding information bit is formed, also referred to as hit. At the digital sampling stage the hit information from all channels is combined. In some read-out chains, an analog-to-digital converting stage can be added after the discriminator in order to provide charge information and allow to further improve positional resolution by combining an input from several channels. Such a configuration is used in the existing CMS tracker, but for the upcoming upgrades it will be replaced with a binary system, as shown in Figure 1.8, in order to decrease data throughput needs.

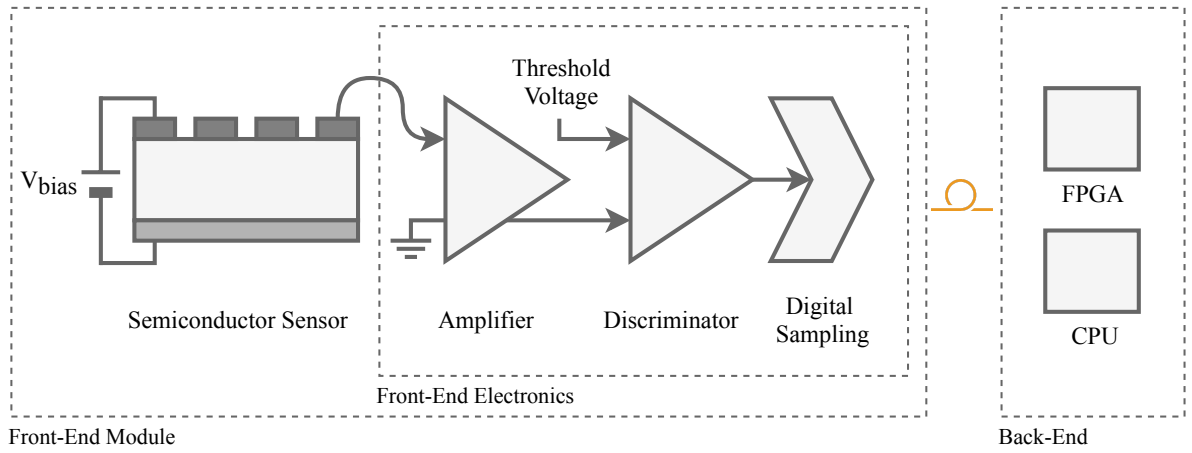


Figure 1.8.: Schematic diagram of the typical read-out chain of a tracking detector module.

Data from the front-end modules are transferred to a Data Acquisition (DAQ) system using electrical cables or optical fibres. The DAQ system is typically located outside of the detector sensitive volume, thus called a back-end system, and is responsible for the data aggregation and further forwarding to the storage.

The hit data can be streamed to a DAQ system continuously or upon receiving a trigger signal, resulting in only selected events being read out. At the LHC the sampling rate for most of the detector subsystems is 40 MHz, the total channel granularity for just the CMS Silicon tracker is of the order of  $\mathcal{O}(10^8)$  channels. The continuous read-out of data from every single bunch crossing would result in a tremendous data rate, which is impossible to handle. In order to solve this problem, potentially attractive events are selected based on the decision of the Level-1 Trigger system mentioned earlier. Data are buffered in the front-end modules until the trigger decision is made, with the depth of the front-end buffers defining a maximum amount of time available for the trigger decision, or trigger latency. A compromise has to be found in terms of the buffer size, as increasing it leads to an increase of the power consumption of every single front-end module.

**Radiation Effects** The performance of Silicon tracking detectors tends to degrade in the harsh radioactive environment present in the LHC experiments. Most of the energy loss of a particle traversing matter is due to collisions with atomic electrons, which is also referred to as Ionising Energy Loss (IEL) and serves as a base principle of particle detection. In the Non-Ionising Energy Loss (NIEL) process, nuclear interactions result in collisions where atoms are displaced from the lattice and the energy is dissipated in lattice vibrations. Both ionising and non-ionising processes cause radiation damage of a detector, which can be categorised as surface and bulk damages.

Bulk damage is mostly caused by the non-ionising radiation. A displacement of a single atom does not lead to significant changes in the material, but if the atom receives sufficient recoil energy to displace nearby atoms, defect clusters are formed. This creates new energy levels in the semiconductor, which cause parasitic current through the detector and trapping of charge carriers in the defective zones, thus deforming the electric field. Charge trapping and electric field deformation both influence the charge collection time and efficiency, resulting in the degradation of the sensor performance.

Surface damage mostly affects thin insulating Silicon oxide layers between the sensor channels. The displacement of atoms does not cause significant effects here due to the irregularity of the crystal structure in the surface region. The main contribution to the surface damages is from the ionising radiation. The mobility of electrons is significantly higher in the Silicon oxide layer, holes can be captured in the interface region between the Silicon and oxide, which results in an increase of the positive charge. The positive surface oxide charge may create short circuits in Silicon sensors having a p-doped bulk, which were schematically shown in Figure 1.7. As a consequence, this increases the bulk current and the cross-talk between the read-out channels, which leads to additional noise in the detector channels and the degradation of the detector resolution.

In addition to the permanent damage, an ionising particle may induce significant charge in an integrated circuit. The effect is also referred to as Single Event Upset (SEU) [44] and causes the corruption of digital information. SEUs affect primarily memory cells of the front-end electronics. The effect does not cause a permanent damage, thus information is typically recovered after the reconfiguration of electronic circuits.

Permanent radiation damages cause an increase of the parasitic current, as well as a decrease of the efficiency of a detector. Up to a certain extent, a detector can be re-calibrated and operated at higher voltages and lower temperatures, but at some point signals become indistinguishable from noise. Therefore, the front-end modules which operate in high-dose regions have to be replaced periodically. A typical operation time for the inner layers of a Silicon tracker at the LHC is 5 - 10 years. In order to assure such a long operation time, the front-end modules have to be radiation hard. The radiation hardness is defined as the sustainability of a system to high radiation fluxes and doses, and can be improved by adjusting the doping concentration in a semiconductor and the thicknesses of the internal sensor layers. For digital circuits, error detection and correction techniques, such as data triplication, have to be used in order to protect data from SEUs.



### 1.5.2. The Silicon Tracker of the CMS Detector

The LHC currently delivers approximately 20-50 interactions per bunch crossing, with a corresponding amount of primary vertices. The interaction region of the detector is surrounded by the Silicon tracker, which is comprised of pixel and strip subsystems, both consisting of several layers of front-end modules detecting the positions of particles passing through the detector. By combining the information from all layers, particle trajectories are reconstructed.

The spatial coordinate resolution and the sampling rate of the system have to be sufficient to precisely reconstruct vertices from every bunch crossing. At the same time, the total material thickness of the tracking system has to be kept at a minimum, as the increase of the thickness would increase the amount of multiple scattering in the tracking layers, which in turn affects the tracking resolution. A requirement on the radiation hardness of the tracking system is imposed due to the close positioning to the interaction point. A schematic layout of the resulting system is shown in Figure 1.9. A detailed technical description of the CMS tracker is available in [3].

**Inner Tracker** The inner part of the tracker is comprised of pixel modules and is the closest subsystem to the interaction point. The highest density of particle tracks and the highest radiation flux are present in this region, therefore the granularity and the radiation hardness become essential requirements for the inner tracker. This subsystem has already experienced one upgrade since the beginning of the CMS operation [34]. The initial pixel detector [32, 33]

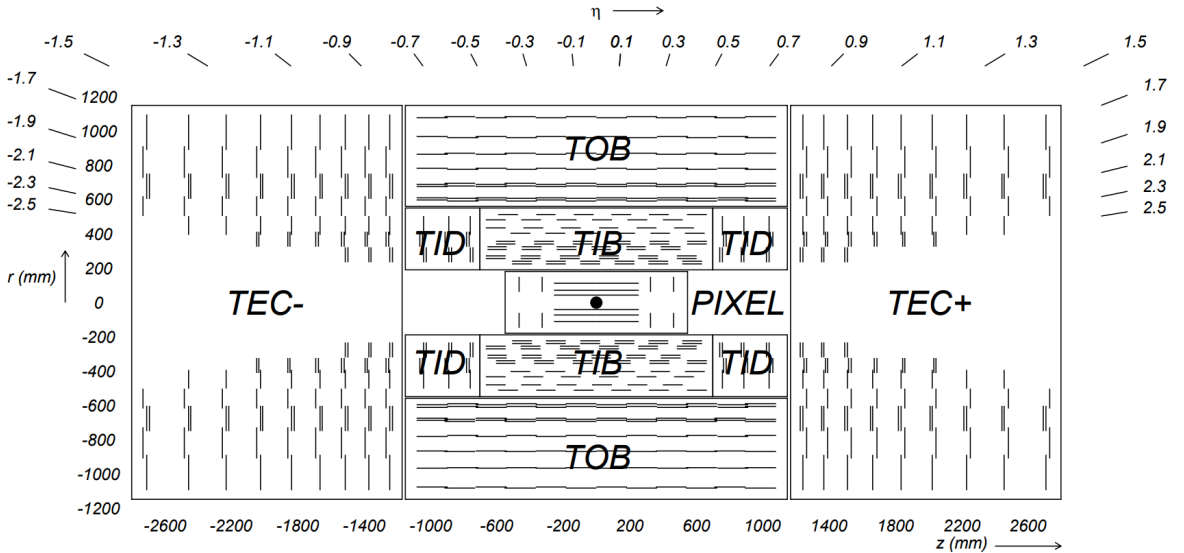


Figure 1.9.: Schematic cross-section of the CMS Silicon tracker. Each line represents a detector module. Double lines indicate back-to-back modules. The nominal interaction point is marked with a solid black dot. From [3].

was comprised of three concentric barrel layers at radii of 4.4 cm, 7.3 cm and 10.2 cm. Two end-cap disks on each side complemented the barrel segment, being located at distances of  $z = \pm 34.5$  cm and  $\pm 46.5$  cm. This configuration of the inner tracker provided a hit resolution of around  $10\text{ }\mu\text{m} - 20\text{ }\mu\text{m}$ , exploiting the pixel sensors with a pitch of  $100\text{ }\mu\text{m} \times 150\text{ }\mu\text{m}$  [34].

Over the years of operation radiation damage has been constantly accumulated in the inner layers of the detector. In addition, the delivered instantaneous luminosity of the LHC was constantly increased. As a consequence, the efficiency of the innermost layer of the initial tracker had dropped and the increase of the collision multiplicity made distinguishing particle tracks more complicated, increasing the rate of falsely reconstructed tracks, which may be formed from a combination of either unrelated or spurious hits. In order to deal with the above mentioned challenge, the inner pixel tracker was replaced in the beginning of 2017 [34]. The comparison between the two system revisions is shown in Figure 1.10.

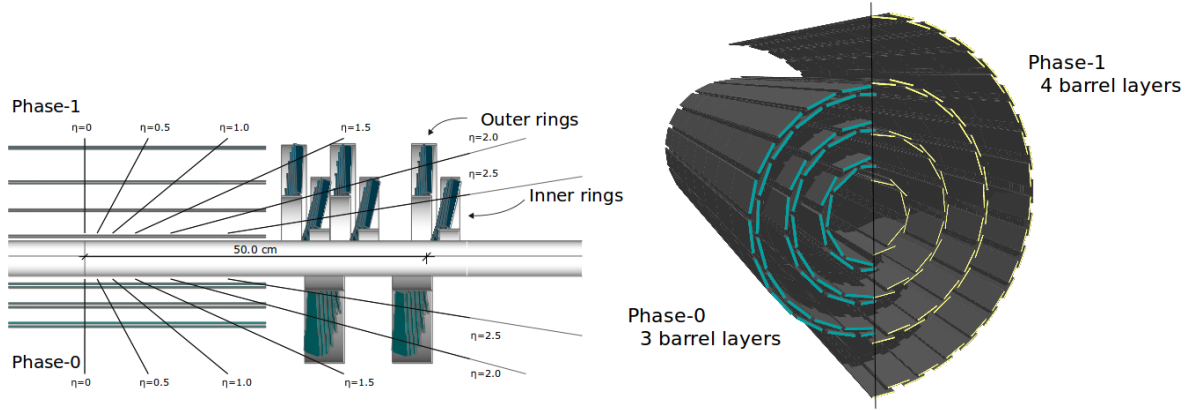


Figure 1.10.: Conceptual layout for the Phase I upgrade pixel detector in the r-z view (left) and three-dimensional view (right) compared to the present detector design. From [34].

The new inner pixel tracker consists of four concentric barrel layers located at radii of 2.9 cm, 6.8 cm, 10.9 cm and 16.0 cm. Three disks on either side of the system form the end-cap part of the inner pixel tracker and are placed at distances of  $z = \pm 29.1$  cm,  $\pm 39.6$  cm and  $\pm 51.6$  cm. The new system offers higher number of detecting layers and thus a significantly larger amount of channels. Moreover, the innermost layers are located closer to the interaction point, which allows for better vertex reconstruction. The detector is cooled using the two-phase  $\text{CO}_2$  cooling approach [45] instead of the mono phase  $\text{C}_6\text{F}_{14}$ . The  $\text{CO}_2$  cooling system operates at high pressure, which allows to reduce the size of the cooling pipes and, along with the reduced weight of the support structures, results in a significantly smaller material thickness of the new inner tracker [34].

A comparison of the measured hit efficiencies for both systems is shown in Figure 1.11. At the end of operation, the efficiency of the innermost layer of the old tracker dropped to 94 % at an instantaneous luminosity of  $1.5 \times 10^{34} \text{ cm}^{-2} \text{ s}^{-1}$ , while the corresponding layer in the upgraded detector shows a hit efficiency of more than 98 %.

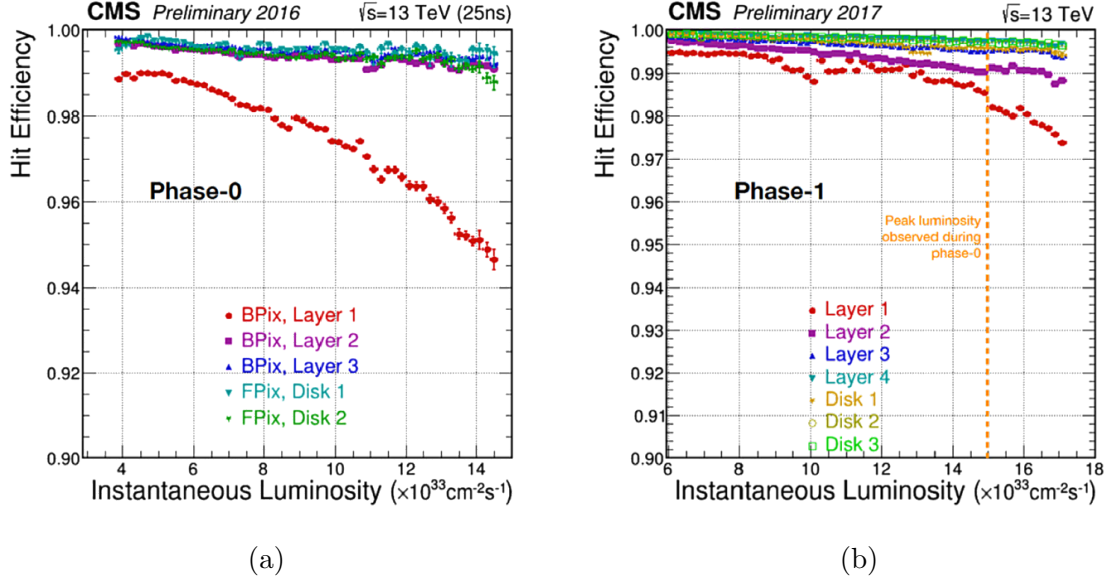


Figure 1.11.: Measured hit efficiency as a function of instantaneous luminosity for the initial inner pixel tracker at the end of operation (a) and for the current one (b). From [46].

**Outer Tracker** The CMS outer tracker consists of Silicon strip modules due to the fact that the track multiplicity per unit area is much lower for higher radii, which reduces the need for high channel granularity. Moreover, the total area of the outer tracker is larger than the inner tracker, and the usage of pixel sensors would significantly increase the amount of read-out channels. This would increase the required data transferring bandwidth, without providing a significant profit. The outer tracker modules are distributed among four different subsystems, as shown in Figure 1.9: Tracker Inner Barrel (TIB), Tracker Inner Disks (TID), Tracker Outer Barrel (TOB) and Tracker End-Cap (TEC). Each module of the system consists of either one Silicon strip sensor with a thickness of  $320 \mu\text{m}$  or two  $500 \mu\text{m}$  thick sensors.

**Tracking Efficiency and Resolution** One of the main parameters characterising the performance of the CMS tracker is the tracking efficiency. The simulation of the tracking efficiency of the current tracker for different vertex multiplicities is shown in Figure 1.12. As can be seen, the tracker has an efficiency of more than 90 % for  $p_T > 0.9 \text{ GeV}$  in the region  $|\eta| \lesssim 1$  corresponding to the barrel. The efficiency drops slightly in the transition regions between the end-cap and the barrel, and has a significant drop in the far forward region, which is caused by the lack of detector systems in these regions.

The simulated transverse momentum resolution for the CMS tracker is shown in Figure 1.13. The simulations show a comparison between the  $p_T$  resolution for the systems before and after the inner tracker upgrade, the data from the year 2016 represents the operation with the old inner tracker. The additional fourth layer in the inner tracker allowed

to improve the  $p_T$  resolution in the  $1.2 < |\eta| < 1.6$  region (see Figure 1.13a). According to Figure 1.13b, the tracker provides a resolution of approximately 1.5 % for  $p_T > 1$  GeV.

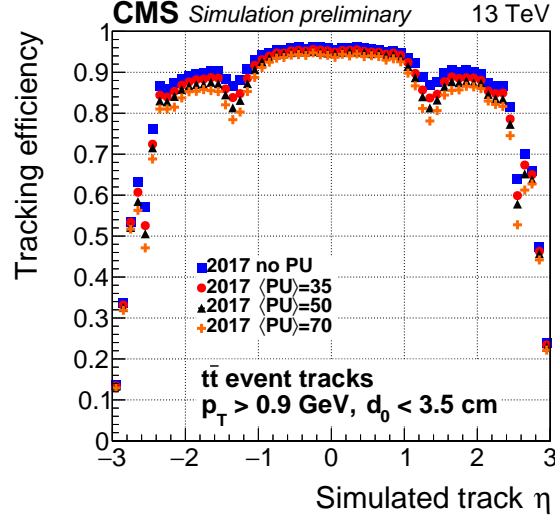


Figure 1.12.: Simulated track reconstruction efficiency for the CMS tracker at different pile-up conditions [47].

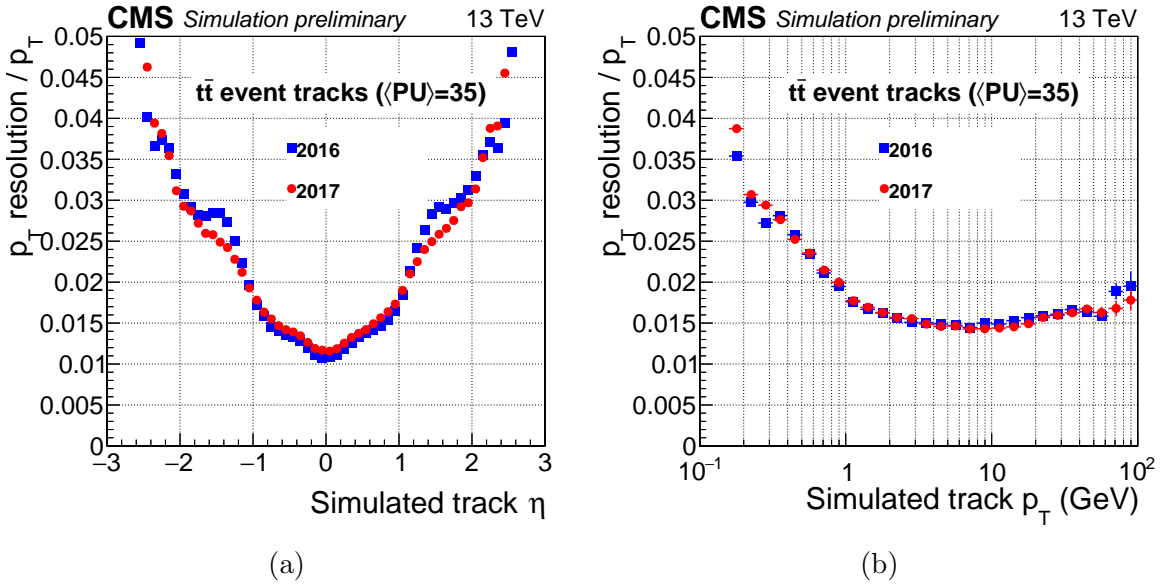


Figure 1.13.: Comparison of the simulated track  $p_T$  resolution plots for the years 2016 and 2017 [47].

All what mentioned above makes the CMS Silicon tracker a powerful tool for measuring particle trajectories and allowing to precisely disentangle different particles originating from the interaction point. However, the experimental goals constantly dictate new requirements for energy and intensity of the colliding beams. In order to overcome the evolving challenges, the CMS detector and the tracker in particular have to be constantly upgraded. The future

challenges for the CMS detector along with the proposed solutions will be discussed in the next chapter.



## 2. The High Luminosity LHC

A set of important physics results has already been acquired at the LHC. Among them are the discovery of the Higgs boson and the studies of its decay. The coupling of the Higgs boson to other particles, its spin and parity were measured [48]. Measurement of the very rare  $B_0^s \rightarrow \mu^+ \mu^-$  decay allowed to define constraints on the models of physics beyond the SM [49]. The observed branching ratio is consistent with expectations of the SM, whereas if new physics was present in the LHC energy range, it would either enhance or suppress the predicted decay rate. These and other studies have proven the importance of the LHC as an experimental tool.

Further precision measurements of the SM require more statistics due to significant contribution of the statistical uncertainties to the total measurement uncertainties. As such, the statistical uncertainty on the  $t\bar{t}H$  production cross-section in the  $H \rightarrow b\bar{b}$  channel with a di-lepton final state at CMS currently reaches a value of 39% [50]. Moreover, there is a set of measurements which are not yet performed. For instance, the Higgs-field potential involves terms proportional to  $\phi^2$  and  $\phi^4$ . An elementary field potential of this kind has never been seen before in nature, and it is crucial to prove that this potential can indeed be associated with vacuum. Even though the Standard Model covers a range of energies from eV to the TeV scale, it is possible that it cannot explain physics at higher energies thus being a low energy theory. Super Symmetry (SUSY) and other theoretical models may extend the SM to higher energy range by introducing new particles, but physics processes in these models are also associated with small cross-sections at the LHC. Due to the rare nature of the investigated processes, the LHC is close to reaching the limit of its discovery potential. All mentioned and other possible studies would take decades to collect reasonable statistics. Operating the LHC in the current mode for longer time would require continuous maintenance and human effort, which is comparable to the investment in an upgrade project, but providing much less of scientific results. This makes it essential to increase the luminosity. A High Luminosity Large Hadron Collider (HL-LHC) project was proposed, including a series of modifications to the existing accelerator complex, which will allow to increase the instantaneous luminosity by up to four times.

## 2.1. Accelerator Upgrade

The LHC beams are injected from a cascade of pre-accelerators. As already shown in Figure 1.2, the pre-accelerators are the Linear Accelerator 2 (LINAC2), Proton Synchrotron Booster (PSB), Proton Synchrotron (PS) and Super Proton Synchrotron (SPS). In order to increase the luminosity, the brightness of the beams has to be increased along with the decrease of beam losses in the transport lines. The upgrade of the whole injection chain is referred to as the LHC Injectors Upgrade (LIU) [51], and will mostly take place in 2019-2020.

As a part of the LIU, the existing 50 MeV LINAC2 will be replaced by LINAC4, which is able to accelerate Hydrogen ion beams to an energy of 160 MeV. The LINAC4 accelerator was already built and commissioned, and is currently being connected to the rest of the accelerator complex. The output energy of the PSB will be increased to 2.0 GeV with respect to the current 1.4 GeV. The PS and SPS accelerators will experience a sequence of stability upgrades, among which is the installation of new accelerating cavities, bending magnets and collimators [51]. The injection and extraction structures are being modernised in order to decrease beam losses between the accelerators.

The LHC accelerator upgrade will be split into two phases. In 2019-2020, a new cryogenic system will be installed along with new 11 T bending magnets, which due to the increased bending power allow to allocate free space for extended collimators [52]. Most of the remaining work packages of this upgrade will be covered in 2023-2025. In order to allow for the increase in luminosity, the beam sizes have to be reduced in the interaction regions, which will lead to the increase of their size in the dipole and quadrupole insertion magnets. In order to assure safe operation, the apertures of the insertion magnets will be increased. In the meantime, the decrease of the beam sizes will be achieved by using Nb<sub>3</sub>Sn insertion magnets, which are able to provide magnetic fields with a peak value of 12 T on the coils, compared to the 9 T fields in the existing Nb-Ti magnets [52].

A schematic representation of a LHC collision is shown in Figure 2.1a. In conventional accelerator operation bunches become elliptical due to relativistic effects and typically cross each other at a specific angle, which leads to a limited overlap and smaller interaction rate. In order to allow for a higher overlap, the concept of superconducting radio-frequency crab cavities will be used for the first time in a hadron collider and is illustrated in Figure 2.1b. Crab cavities will turn the bunches before the collision, thus increasing the luminosity. The cavities will be installed at both sides of the ATLAS and CMS experiments, allowing also to tilt the out-going beams after the collision and bring them on their initial orbits.

The aforementioned modifications allow to improve the performance of the existing accelerator complex. The prediction for the LHC luminosity for the upcoming years is shown in Figure 2.2. After the upgrade the instantaneous luminosity will be slowly increased from the starting point of  $\mathcal{L} = 2 \times 10^{34} \text{ cm}^{-2} \text{ s}^{-1}$  to a value of  $\mathcal{L} = 7.5 \times 10^{34} \text{ cm}^{-2} \text{ s}^{-1}$ . The LHC will deliver around  $300 \text{ fb}^{-1}$  of integrated luminosity in its first 10-12 years of operation [53], whereas for the HL-LHC the plan is to reach  $3000 \text{ fb}^{-1}$  within the first decade.



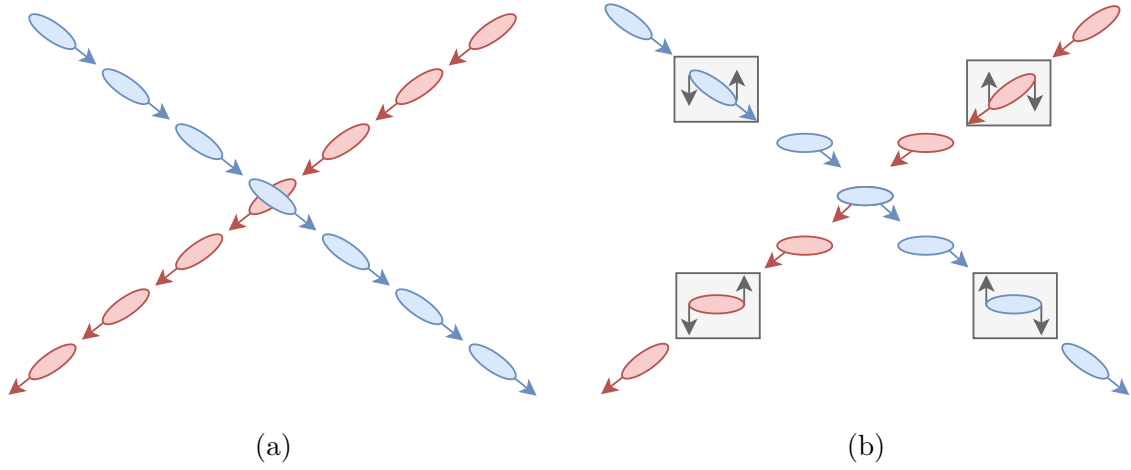


Figure 2.1.: Effect of crab cavities on charged particle beams. Current LHC collision (a) and collision with Crab cavities (b).

The LHC experiments will also be affected by the higher luminosity. The existing subsystems continuously degrade due to the harsh radiation environment and some of them will have to be completely replaced by the beginning of the HL-LHC era. The amount of primary vertices will increase to approximately 200 per bunch crossing, thus significantly increasing the track density and data throughput from the detectors. Such conditions require an upgrade of the front-end electronics and data acquisition systems in the experiments. The upgrade of the CMS experiment is in the focus of this thesis and will be discussed in the following.

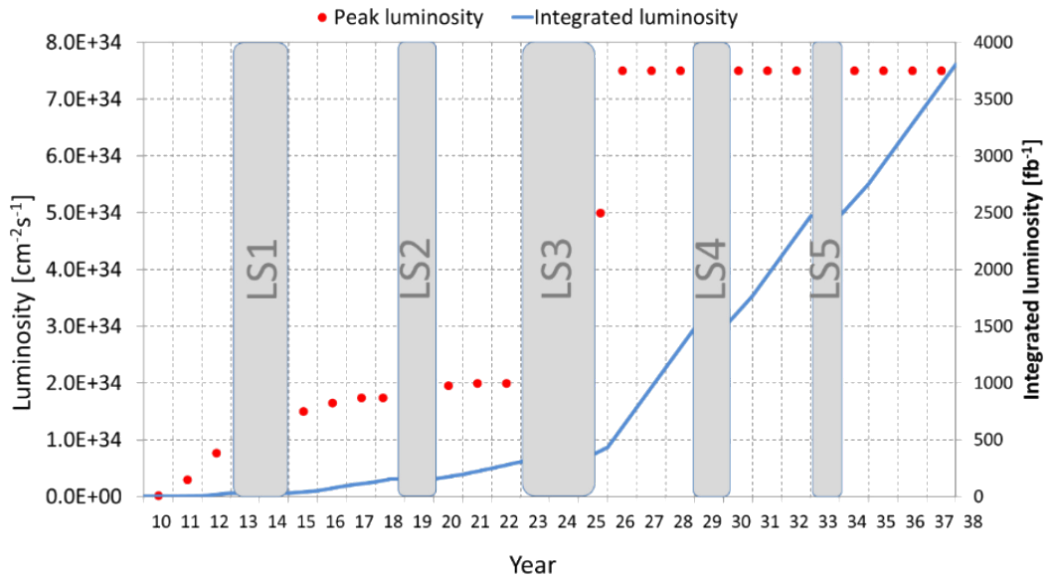


Figure 2.2.: Forecast for the peak luminosity (red dots) and integrated luminosity (blue line) for the coming years [54].

## 2.2. CMS Phase-2 Upgrade

As already mentioned, a pile-up of up to 200 vertices per bunch crossing is expected for the high luminosity operation phase of the CMS experiment. High luminosity data taking campaigns in 2011 and 2012 [53] were aiming to estimate the performance of the CMS subdetectors under conditions similar to the HL-LHC. Data with a pile-up of up to 100 vertices were collected and analysed. The investigation suggested a full replacement of the end-cap calorimeters and the tracker in order to cope with the expected future event rates, whereas the other subsystems only have to be upgraded partially [55].

The current electromagnetic and hadronic end-cap calorimeters will suffer significant radiation damage by 2023 and will be fully replaced with a new system called the High Granularity Calorimeter (HGCAL) [56]. The electromagnetic end-cap calorimeter will be constructed out of Tungsten absorbing plates interleaved with Silicon sensors acting as detection layers. The hadron calorimeter will be split into two subsections, both exploiting brass as absorbing material. In the subsection closest to the LHC beam-pipe, Silicon will be used as detecting material, whereas plastic scintillators will be used in the outer section. The segmentation of the new system is going to be significantly increased, thus providing detailed three dimensional images of hadron showers.

The barrel section of the calorimeter will undergo an electronics upgrade, preserving the existing crystals and photodiodes [57]. The goal is to eliminate the present latency constraint of  $3.2\mu\text{s}$  by moving the buffering of the event data to the data acquisition system. In order to achieve this, the front-end electronics will transfer data from every bunch crossing. The upgraded electronics will also feature reduced shaping times of the signals, thus improving timing precision and leading to a timing resolution of the order of  $30\text{ ps}$  for high energy photons and hadrons [57]. Such a good timing resolution is crucial under high pile-up conditions allowing to improve the discrimination of the interaction vertices beyond spatial tracking algorithms.

In order to improve timing resolution for Minimum Ionising Particles (MIPs) down to  $30\text{ ps}$ , an additional MIP Timing Detector (MTD) will be inserted between the tracker and the electromagnetic calorimeter. The barrel section of the subdetector, will be made out of scintillating crystals combined with Silicon Photomultipliers (SiPMs). Due to radiation tolerance limitations, this technology can not be used for the MTD end-caps. Therefore, the end-cap region will be instrumented with Low Gain Avalanche Detectors (LGADs), which are Silicon sensors with internal gain of about 10 - 30. More details on the timing layer can be found in [58].

The muon system in the far forward region is currently comprised of four layers, or stations, of Cathode Strip Chambers (CSC) covering the pseudorapidity range  $1.5 \leq |\eta| \leq 2.4$ . In order to maintain good muon trigger acceptance, additional chambers will be added to extend the coverage up to  $|\eta| \approx 2.8$  [59]. Two of the new muon stations will be located in the region with higher magnetic field and comprised of Gas Electron Multiplier (GEM) chambers, as

they provide better position resolution, while the other two stations will be enhanced with low-resistivity Resistive Plate Chambers (RPC). In addition, the electronics of the existing muon system will be upgraded to deal with the future data rates.

The data acquisition and control system will be upgraded in order to provide extended bandwidth capabilities. The data reconstruction, analysis, storage and access algorithms will be improved in order to account for the increased data rates. The beam radiation protection and luminosity measurement systems will be upgraded due to the increased radiation level and the aging of the existing systems.

## 2.3. Outer Tracker Upgrade

The present CMS tracker was designed to operate without loss of efficiency up to an average pile-up of 50 for an integrated luminosity up to  $500 \text{ fb}^{-1}$  [55]. Under the expected pile-up conditions, the track reconstruction will become more complicated due to the increased track density, which brings up the requirement to increase the granularity of the front-end channels. In addition, the existing tracking system is able to handle a maximum trigger rate of approximately 100 kHz, whereas the maximum expected trigger rate at the HL-LHC is up to 750 kHz [55].

Both the CMS inner and outer tracker will be upgraded to match these challenges. In order to improve the event reconstruction efficiency of the CMS Level-1 Trigger, the outer tracker modules will contribute with information on high transverse momentum charged particles traversing the tracking system. The trigger information from the tracker will be combined with the one from the muon systems and calorimeters in order to form the L1 decision. This modification of the triggering system will allow for better identification of charged leptons ( $e$ ,  $\mu$ ,  $\tau$ ) and an improvement of their  $p_T$  determination. The primary and secondary vertex finding resolution will also be improved.

The concept behind this improvement exploits the magnetic field of 3.8 T inside the CMS detector. The trajectory of a particle traversing the detector subsystems in the magnetic field is bent in the plane orthogonal to the field vector. The bending radius of the trajectory is proportional to the particle momentum and will be used to identify tracks having high transverse momentum. A single outer tracker module, also referred to as  $p_T$  module, consists of two closely spaced sensors (see Figure 2.3). When a charged particle passes through a module, it leaves a hit in both sensors. Under the assumption that particle tracks originate from the beam-line, particles with a larger transverse momentum (the green line) will traverse the module under smaller incident angles than the ones with a lower transverse momentum (the red line). A transverse momentum threshold can be defined by the maximal distance between the hits in the top and bottom sensors. The module front-end chips will use a hit in the bottom sensor as a reference and require the presence of a hit in the top sensor within a programmable search window in order to pass the momentum threshold. In case

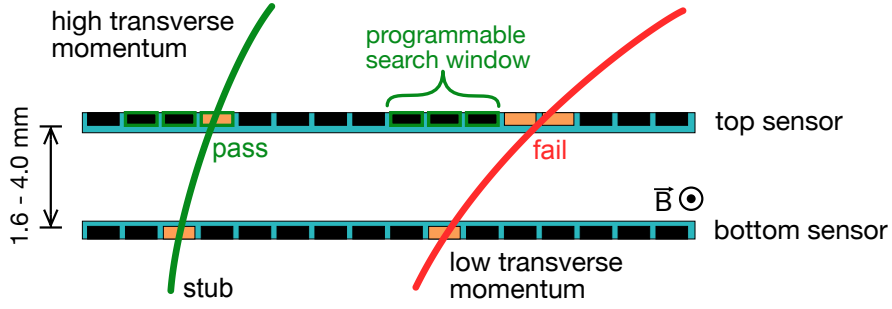


Figure 2.3.: Schematic representation of charged particles (green and red lines) with different momenta crossing a  $p_T$  module.

the selection criteria is satisfied, a matching pair of hits is described by the position in the bottom sensor and the deflection of the trajectory, and is referred to as stub, which is the minimalistic information describing both position and momentum of a trajectory.

In Figure 2.4 a schematic diagram of the data flow between the outer tracker modules and the back-end system is shown. Stubs are transferred to the back-end system at a rate of 40 MHz. The back-end system aggregates stubs from a number of modules and transfers them to the Track Finder (TF), which reconstructs tracks and forwards them to the CMS Level-1 Trigger. The Level-1 Accept (L1A) signal is propagated through the back-end system back to the modules. Once the L1A signal is received, a front-end module transfers the complete event information to the back-end system, which aggregates data and transfers them to the central CMS DAQ system.

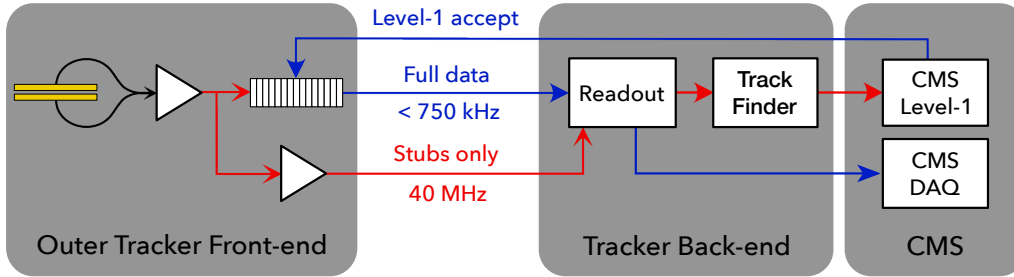


Figure 2.4.: Schematic diagram of the data flow from the outer tracker modules. Red arrows represent the trigger data path, whereas blue arrows represent the triggered hit data path.

**The Front-End Modules** The layout of the upgraded outer tracker is shown in Figure 2.5. It will be comprised of two types of front-end modules [61], where the first type is built out of two Silicon strip sensors and is called Two-Strip Module (2S). The second type combines pixel and strip sensors and is referred to as Pixel-Strip Module (PS). PS modules will be located closer to the beam-pipe in the inner part of the outer tracker providing higher precision to

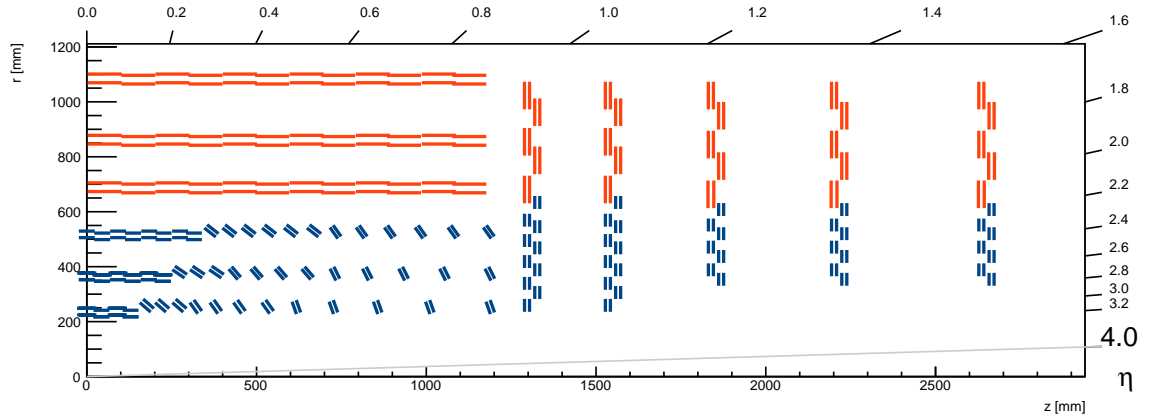


Figure 2.5.: R-z view of the layout of the new CMS outer tracker foreseen for the HL-LHC. The PS modules are shown in dark blue, whereas the 2S modules are shown in red. From [60].

constrain the origin of the trigger tracks. The outer part of the subsystem is built using 2S modules. Drawings of the 2S and PS modules are shown in Figure 2.6. Both module types are comprised of Silicon sensors, two symmetrically placed front-end hybrids, a power hybrid and a read-out hybrid. Two front-end hybrids are used to perform the module read-out due to the fact that each strip in both 2S and PS modules is split half along its length in order to provide higher channel granularity. In the 2S module, the read-out and power hybrids are combined in a single service hybrid.

Each sensor of the 2S module contains a matrix of  $2 \times 1016$  strips with a pitch of  $90 \mu\text{m}$ , the total area of a single sensor is approximately  $10 \text{ cm} \times 10 \text{ cm}$ . Each front-end hybrid contains eight front-end chips, called CMS Binary Chip (CBC) [62], which perform channel data sampling, stub generation, and hit data output after receiving the L1A signal.

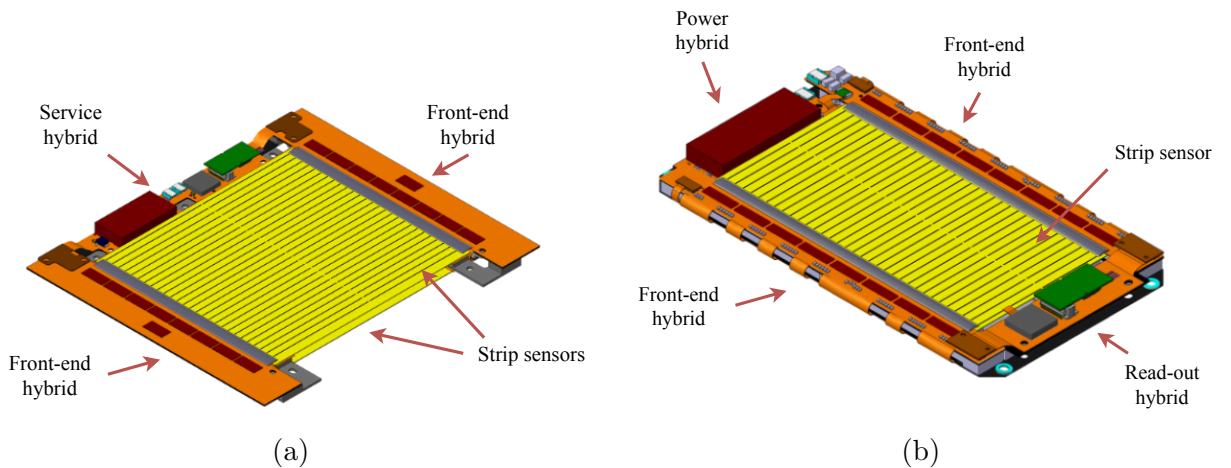


Figure 2.6.: Three-dimensional models of the 2S (a) and PS (b) modules. Strips are schematically represented by solid black lines on the sensors.

Both sensors of the PS module have a size of  $5\text{ cm} \times 10\text{ cm}$ , with the top sensor containing a matrix of  $2 \times 960$  strips with a pitch of  $100\text{ }\mu\text{m}$ . The bottom sensor contains an array of  $32 \times 944$  macro pixels with a size of  $1467.5\text{ }\mu\text{m} \times 100\text{ }\mu\text{m}$  each. The strip sensor is wire-bonded to the front-end hybrids, each containing eight Short-Strip ASICs (SSAs) [63], which transfer hit data to an array of Macro-Pixel ASICs (MPAs) [64] bump-bonded to the bottom pixel sensor. The MPA performs data read-out from the pixel sensor, clustering of strip and pixel data, and their correlation.

A schematic diagram of the data flow in the outer tracker modules is shown in Figure 2.7. The front-end chips mentioned above transfer data to the Concentrator Integrated Circuit (CIC), which performs the front-end data aggregation. One CIC per front-end hybrid handles data from all the front-end chips. On the read-out hybrid, data from both front-end hybrids are combined in the Low Power Giga-Bit Transceiver (lpGBT) chip. A data package is formed inside the lpGBT and transferred to the back-end system through the VTRx+ optical link [65].

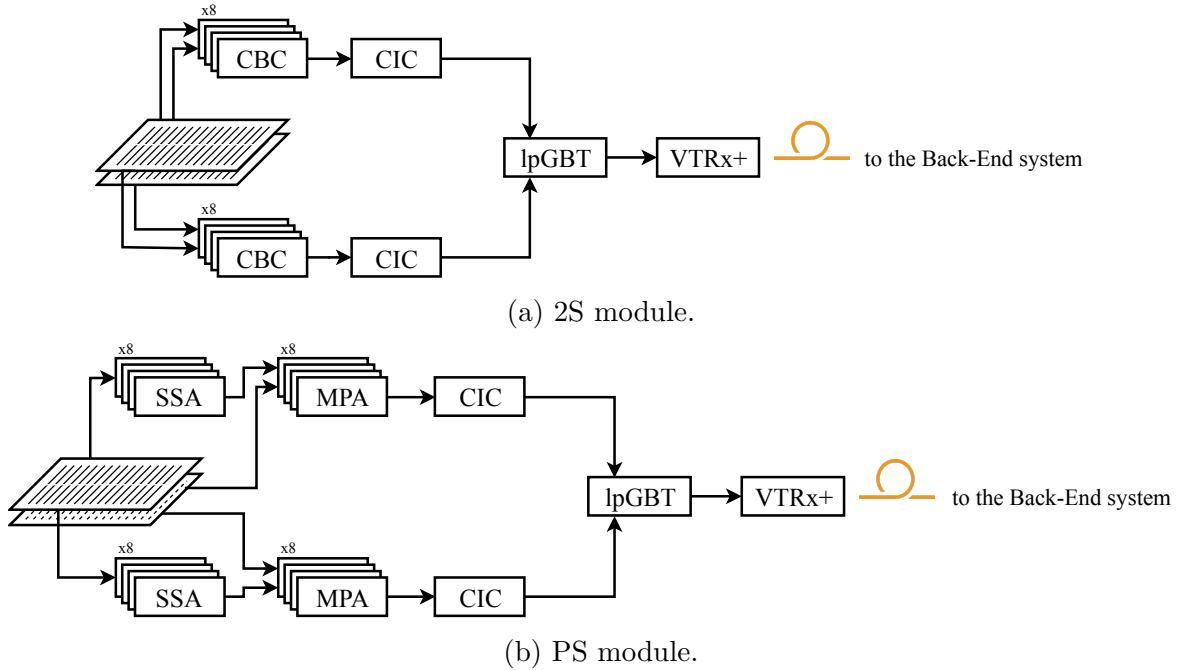


Figure 2.7.: Schematic diagram of the data flow in the outer tracker modules.

**Module Mechanics** Figure 2.8 illustrates a particle originating from the interaction point and traversing two  $p_T$  modules located at different radii. As can be seen, for the same particle momentum the distance between hits in the top and bottom sensors varies depending on the radial position of the module. Up to a certain extent, the  $p_T$  threshold can be equalised for these two modules by adjusting the discrimination window size, while in order to compensate the effect at larger radial positions, the sensor spacing has to be reduced. The 2S modules will be produced with a sensor spacing of  $1.8\text{ mm}$  and  $4.0\text{ mm}$ , whereas spacings of  $1.6\text{ mm}$ ,

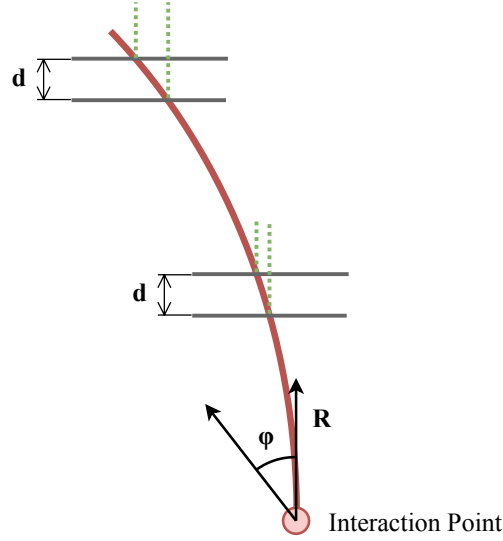


Figure 2.8.: Charged particle traversing  $p_T$  modules located at different radial positions.

2.6 mm and 4.0 mm are foreseen for the PS modules. A sensor spacing is provided by gluing the sensors to Carbon Fibre Reinforced Aluminium (Al-CF) spacers. The spacers also act as the thermal interface to the cooling system in the 2S modules, while in the PS modules they are used to remove the heat from the strip sensor through the pixel sensor, with the latter being cooled through the Carbon Fibre Reinforced Polymer (CFRP) base-plate. Similar to the current inner tracker, the upgraded CMS tracker will be cooled with the two-phase  $\text{CO}_2$  cooling system designed for a nominal coolant operating temperature of  $-35^\circ\text{C}$  [61].

**The Back-End System** The back-end system acts as an interface between the central CMS control system and the front-end modules. It will be implemented using DAQ, Trigger and Control Boards (DTCs), each controlling up to 72 front-end modules. Currently the DTC is in the prototyping stage, and several hardware configurations are being reviewed. A simplified diagram of a possible DTC structure is shown in Figure 2.9. It will be comprised of two FPGAs, implementing the communication with 36 front-end modules each and performing data formatting and aggregation. A high-rate stub data stream will be continuously delivered to the Track Finder (TF) with a latency of several microseconds, whereas the triggered hit data stream will be formed in the front-end modules only after receiving the L1A signal, aggregated in the DTC and transferred to the CMS DAQ. The on-board Central Processing Unit (CPU) will be used to perform configuration, control and monitoring of the DTC board and the front-end modules using the FPGAs as the communication channel with the last ones. The main drawback of the proposed structure is the necessity of additional synchronisation algorithms between the FPGAs, and therefore an option with a single more powerful FPGA is currently being reviewed.

Due to the fact, that the DTC system is in an active development phase, an intermediate back-end system was developed in the scope of this thesis in order to allow for module

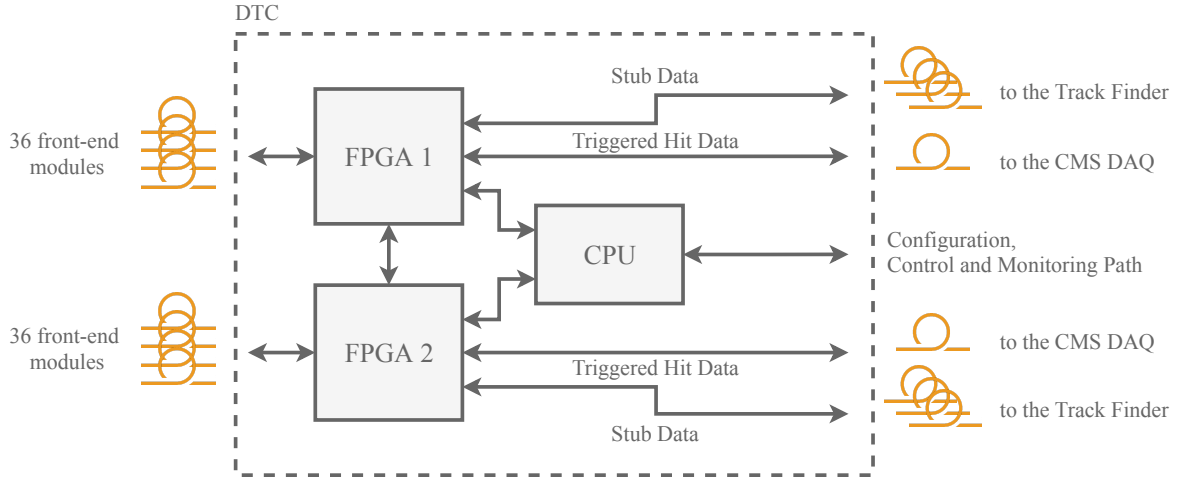


Figure 2.9.: Simplified diagram of the DTC structure.

prototyping and testing. This system is referred to as  $\mu$ DTC and will be discussed in detail in Chapter 3.

**The Track Trigger** The architecture of the stub processing system is shown in Figure 2.10. The outer tracker will be divided into nine sectors, called nonants, with 24 DTCs interfacing the modules in a single nonant. The Track Finder (TF) consists of a set of Track Finding Processors (TFPs) [66] represented by FPGA-based computing units, which perform reconstruction of tracks from a single processing nonant, being rotated by  $20^\circ$  in  $\phi$  with respect to the detector nonants. This creates a duplication region between processing nonants allowing to reduce the probability of truncating the tracks. Data from tracks in a single bunch crossing will be reconstructed by a single TFP within 450 ns. In order to maintain the 40 MHz event processing rate, a time-multiplexed technique is used, distributing the track finding

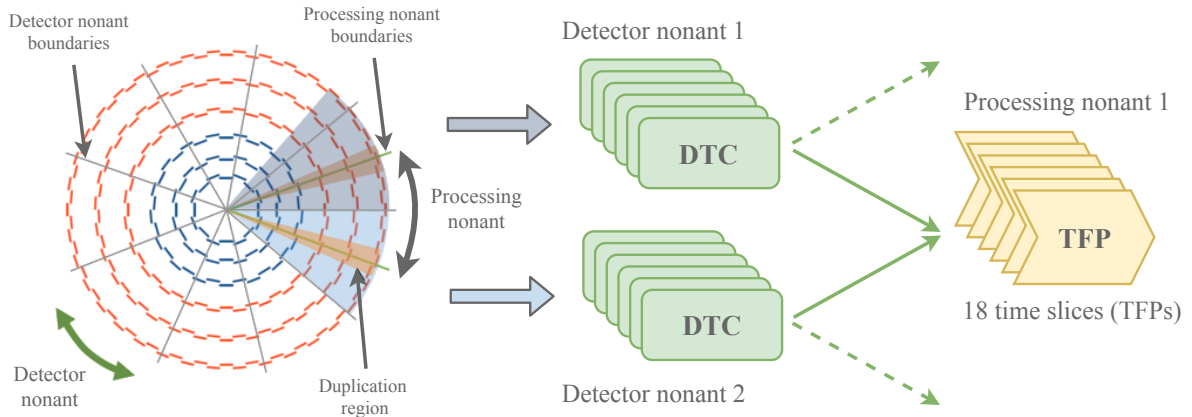


Figure 2.10.: Simplified diagram of the stub data flow in a single processing nonant. Grey and blue shaded areas represent two different detector nonants.



over 18 TFPs. As a result, 18 TFPs require 450 ns to reconstruct tracks from 18 consecutive bunch crossings, which corresponds to an effective processing time of 25 ns per bunch crossing matching with the system requirements. As already mentioned, the TFPs will transfer reconstructed tracks to the CMS Level-1 Trigger. A more detailed description of the Level-1 Trigger upgrade can be found in [67, 68].



## 3. $\mu$ DTC System Design

In the previous chapter the upgrade of the CMS experiment and in particular its outer tracker was introduced. As already mentioned, the module read-out and control during data taking at CMS will be performed by the DAQ, Trigger and Control Board (DTC), which is currently being developed. A variety of already available and planned module prototypes leads to the requirement for the development of an intermediate back-end system. The system has to support all hardware prototypes and allow for testing of the modules during production. The  $\mu$ DTC project was established to fulfil these needs, providing a back-end system based on the FC7  $\mu$ TCA-compatible board [69] and able to control up to 8 front-end modules.

This chapter will give an overview of the existing module prototypes, which dictate the requirements for the back-end system. The latter will be described thereafter with a focus on the FPGA firmware developed as a part of this thesis work. At the end of the chapter, a brief overview on the control software will be given.

### 3.1. Module Prototypes

The outer tracker modules were described in Section 2.3. Being mechanically and electronically complex devices, the modules will be based on a set of recently developed ASICs implementing the transverse momentum discrimination concept, introduced for the first time in a detector module. The ASIC and module prototyping phase is split into several stages and involves testing of the system at different levels of complexity.

**2S Prototypes** A schematic diagram of the communication chain in a 2S module is shown in Figure 3.1. At the initial stages, the CMS Binary Chip (CBC) is tested individually by connecting it directly to the back-end system using an electrical interface. Such a configuration is also referred to as electrical read-out of the CBC.

The development of the ASIC was divided into several steps. The first version [70] of the CBC provided basic read-out functionality, whereas a simplified transverse momentum discrimination logic was introduced in the CBC2 [71]. It allowed to proof the  $p_T$  module concept and only provided a stub presence bit, but no address or bending information of the stubs. Two modules equipped with two and eight CBC2 are shown in Figure 3.2, the

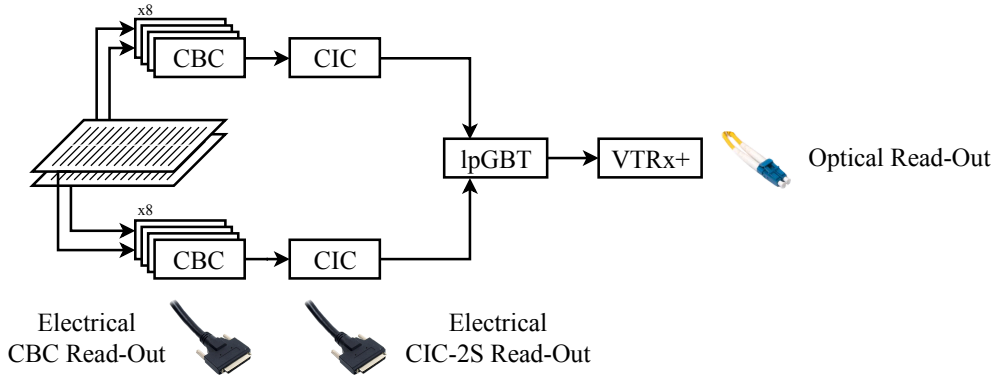


Figure 3.1.: Schematic representation of the internal communication chain of a 2S module with possible read-out options.

evaluation of their performance can be found in [72, 73]. A module prototype containing eight CBC2 chips connected to reduced-size sensors was tested at DESY within the framework of this thesis. The results will be discussed in detail in Section 5.1.

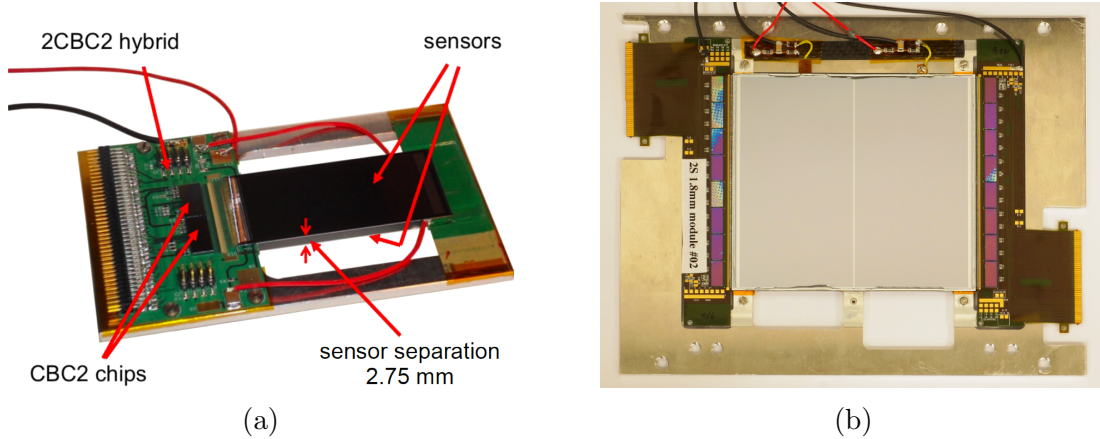


Figure 3.2.: Module prototype containing two CBC2 chips (a) [72] and the full-size CBC2-based 2S module (b) [61].

The third revision [74] of the CBC features the full functionality according to the 2S module specifications [61] and was followed by the CBC3.1 revision, which includes minor design improvements. The third generation of the CBC allows further extension of the front-end chain by connecting the CIC chip, with the configuration being referred to as electrical CIC-2S read-out (see Figure 3.1).

The first prototype of the complete read-out chain, which implements an optical communication, is shown in Figure 3.3. The front-end hybrid containing eight CBC3.1 chips is connected to the CIC chip, both being interfaced and powered using the 2S service hybrid prototype. As mentioned in Section 2.3, in the final system the lpGBT chip will be used to provide the data encoding for optical transmission. However, in the service hybrid prototype shown here, the lpGBT chip is replaced by a combination of the Giga-Bit Transceiver

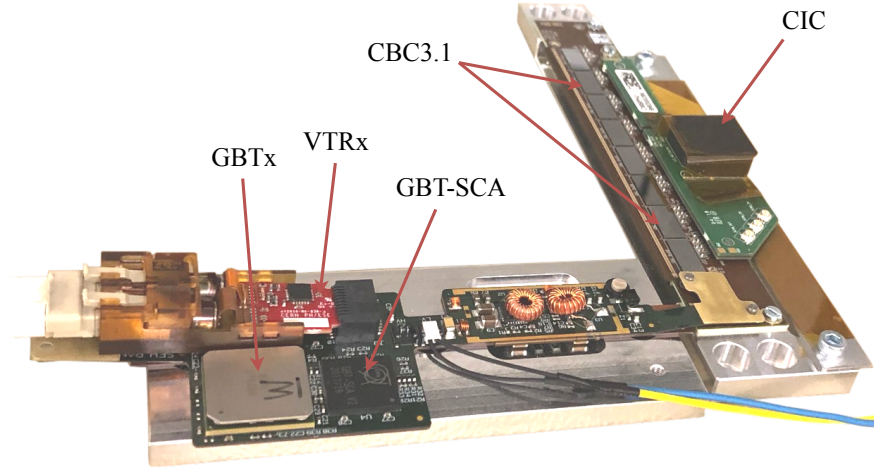


Figure 3.3.: Prototype of the 2S front-end hybrid connected to the service hybrid.

Chip (GBTx) and the GBT Slow Control Adapter (GBT-SCA) [75] due to the fact that the lpGBT chip is currently under development. The prototype allows to test the optical read-out with the  $\mu$ DTC and prepare for the final revision of the service hybrid exploiting the lpGBT chip.

**PS Prototypes** Similar to the 2S module, a schematic diagram of the communication chain inside a PS module is shown in Figure 3.4. The MPA and SSA prototypes were first available for testing in the beginning of 2018, providing the full functionality according to the PS module specifications [61]. Due to the higher number of components contained in the PS module, the initial testing steps involved individual qualification of both ASICs using an

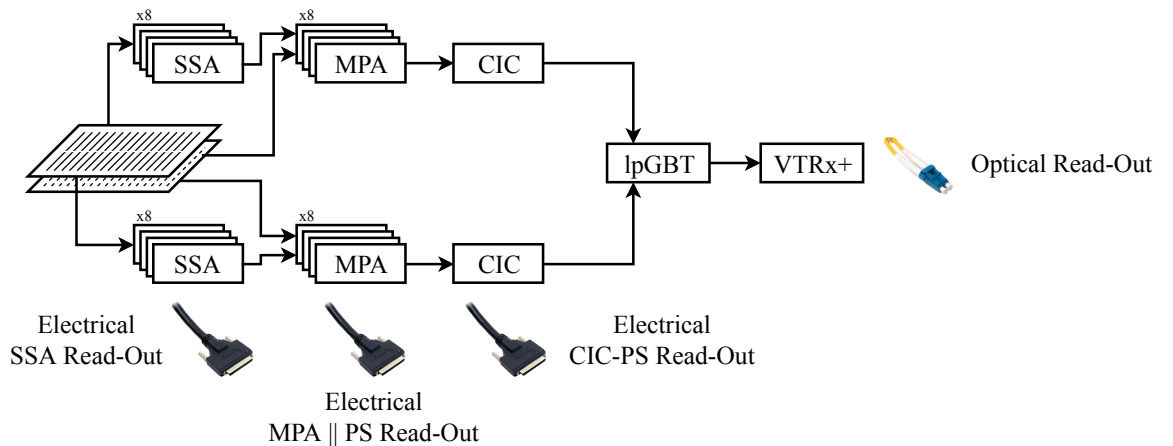


Figure 3.4.: Schematic representation of the internal communication chain of a PS module with possible read-out options.

electrical interface. The ASIC qualification was performed using standalone SSA or MPA assemblies and a combined MPA-SSA assembly, with the corresponding read-out chains being referred to as electrical SSA, electrical MPA or electrical PS read-out, respectively. The standalone MPA-based pixel assembly was successfully tested using particle beams, the results from one of the test beam campaigns will be discussed in Section 5.2.

## 3.2. Structure of the Read-out and Control System

The  $\mu$ DTC project was established to allow for testing of different revisions of the front-end ASICs and to provide an interface for controlling all the relevant module prototypes using electrical or optical interfaces. The  $\mu$ DTC is also intended to be used as the DAQ system for qualification during the module production and integration of the outer tracker. The system is based on the FC7 board, which will be described in detail in Section 3.3.

The structure of the read-out and control path in the  $\mu$ DTC system is shown in Figure 3.5. As an example, a front-end hybrid containing two CBC3 chips is shown connected to the interface board, which is responsible for the power distribution and the amplification of digital signals. An electrical interface cable between the interface board and the FC7 is not

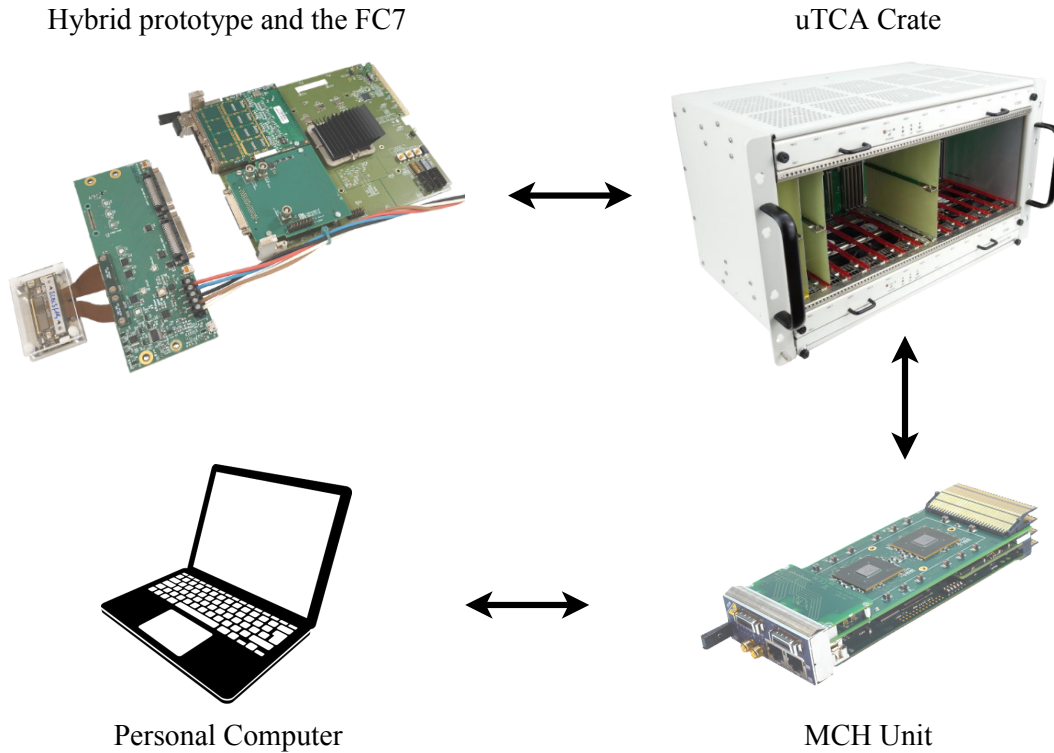


Figure 3.5.: Data flow diagram of the control system.

shown in the picture. The FC7 exploits the  $\mu$ TCA standard [76] allowing to combine several computing units, also called Advanced Mezzanine Cards (AMCs), in a single  $\mu$ TCA crate, where a  $\mu$ TCA Control Hub (MCH) unit is responsible for the system control, monitoring and data transfer to the PC at the rates compatible with the Giga-Bit Ethernet standard [77]. In order to allow for higher data transfer rates, additional data aggregation units may be installed in the  $\mu$ TCA crate. The FC7 can also be used without a  $\mu$ TCA crate, exploiting a dedicated adaptor to connect the board directly to a PC.

In order to customise the system for the read-out and control of the outer tracker modules, the FPGA firmware had to be developed. The work shown in this thesis aimed to fully design and implement the firmware for the  $\mu$ DTC project.

### 3.3. The FC7 Board

The FC7 is an AMC for generic data acquisition and control applications [69]. Built around the Xilinx Kintex-7 FPGA [78] it provides a custom platform with a large array of configurable inputs and outputs, primarily accessible via two on-board FPGA Mezzanine Card (FMC) sockets. A picture of the FC7 is shown in Figure 3.6, where the connected FMC card allows to interface four outer tracker modules using optical fibers. The FPGA itself is covered with a black heat-sink and is the key element of the FC7.

A Field Programmable Gate Array (FPGA) provides an array of basic logic elements organised in blocks and a highly-flexible configurable interconnect system between them, all complemented with a set of I/O blocks, see Figure 3.7a. A simplified structure of an FPGA logic block, also called slice, is shown in Figure 3.7b. There, a Look-Up Table (LUT) is a

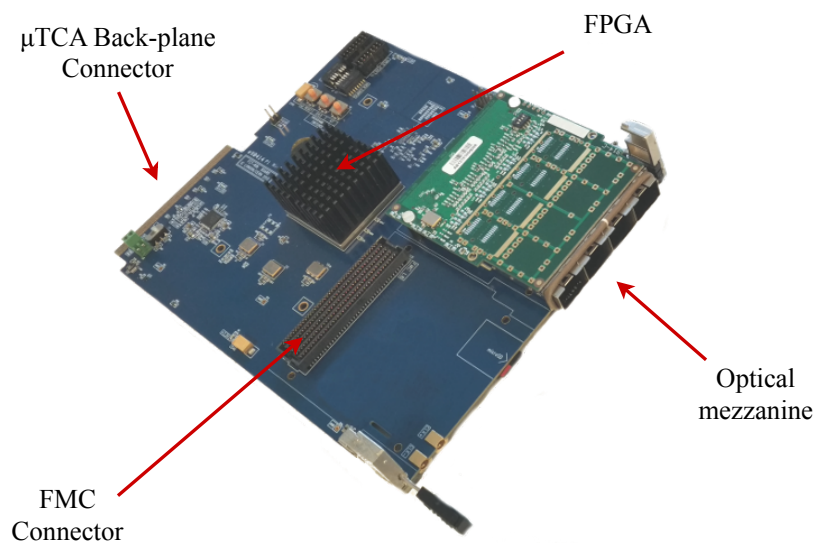
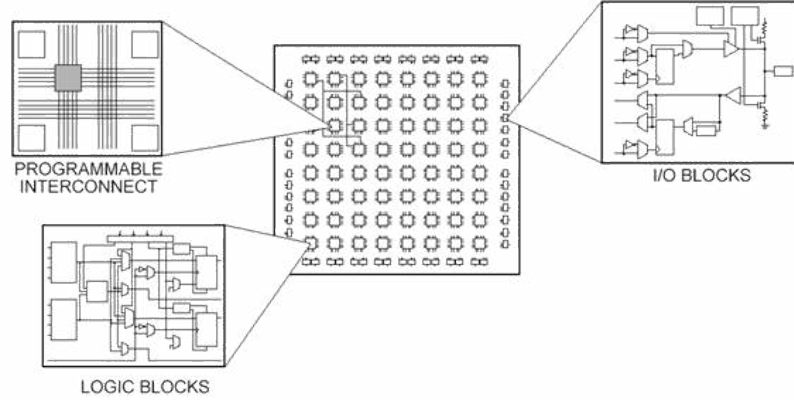
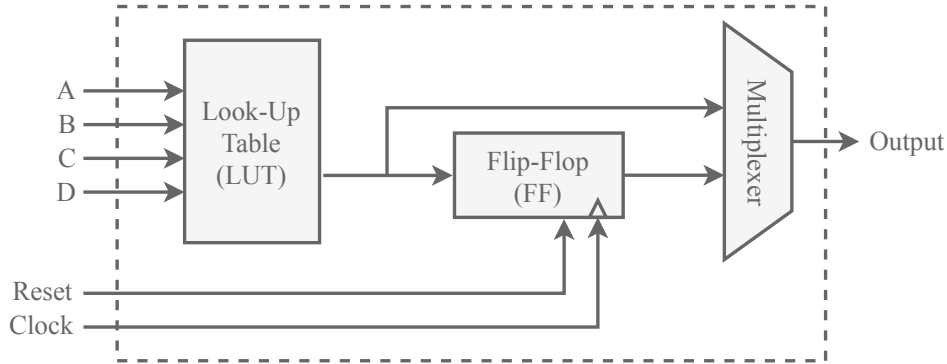


Figure 3.6.: Photograph of the FC7 AMC.

configurable truth table, the output signal from which depends on the condition of its inputs. From the LUT the output signal is further forwarded to a Flip-Flop (FF) controlled with clock and reset signals and allowing to store the received information. A Multiplexer (MUX) is used to select a desired slice output signal either directly from the LUT or after passing the FF. Actual FPGA logic blocks use more complex combinations and larger amounts of basic logic elements.



(a) Structure of an FPGA [79].



(b) Simplified diagram of an FPGA logic block, or slice.

Figure 3.7.: Illustration of the substructure of an FPGA.

The Kintex-7 FPGA used in the FC7 contains 74 560 slices having a varying structure and providing a total amount of 260 600 LUTs, 521 200 FFs and 89 580 MUXs [78]. The FPGA also provides 34 380 kB of Random Access Memory (RAM) distributed over the chip and optimised for intermediate data storage. All these resources allow the users to build logic circuits of any level of complexity by developing a dedicated FPGA firmware.

Apart from the FPGA, the FC7 also features a clock distribution ASIC, which allows to precisely control the frequency and the phase of the FPGA clock needed for various firmware parts. The DDR3 memory chip available on the FC7 is used as an intermediate data storage.

The FC7 board is equipped with a basic system firmware core, which implements the control of the FC7 peripheral elements, the  $\mu$ TCA functionality and the communication



protocol. The system firmware has to be complemented with user-specific firmware in order to extend the functionality of the FC7 for custom applications, such as the read-out and control of the outer tracker modules.

### 3.4. Digital Design

The basic requirements on the  $\mu$ DTC firmware are driven by the communication interfaces implemented in the outer tracker front-end ASICs. The configuration and tuning of the front-end chips is performed using a slow control interface, which exploits the Inter-Integrated Circuit (I<sup>2</sup>C) protocol [80] and provides data transfer at frequencies up to 1 MHz. In order to achieve synchronisation with the accelerator and the rest of the CMS detector, the bunch crossing clock has to be received by the back-end system and forwarded to the front-end modules, whereas trigger and other synchronisation signals are forwarded using a fast control interface. Event data are transferred to the back-end system using a data read-out interface, which is split into stub and triggered hit data paths.

The structure of the  $\mu$ DTC firmware is shown in Figure 3.8. The front-end modules are connected to the FMC connectors, shown on the left side of the diagram. The FC7 is connected to a PC through a  $\mu$ TCA crate or an adaptor using its back-plane connector

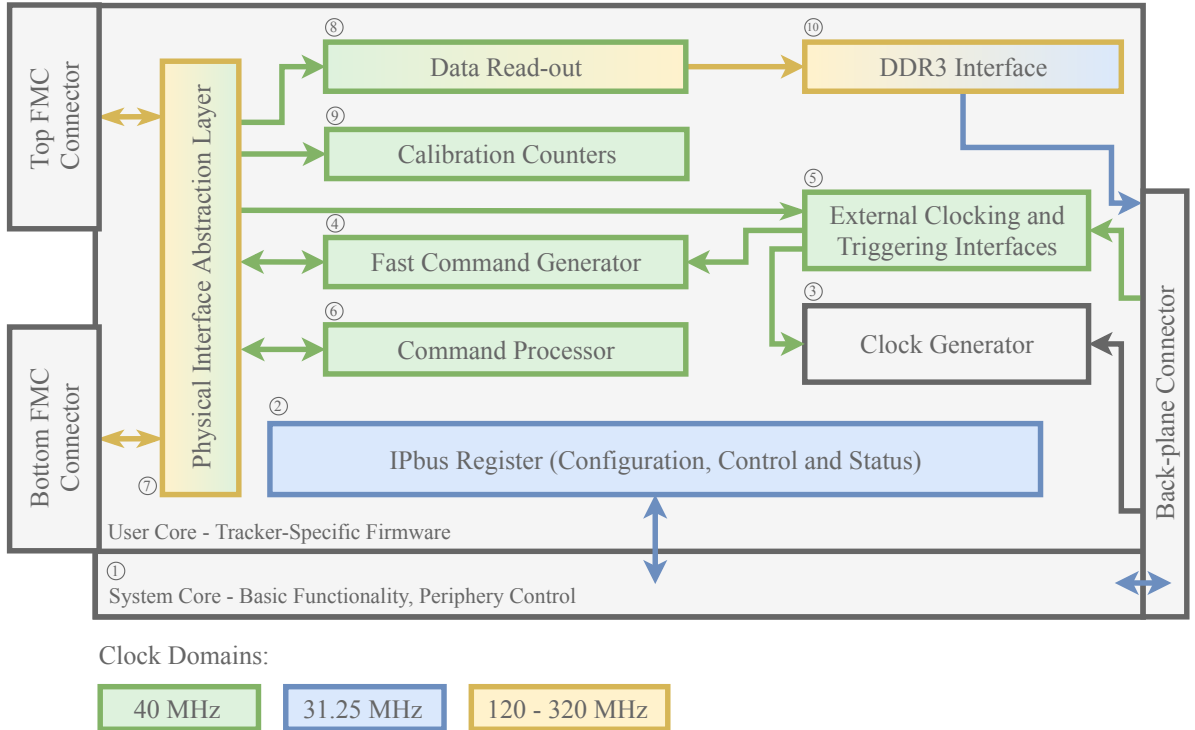


Figure 3.8.: Top-level diagram of the  $\mu$ DTC firmware. The colour coding represents different clock domains. Gradient colours correspond to a change of the clock domains.

shown on the right side of the diagram. Each block in the diagram represents a part of the firmware and is marked with a number used to refer to it in the text.

As discussed in Section 3.1, testing of the module prototypes is performed at different stages of the read-out chain, starting from the electrical communication with the front-end chips and ending with the optical read-out of a complete front-end module. The  $\mu$ DTC has to support all these read-out scenarios. The output data have a slightly different format for each front-end ASIC, and in order to deal with this and the other divergences introduced by different connection options, the firmware was divided into abstraction layers, which allowed to keep generic and common algorithms separated from the ASIC-specific ones. A Physical Interface Abstraction Layer (PIAL) was introduced in the back-end system, Figure 3.8(7). The common firmware blocks responsible for the event packing, control and triggering are all interfacing the hardware through this layer, in which the FPGA pin assignments and the low-level hardware interfacing are encoded.

An additional abstraction layer is marked in the diagram as the system core, Figure 3.8(1). As mentioned earlier, the system core is delivered together with the FC7 and does not require changes.

**IPbus Registers** The IPbus [81] is an Ethernet-based control protocol for devices exploiting the Telecommunications Computing Architecture (TCA). It includes both firmware and software, forming a communication layer between a TCA computing unit and a PC. The IPbus communication is organised in FPGA in 32-bit registers, which can be accessed or modified from the user software. A register can be responsible for the reset of firmware algorithms, thus bringing them to an initial state, or it can be assigned to perform configuration or status requests. In the  $\mu$ DTC the registers are divided into three main IPbus groups responsible for the configuration, control and status monitoring of the  $\mu$ DTC firmware, Figure 3.8(2). The corresponding information is distributed from the IPbus registers to the rest of the tracker-specific firmware. The arrows are not shown in the top-level diagram as IPbus registers are assigned to every single firmware block.

**Clock Generator** The algorithms running on the FPGA require a clock signal, which can be provided to the FC7 from the on-board oscillator, using the back-plane connector or the FMC connectors. The clock generator performs selection of a clock source and further distribution of the clock signals to the rest of the firmware logic. For a better overview, there are no corresponding arrows shown in the top-level diagram, Figure 3.8(3). As it is typical for LHC-based applications, a clock frequency of 40 MHz was chosen as the basic one for the  $\mu$ DTC, with certain algorithms running at higher or lower clock frequencies derived from the 40 MHz clock. The clock generator acts as a repeater of the 40 MHz clock, additionally generating the 120 MHz, 160 MHz and 320 MHz clock frequencies.

During a beam test or when installed in the CMS detector all operated front-end modules, and thus all the DAQ boards, are required to use the same external clock source in order to

achieve an optimal synchronisation between each other, while in the standalone operation the on-board oscillator is used as the primary clock source.

**Fast Command Generator** The fast command generator, Figure 3.8(4), implements a fast command interface used in the outer tracker front-end modules to keep the synchronisation during the data taking. Four types of fast commands are defined and can be sent at the bunch crossing frequency of 40 MHz:

- **Fast Reset** is used to synchronise the front-end modules by resetting buffers, state machines and counters on the front-end chips.
- **Orbit Reset** allows to reset bunch crossing and trigger counters on the front-end chips.
- **Calibration Pulse** triggers the release of a configurable charge into selected front-end channels, thus allowing to emulate a charged particle traversing a front-end module.
- **Level-1 accept** is used to trigger the read-out of event data.

The fast command generator allows to acquire these signals from external sources or generate them internally in a selected sequence. The firmware block provides the possibility to generate random triggers at a frequency in the range from 1 kHz to 1 MHz. For calibration and characterisation purposes, the fast command generator implements the possibility to send a sequence of calibration pulses followed by the trigger signals with a configurable delay. This helps to examine the physics data collection mode when a trigger signal is sent with a certain latency after a physics event.

The possibility to generate trigger signals based on the stub information received from modules is present and allows to operate the system in a self-triggering mode. The other external trigger sources will be introduced in the following paragraph.

**External Clock and Trigger Interfaces** When performing data taking with a combination of several modules, synchronisation is achieved by using a central control system which distributes clock and trigger signals to the modules. The  $\mu$ DTC implements a set of clock and trigger interfaces, Figure 3.8(5), which can be selected in the clock and fast command generators, respectively, using configuration registers:

- The **AMC13 Interface** implements the communication with the AMC13  $\mu$ TCA module [82]. The AMC13 is compatible with the existing CMS Trigger Distribution and Control System (TCDS) and is able to distribute these control signals through the back-plane of the  $\mu$ TCA crate.
- The **DIO5 Interface** allows for communication with the DIO5 5-channel Digital I/O FMC module [83], which is able to provide configurable outputs or inputs to the FPGA.

- The **Custom FMC Interfaces** in the  $\mu$ DTC provide the possibility to obtain trigger and timing information from custom designed FMC cards. For instance, the FMC card used to interface the CBC3-, MPA- and SSA-based module prototypes provides LEMO connectors suitable for such purposes.

**Command Processor** The configuration and calibration of the front-end modules and the monitoring of their status and the status of the  $\mu$ DTC is performed by the command processor, Figure 3.8(6). The present implementation has reduced functionality and provides only the slow control interface to the front-end modules. The command processor receives commands from the IPbus, and decodes and transfers them to the I<sup>2</sup>C master implemented in the PIAL.

The updated command processor will act as a task distributor between different firmware blocks, which perform slow control and status collection from the  $\mu$ DTC and the front-end modules, as well as the initial configuration and calibration of the modules. Such a structure will allow to reduce load on the IPbus communication channel by moving a set of algorithms from the user software to the FPGA, providing the possibility for testing the algorithms required for the final outer tracker read-out system where a single DTC will have to control up to 72 modules and the communication with the CPU has to be minimised.

**Physical Interface Abstraction Layer (PIAL)** The PIAL, Figure 3.8(7), provides the possibility to interface different front-end prototypes which use optical or electrical connections within a single DAQ system. A simplified structural diagram of the layer is shown in Figure 3.9. In order to communicate with the PIAL, generic interface formats were defined. Slow control and fast commands are sent to the PIAL using generic data buses, whereas in order to perform data read-out, a chip-agnostic event format was defined allowing to design a completely generic firmware block for the data read-out. The data read-out block will be discussed after the PIAL.

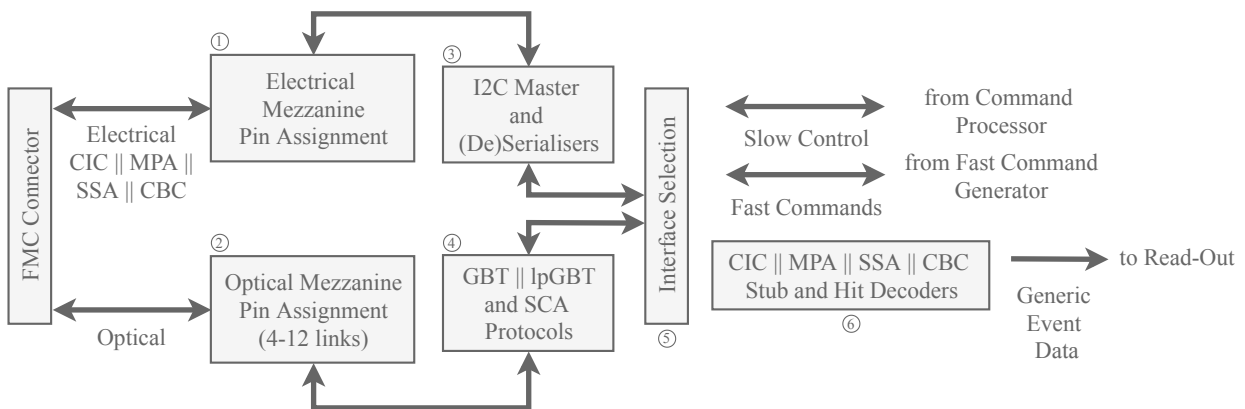


Figure 3.9.: Tree diagram of the abstraction levels inside the PIAL.

Prior to the firmware compilation, the user has to specify the type of the hardware interface, the number of the front-end hybrids and their type, as well as the amount and type of the chips used in a given module or prototype. If the electrical hardware interface is chosen, the I<sup>2</sup>C master and data serialiser, Figure 3.9(3), are instantiated in order to provide the slow and fast control interfaces correspondingly. Connections to the FPGA pins, Figure 3.9(1), are generated in the PIAL according to the pin assignment table defined for a given prototype. Using a dedicated FMC card, control commands are transferred to an interface board and forwarded to the front-end module. The read-out interface follows the way back, where after the pin assignment stage the deserialisers are used to recover the incoming data.

One of the prototypes, which implements the optical communication interface was shown in Figure 3.3. As already mentioned there, either GBTx or lpGBT transceiver chips can be used for the data transfer. On the back-end side, the communication with a transceiver chip is performed using the FPGA implementation of the (lp)GBT protocol, Figure 3.9(4), which assures encoding of the data and their further forwarding to a front-end module through an optical FMC card. The decoded data stream coming back from a transceiver chip contains the stub and triggered hit data in the same format as in the electrical read-out scenario.

Depending on the ASIC type, dedicated decoders, Figure 3.9(6), are used to decode stub and hit data at this stage and to form generic chip-agnostic event data, which are later forwarded to the data read-out.

**Data Read-Out** The processing and aggregation of data from all front-end modules connected to the  $\mu$ DTC are performed in the data read-out firmware block, Figure 3.8(8). The data flow diagram inside the firmware block is shown in Figure 3.10. Initially, the stub and triggered hit data decoded in the PIAL are buffered in order to allow for further processing. Triggered hit data are stored directly in the read-out buffers, Figure 3.10(1), whereas stub data are previously delayed, Figure 3.10(2, 3), in order to be later compared with triggered data and further verified. The buffering is performed independently for every read-out chip. In the final module design, the CIC is considered to be a read-out chip aggregating data from all the preceding ASICs in the chain, whereas in a hybrid prototype containing eight CBC chips that is interfaced electrically from the  $\mu$ DTC, each CBC is considered a separate read-out chip, increasing the amount of required read-out buffers by a factor of eight.

Buffered data from all the connected read-out chips are combined in a single event. The data aggregation is performed sequentially, therefore the event processing time is proportional to the total amount of chips in the system. In order to provide the required 750 kHz read-out rate for the front-end data, it should take a maximum of 53 bunch crossings to process a single event. This was achieved by using the 160 MHz clock for the processing, giving a factor of four benefit compared to the processing at the bunch crossing frequency. The time-multiplexed technique was used in order to further decrease the processing time by allocating several data aggregation nodes, Figure 3.10(5), and distributing events between them, thus reducing the effective processing time. The gain is proportional to the number of nodes, and their quantity has to be chosen based on the total number of front-end mod-

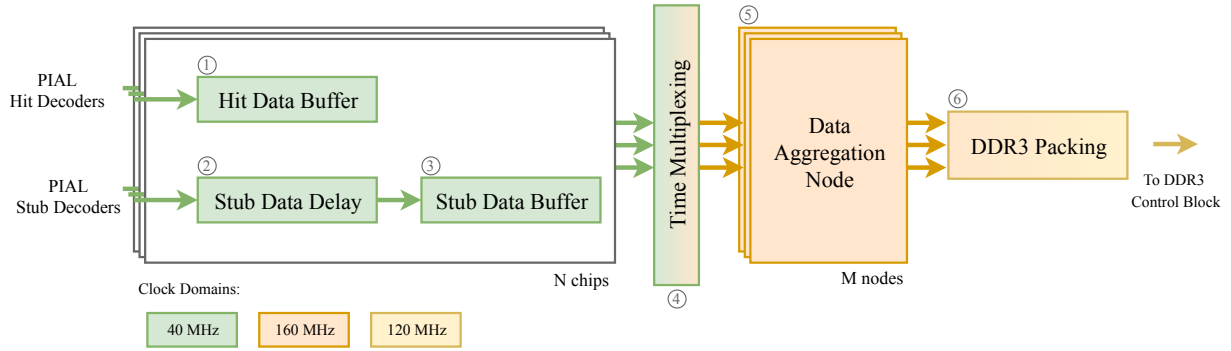


Figure 3.10.: Data flow diagram in the read-out block.

ules connected to the  $\mu$ DTC. The data aggregation nodes also append a header, containing general information about the event. Subsequently, the data are forwarded to the DDR3 interface, Figure 3.8(10), using a dedicated DDR3 packing controller operating at 120 MHz, Figure 3.10(6).

It has to be noted, that in contrast to the final DTC system, the  $\mu$ DTC does not transfer data to the central CMS DAQ or Track Finders using optical links. The data are acquired locally and further transferred to a PC using the IPbus protocol. Therefore, the read-out structure in the final system will differ significantly.

**Calibration Counters** In order to equalise the response of individual front-end channels, the front-end chips have to be calibrated. The most common approach is to measure the noise occupancy on the chip channels for different thresholds. To perform such a procedure a front-end chip is triggered several hundreds of times, then the data are transferred to a PC and processed in order to measure the noise occupancy for a given threshold. This procedure is repeated for different thresholds and takes several minutes for a single front-end module. In order to minimise the dead time of the detector system, the noise occupancy can be measured directly on the front-end modules or data acquisition boards, thus transferring only hit counts to the software algorithms. A dedicated algorithm was implemented in the  $\mu$ DTC in order to be tested and further used in the final DTC.

The front-end chips of the PS module (MPA, SSA) perform hit counting on chip. A dedicated firmware block records the counter output and transfers it to the PC. The CBC chip is not able to perform such a procedure. Therefore, in order to reduce the load on the IPbus communication channel, the counting procedure for the 2S modules is performed on the  $\mu$ DTC board, Figure 3.8(9). Counters are very resource consuming for an FPGA, and to create a counter instance for each channel in a single module, around 6 % of the FC7 FPGA resources would be required. This would result in around 50 % of the FC7 resources only to count hits from 8 modules simultaneously, excluding all the other aforementioned algorithms. In order to optimise the resource usage, the counters are shared between modules and the counting algorithm is executed sequentially. A configurable amount of counters is

instantiated in the  $\mu$ DTC, with one module assumed for the present explanation. Once the occupancy measurement command is received, a state machine on the  $\mu$ DTC activates one module, measures the occupancy and stores the hit counts in the read-out FIFO. While data are being transferred to the PC, the state machine activates the next module and performs the same procedure on this module. This allows to perform occupancy measurements in parallel to the read-out thus minimising the amount of time when modules are not used. This method is a compromise between the time performance and the FPGA resource utilisation. The first test results with emulated hardware already showed a factor of ten benefit in terms of consumed time compared to the conventional approach exploiting the full read-out chain.

### 3.5. Resource Utilisation

The resource utilisation for the aforementioned control and configuration algorithms, excluding the data read-out path, is shown in Table 3.1. The amount of resources used by these firmware components does not scale with the number of front-end modules. As discussed earlier, the utilisation for the 2S calibration counters is shown for the configuration with the number of counter instances sufficient for processing of only hits from one front-end module simultaneously. The slice utilisation represents the total fraction of logic elements used, whereas RAM usage corresponds to the memory utilisation. The utilisation of different logic elements (LUTs, FFs and MUXs) allows to identify a type of optimisation which can be performed. For instance, the measurement for the 2S calibration counters clearly

| Firmware Block          | Reference    | Resource Utilisation, % |      |      |       |      |
|-------------------------|--------------|-------------------------|------|------|-------|------|
|                         |              | Slices                  |      |      |       | RAM  |
|                         |              | LUTs                    | FFs  | MUXs | Total |      |
| System Core             | Fig. 3.8(1)  | 1.67                    | 1.16 | 0.05 | 2.67  | 2.51 |
| IPbus Registers         | Fig. 3.8(2)  | 2.20                    | 1.32 | 0.71 | 5.18  | 0.06 |
| DDR3 Control Block      | Fig. 3.8(10) | 3.84                    | 2.01 | 0.02 | 5.19  | 4.31 |
| Fast Command Block      | Fig. 3.8(4)  | 0.58                    | 0.26 | 0.08 | 0.87  | 0.24 |
| Command Processor       | Fig. 3.8(6)  | 0.16                    | 0.07 | 0.04 | 0.24  | 0.72 |
| 2S Calibration Counters | Fig. 3.8(9)  | 7.19                    | 6.36 | 2.70 | 16.99 | 0.48 |
| Other Logic             |              | 4.99                    | 2.85 | 0.03 | 2.19  | 2.51 |

Table 3.1.: FPGA resource utilisation for the common  $\mu$ DTC algorithms.

indicates high utilisation of both interconnects (LUTs) and memory registers (FFs), which can be optimised by sharing the interconnects. The total slice utilisation does not correspond to the sum of individual contributions due to the used resource packing strategy in the synthesis software. The total logic utilisation for all the common algorithms shown is approximately 30 %, which puts an approximate limit of 70 % on the resource utilisation for the data read-out path.

As already mentioned, the  $\mu$ DTC is intended to read data from up to 8 front-end modules. The resource utilisation for the full read-out chain is strongly dependent on the amount of the interfaced front-end modules, as shown for the 2S modules in Figure 3.11. The plot includes the resources used for the optical communication, hit and stub data decoding, their further buffering, aggregation and storing in the DDR3. The obtained results indicate the possibility to fit the desired read-out of 8 modules using less than 40 % of the FC7 FPGA resources.

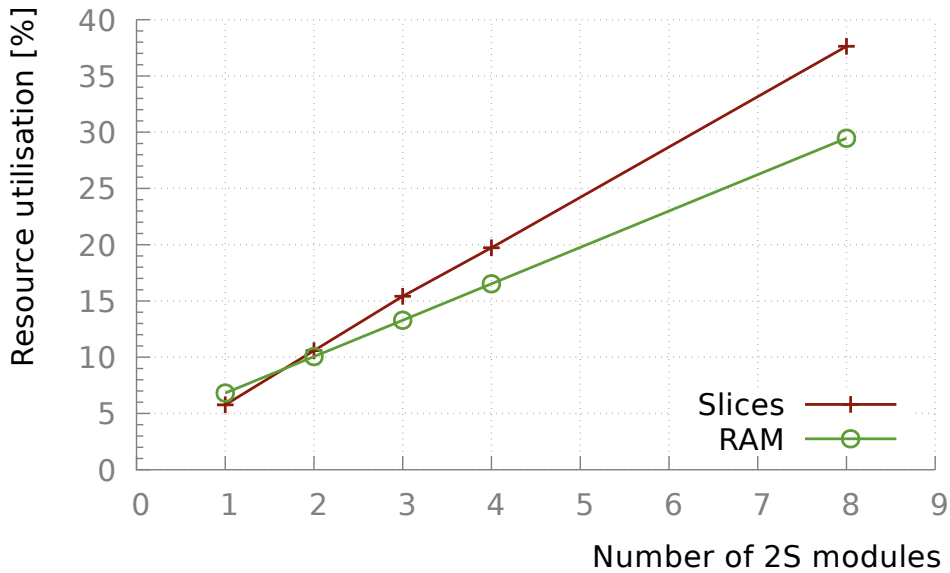


Figure 3.11.: Measured resource utilisation for the data read-out path for the 2S module system.

In Table 3.2 a detailed resource utilisation for the read-out of a single module connected the  $\mu$ DTC is shown. The resource utilisation summaries for the stub and hit data paths are shown separately, highlighting also the amount of resources required for the optical communication (lpGBT-FPGA) and data aggregation (Aggregation Nodes). The latter does not depend on the amount of modules connected and scales only with the amount of the data aggregation nodes instantiated. Four data aggregation nodes are sufficient to process data from 8 modules at the trigger frequency of 1 MHz. In the read-out path, around half of the logic and two thirds of memory resources are consumed by the stub data processing logic. In order to optimise the resource utilisation, the stub decoder can be restructured in order to allow for sharing of the decoding instances between several modules, this will



reduce the utilisation significantly. Additionally, in the final DTC the stub data will be sent directly to the Track Finders and therefore does not require to be delayed and buffered, a simplified monitoring path will be used for the stub data, storing them only for several modules simultaneously, and thus allowing to reduce the memory utilisation for the read-out path by a factor of three.

| Firmware Block            | Reference       | Resource Utilisation, % |      |      |       |      | RAM |
|---------------------------|-----------------|-------------------------|------|------|-------|------|-----|
|                           |                 | Slices                  |      |      |       |      |     |
|                           |                 | LUTs                    | FFs  | MUXs | Total |      |     |
| lpGBT-FPGA                | Fig. 3.9(4)     | 0.30                    | 0.25 | 0.01 | 0.55  | 0.00 |     |
| SCA-FPGA                  | Fig. 3.9(4)     | 0.28                    | 0.15 | 0.03 | 0.41  | 0.00 |     |
| CIC 2S Hit Decoder        | Fig. 3.9 (6)    | 0.70                    | 0.10 | 0.02 | 0.80  | 0.00 |     |
| Hit Buffering             | Fig. 3.10(1)    | 0.26                    | 0.20 | 0.08 | 0.48  | 0.96 |     |
| CIC 2S Stub Decoder       | Fig. 3.9(6)     | 1.38                    | 1.38 | 0.00 | 2.02  | 0.00 |     |
| Stub Delay and Buffering  | Fig. 3.10(2, 3) | 0.26                    | 0.14 | 0.10 | 0.40  | 2.28 |     |
| Aggregation Nodes (all 4) | Fig. 3.10(5)    | 0.75                    | 0.28 | 0.01 | 1.11  | 3.59 |     |

Table 3.2.: Detailed FPGA resource utilisation for the read-out of a single module connected to the  $\mu$ DTC.

The presented measurements also allow to estimate the resource utilisation in the final DTC. According to the preliminary design considerations for the DTC, a single board may consist of two Xilinx UltraScale+ XCKU15P FPGAs [84], each responsible for the read-out of 36 front-end modules. This FPGA provides two times more slice and memory resources than the one used in the FC7. The extrapolation of the read-out path resource utilisation shown in Table 3.2 to 36 modules would result in around 83 % of slice and 60 % of memory resources of the UltraScale+ FPGA. This estimate includes only the resources required for the optical communication (lpGBT-FPGA, SCA-FPGA) and for the hit and stub data decoders. An additional resource margin is required for data aggregation and monitoring algorithms, as well as for the data transfer towards the TFs and the central CMS DAQ. The optimisation can be achieved by excluding the front-end verification functionality and optimising the implementation towards the final application.

All the above allows to conclude that the resources available on the FC7 board are sufficient to implement the read-out and control of 8 front-end modules, leaving a margin of approximately 30 % of logic and 60 % of memory resources. In addition, the present resource utilisation was projected towards the future DTC system, providing a worst case estimate

on the required resources. The existing implementation of the read-out path would fit in the DTC board, but without providing sufficient free resources for the other algorithms, and therefore has to be optimised for the DTC use case.

### 3.6. Software

In order to control the  $\mu$ DTC board and to perform the data acquisition, the CMS Phase 2 Acquisition and Control Framework (Ph2 ACF) is used. The Ph2 ACF is a software implemented in C++ that provides the interface to the modules for the CMS inner and outer tracker upgrade. The framework is responsible for the configuration, control and calibration of the front-end modules, as well as monitoring of their status and the data acquisition.

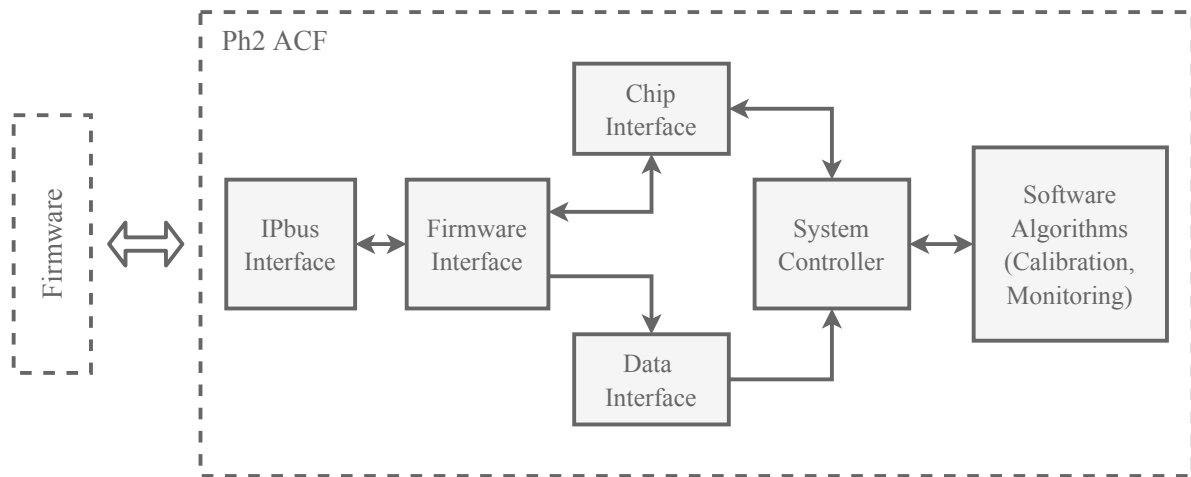


Figure 3.12.: Schematic diagram of the Ph2 ACF and the communication with the  $\mu$ DTC board.

The software is executed either on a PC, when interfacing the  $\mu$ DTC, or on the on-board CPU in case of the final DTC, see Section 2.3. The Ph2 ACF implements a set of abstraction layers shown in Figure 3.12. There, the communication with a DAQ board is established using the IPbus interface, while the firmware interface implements a set of methods providing the possibility to perform the initial DAQ board configuration, send the control, configuration or fast commands to the front-end, or acquire data. The chip interface provides the control and configuration methods for the front-end chips and currently supports all the existing outer tracker front-end chip prototypes. Support of the inner tracker prototypes is maintained as well. The data interface, similar to the chip interface, provides a chip-specific data interpretation layer. All the above mentioned parts of the software are supervised by the System Controller, which provides a global interface between the front-end modules and various software algorithms, performing the front-end calibration, monitoring and data processing.

The  $\mu$ DTC project provides a flexible and configurable DAQ and Control system for all the existing module prototypes and was successfully tested in the laboratory. The following chapters will focus on the test beam characterisation of the front-end modules using the system described in this chapter.



## 4. Beam Tests at the DESY-II Synchrotron

The outer tracker module prototypes were introduced in Section 3.1. These and the other existing prototypes have been extensively characterised in the laboratory, and their operation had to be further verified using particle beams. At test beam facilities, the beam parameters such as particle type, their energy and time distribution are well-known properties and allow to precisely characterise detection efficiency, position resolution and timing performance of a tested device. A sequence of beam testing campaigns was performed as a part of the outer tracker upgrade project, almost ten of which were carried out using the  $\mu$ DTC as the read-out and control system. The results from two of these campaigns performed at DESY are presented in Chapter 5. The first campaign was dedicated to the testing of a 2S module prototype based on the CBC2 chip, while the second one aimed to characterise a prototype of the pixel sensor assembly with the MPA front-end chip. In order to introduce the reader to the measurement campaigns, this chapter will describe the beam test facility at the DESY-II synchrotron, provide a description of the experimental setup used to perform the measurements, and finally discuss the data analysis strategy.

### 4.1. The DESY-II Facility

The Deutsches Elektronen-Synchrotron (DESY) accelerator began its operation in 1964. It was decommissioned after two decades of operation and a new DESY-II accelerator [85] capable of accelerating either electrons or positrons was built in the DESY tunnel in 1987. The magnet system of the old accelerator was reused by the DESY-III proton accelerator [86], which served as a proton injector for HERA [87] and was decommissioned in 2007. The DESY-II accelerator is 292.8 m long and has an average radius of 46.6 m, being able to deliver a particle beam with energies up to 7 GeV. At different periods of time, DESY-II was used as the beam source for experiments at DORIS, PETRA and HERA [88]. Currently the main use of the DESY-II accelerator is the injection of the particle beam into the PETRA-III storage ring [89]. In this operation mode, also referred to as the PETRA-III top-up mode, the accelerator has to deliver a particle beam to PETRA-III every few minutes [88]. The beam is fully extracted from DESY-II during this injection, whereas in between the injections the accelerator can be used for the test beam generation.

The timing and energy structure of the DESY-II particle beam is shown in Figure 4.1. The field in the DESY-II magnets oscillates with a period of 80 ms. One bunch of about  $10^{10}$  electrons or positrons is injected from the linear accelerator LINAC-II. In test beam generation mode the beam is then accelerated and decelerated twice during the two magnet cycles and dumped right before the next injection. The intensity is lower in the second magnet cycle due to beam losses.

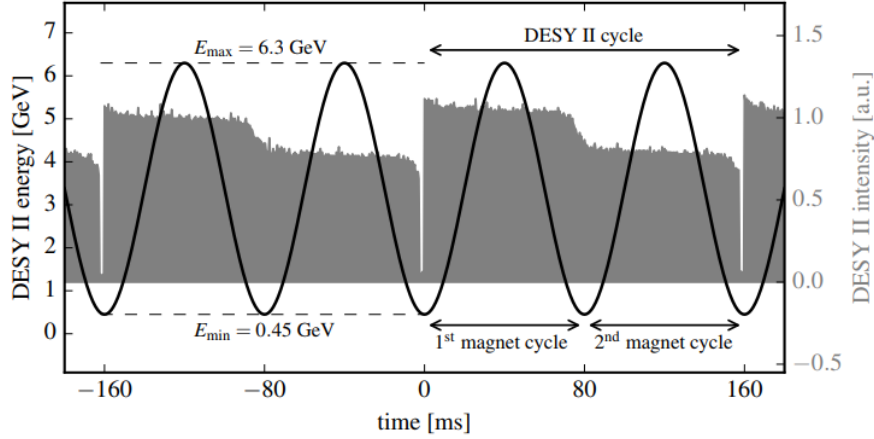


Figure 4.1.: DESY-II operation in the test beam generation mode [88].

The test beam generation is performed using double conversion, the corresponding diagram is shown in Figure 4.2. Initial Bremsstrahlung photons are generated by a carbon fibre target of  $25\ \mu\text{m}$  thickness installed in the DESY-II beam-pipe. The generated photon beam is then converted into electron-positron pairs using a converter target in the form of a Cu wire or Al and Cu plates of different thicknesses. A dipole magnet and a movable collimator are used to select the energy of the outgoing particles [90]. A beam shutter is available to switch off the beam in order to access the experimental area. The DESY-II beam test facility consists of three experimental areas named T21, T22 and T24. The areas are independent from each other, and parameters such as beam energy, collimation or shutter position can be controlled separately.

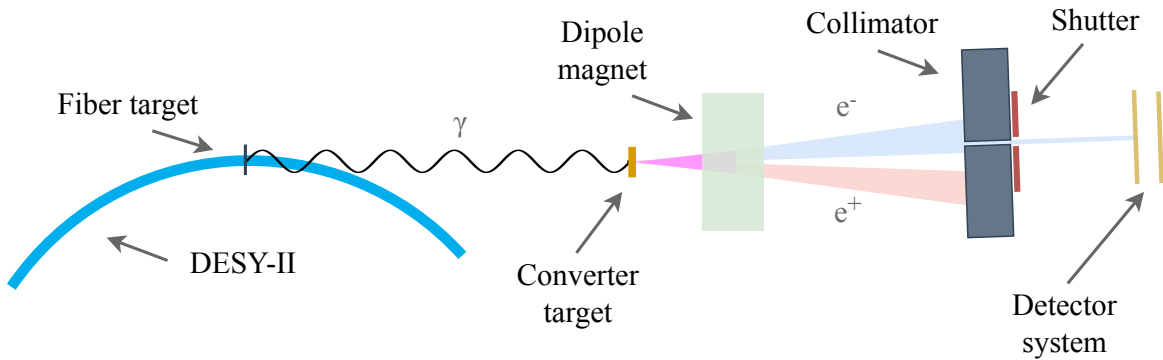


Figure 4.2.: Schematic diagram of the test beam generation at the DESY-II synchrotron.

The particle flux for different test beam particle momenta measured with telescope scintillators in the T22 experimental area is shown in Figure 4.3a. The peak flux is present for  $2.0 \text{ GeV}/c$  particles, while in order to minimise scattering of the beam, the momenta in the range from  $5.0 \text{ GeV}/c$  to  $6.0 \text{ GeV}/c$  are typically selected for test beam measurement campaigns. The particle occurrence for  $5.0 \text{ GeV}/c$  electrons is shown in Figure 4.3b and describes the probability of certain time intervals between test beam particles, considering that the DESY-II beam hits the target every  $0.976 \mu\text{s}$ . The measurement shows the most probable interval of approximately  $0.4 \text{ ms}$ .

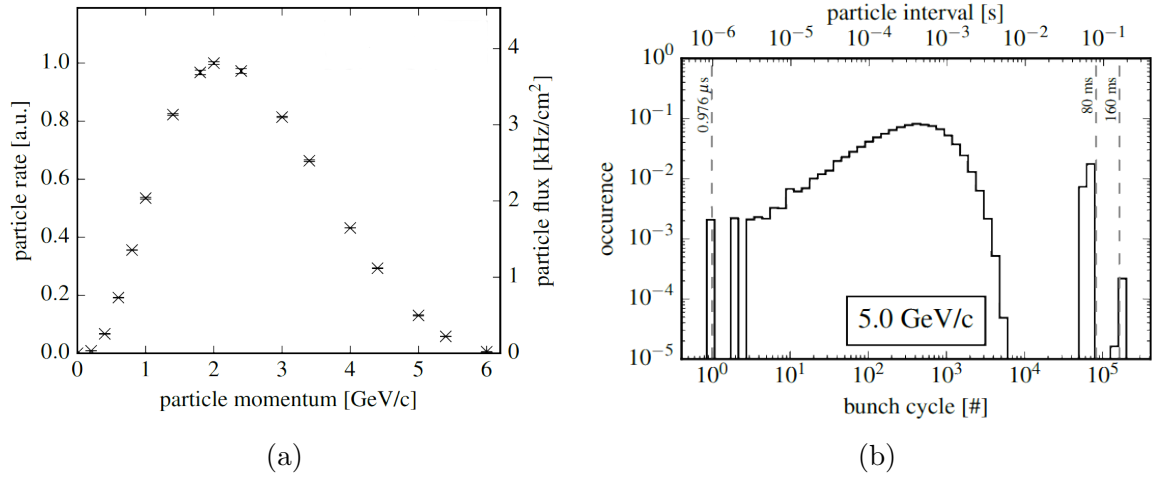


Figure 4.3.: Mean particle flux measured with telescope scintillators in the T22 experimental area (a) and the particle occurrence distribution for  $5.0 \text{ GeV}/c$  electrons (b) [88].

## 4.2. Beam Test Setup

A schematic layout of the setup used in both measurement campaigns is shown in Figure 4.4. In order to verify the performance of a Device Under Test (DUT), a dedicated tracking telescope is used. It allows to interpolate the position of a particle traversing the DUT and compare it with the DUT measurement. The used telescope consists of six Silicon sensor planes, while the DUT itself is mounted on a translation-and-rotation stage between these planes. The bold arrow in the schematics represents a particle traversing the telescope and being scattered in the detector planes. The trigger signal is formed using scintillating detectors located at either ends of the telescope. All the elements of the setup will be described in this section, the DUTs will be introduced in detail during the discussion of the results in the following chapter.

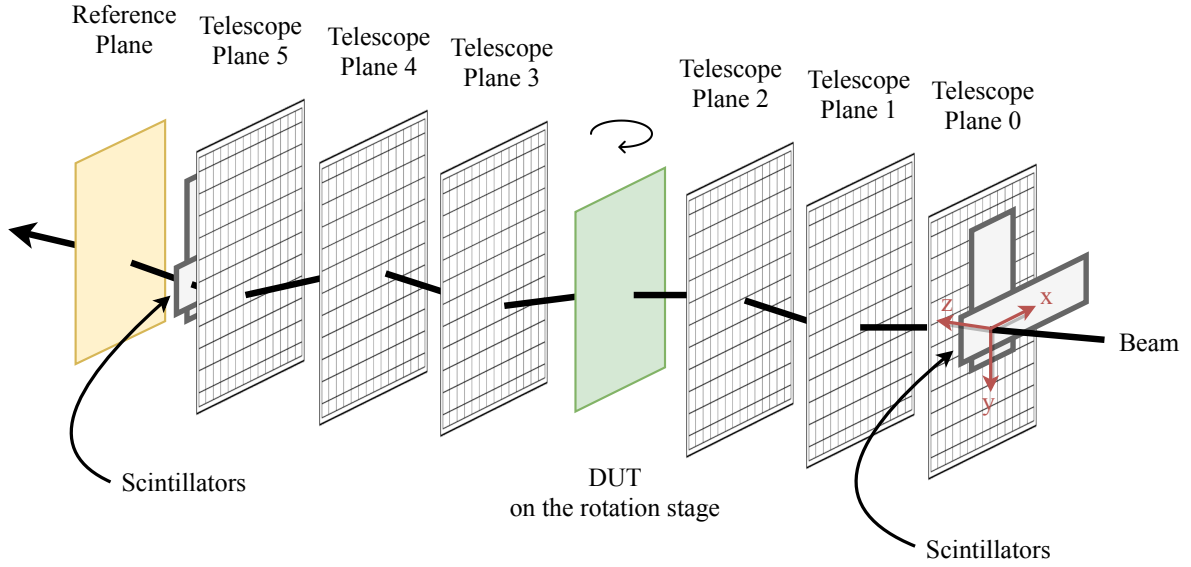


Figure 4.4.: Schematic geometry of the test beam setup.

#### 4.2.1. Beam Telescope

The above mentioned telescope belongs to the EUDET-type telescope family [91, 92], two of which are shown in Figure 4.5. The telescope consists of six MIMOSA 26 sensor planes [93], built using the Complementary Metal-Oxide-Semiconductor (CMOS) technology, which allows to integrate read-out electronics on the same substrate as the sensor itself, thus allowing to significantly reduce the amount of scattering material, or material budget, which is crucial



Figure 4.5.: EUDET-type telescopes at DESY [91].



for low energy beams as present at DESY. The MIMOSA 26 sensors provide a  $2.2 \text{ cm}^2$  sensitive surface with 1152 columns and 576 rows of pixels and a pixel pitch of  $18.4 \mu\text{m}$ , resulting in an intrinsic resolution of  $\sigma_{M26} = (3.24 \pm 0.09) \mu\text{m}$  [92]. The sensors have a thickness of  $50 \mu\text{m}$  and are placed inside aluminium boxes, which are mounted on a support structure. Each box is connected to a cooling system in order to keep the sensors at a constant temperature of  $18^\circ\text{C}$  for stable operation. The boxes feature openings for the beam passage on both sides, covered by lightproof polyimide films of  $25 \mu\text{m}$  thickness in order to reduce material budget [92]. Azalea, Datura and Duranta EUDET-type telescopes are used to perform test beam measurements at DESY.

### 4.2.2. Timing Reference

The EUDET telescopes operate in the rolling shutter mode, meaning that the read-out is performed sequentially, one pixel row after another. It takes  $115.2 \mu\text{s}$  to read the data from a complete sensor, and in correspondence to the particle occurrence interval shown earlier in Figure 4.3b, there is a non-negligible probability of having several tracks within a single read-out cycle. The track multiplicity for  $5.2 \text{ GeV}$  positrons in the Datura beam telescope can be seen in Figure 4.6 and shows a mean value of approximately 2.5 tracks. Also according to Figure 4.3a the particle occurrence interval is energy-dependent, which results in higher multiplicities for lower test beam energies. The sampling frequency of the tested outer tracker modules is  $40 \text{ MHz}$  and additional timing information is needed in order to match telescope tracks with the corresponding hits in the DUT.

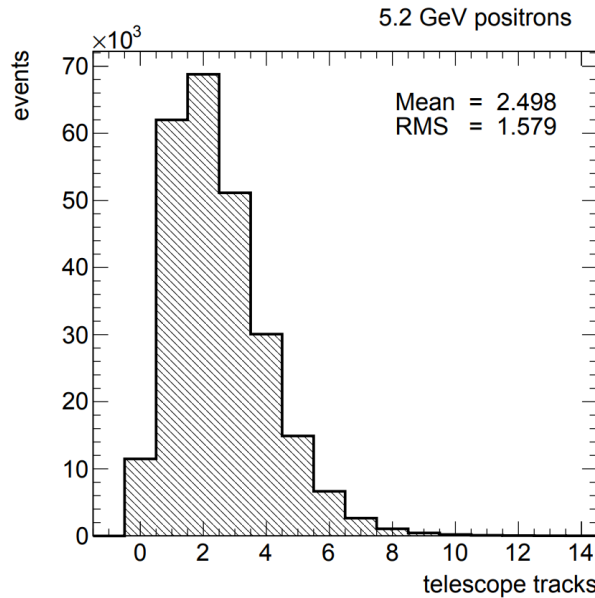


Figure 4.6.: Track multiplicity in the Datura beam telescope within a single read-out frame of the MIMOSA 26 sensors at a particle energy of  $5.2 \text{ GeV}$  [94].

A CMS Phase-I pixel plane [95] is used as a timing reference. Designed for the recent upgrade of the CMS inner tracker, the plane features a  $285\text{ }\mu\text{m}$  thick Silicon sensor with a pitch of  $150\text{ }\mu\text{m} \times 100\text{ }\mu\text{m}$ . The pixel plane performs sampling at a rate of 40 MHz, which allows to use it for track matching by requiring a hit presence in the reference plane during the track reconstruction.

### 4.2.3. Triggering and Read-out

The telescope is equipped with four scintillator detectors each having a size of  $2\text{ cm} \times 1\text{ cm}$ . The scintillators are used to form a trigger signal and are placed in pairs before and after the telescope, as illustrated in Figure 4.4. The outputs of the scintillator Photomultiplier Tubes (PMTs) are connected to the Trigger Logic Unit (TLU) [96] which contains discrimination logic and allows to detect coincidences between any combination of scintillators. One pair of scintillators allows to select a coincidence window of approximately  $1\text{ cm}^2$ , while the coincidence of all four scintillators indicates a particle that passed all telescope planes. The TLU distributes the trigger signal synchronously to the telescope, reference plane and the DUT.

The control and read-out of the telescope is performed using a dedicated modular crate system [97]. The data are passed through a data aggregator in order to assure maximum bandwidth. The CMS pixel reference plane is controlled using a Digital Test Board (DTB) designed for lab and test beam operation of the pixel read-out chips used in the detector [98]. The  $\mu\text{DTC}$ , described in Chapter 3, is used to control the outer tracker module prototypes (DUTs). Additional details on the interface between the TLU and the  $\mu\text{DTC}$  are available in Appendix A.

## 4.3. Data Acquisition Software

Central control software has to be used to synchronise the data collection of all the DAQ systems included in the test beam setup. EUDAQ [99] is a data acquisition framework designed to fulfil this requirement. The framework is developed in C++ and primarily used with EUDET-type beam telescopes. A schematic of the EUDAQ architecture is shown in Figure 4.7. The framework is divided into a number of different processes, each communicating using the TCP/IP protocol. Control over the processes and their communication is established by a central supervising unit, also referred to as Run Control. Among the notable slave processes are the Log Collector, Hardware Producers, Online and Offline Monitors, and Data Collector. Each hardware item is controlled using its own producer, which defines the interface between device-specific software and the EUDAQ framework. Therefore, a dedicated producer has to be implemented for each newly integrated device. The EUDAQ framework allows to implement producers both in Python and C++ by provid-

ing language-specific templates. The corresponding producers for the  $\mu$ DTC system were implemented for the beam testing campaigns. The data are further transmitted from the producers to the Data Collector, which groups data from each producer per event and saves them to a local storage. The Log Collector is responsible for status and error collection from the other processes. The Online Monitor is an optional graphical tool based on the ROOT framework [100] and used to monitor data in real time. It allows to visualise channel data or build correlation plots, providing the possibility to check the synchronisation between all sensor planes during data taking.

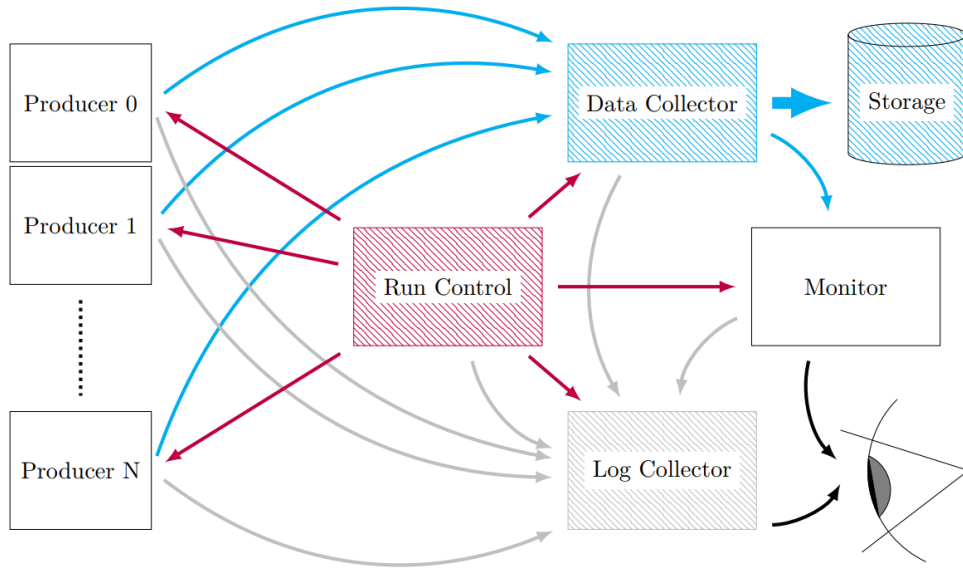


Figure 4.7.: Schematic of the EUDAQ architecture [94].

## 4.4. Offline Track Reconstruction and Data Analysis

The EUTelescope framework is used to process the accumulated raw data. The framework is a group of processors for analysing and reconstructing data collected with pixel beam telescopes [99, 101]. The main goal of this software package is to extract high level objects such as hit clusters or tracks crossing the telescope from the raw data. It fully supports the EUDET-type telescope family, while the processors to handle data from tested devices have to be implemented. The processor approach allows to flexibly analyse data all the way from the raw hit information to the final results. The processors are configured using configuration files, which also describe the geometry of a test beam setup. The processing flow in EUTelescope is shown in Figure 4.8.

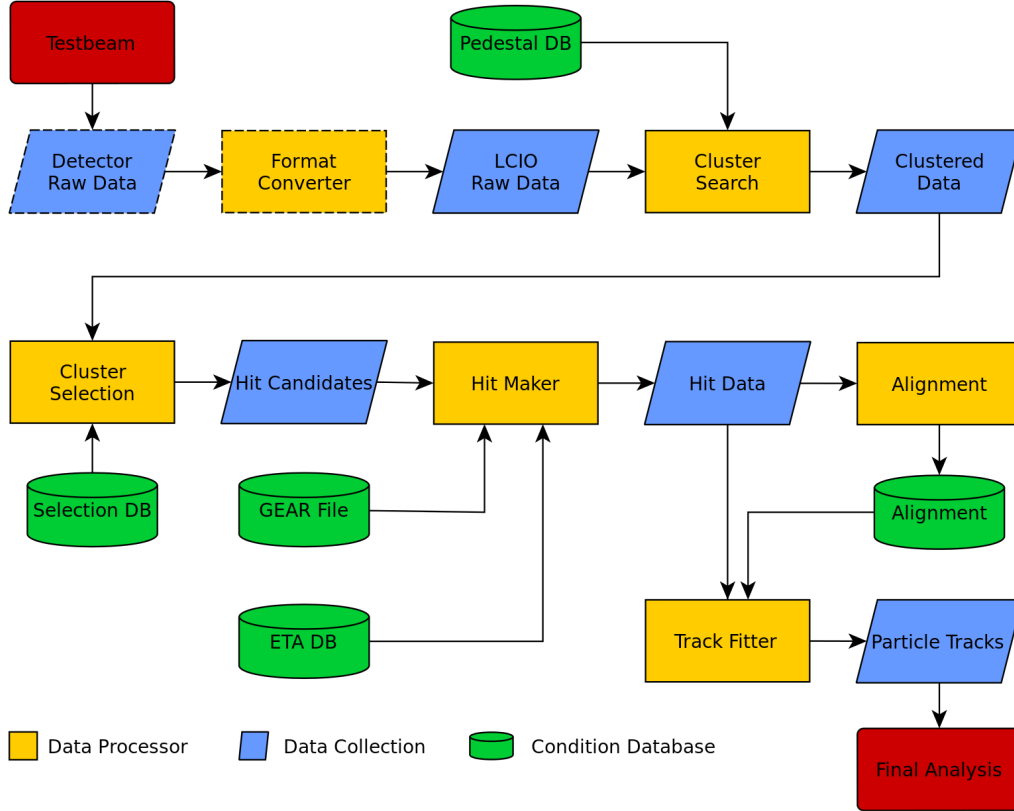


Figure 4.8.: Data processing flow diagram of the EUTelescope framework [101].

**Format Conversion** Raw data are converted into the Linear Collider I/O (LCIO) format [102]. The format describes a set of low- and high-level objects, such as raw channel data, clusters or tracks, and their hierarchical relation. Data from all the detectors are converted using dedicated converter plugins, or Format Converters. Additionally, at this step the hit rate is calculated for each pixel in order to form a noisy pixel database from the pixels exceeding the average hit occupancy across a sensor.

**Cluster Search** The charge created by a particle passing through a detector can be shared between neighbouring channels and the channel data have to be combined in groups of pixels in order to define the position precisely. Such a group is referred to as cluster, while the process of grouping the channel data is called clustering and can exploit different algorithms. The most widely used one is the Centre-of-Gravity (CoG) algorithm [103], in which the cluster centre is defined as the first raw moment of the cluster charge distribution

$$x_{CoG, Analog} = \frac{\sum Q_i \cdot x_i}{\sum Q_i}, \quad (4.1)$$

where  $x_i$  denotes the coordinate of a channel belonging to the cluster,  $Q_i$  is the charge above threshold measured in this channel. The pixel reference plane features an analog read-out

using integrated ADCs, and the CoG algorithm allows to get a weighted position of the cluster centre. Binary systems such as the MIMOSA 26 sensors or the outer tracker modules do not provide charge information, which results in a simplification of Equation 4.1

$$x_{CoG,Binary} = \frac{\sum x_i}{N}, \quad (4.2)$$

where  $N$  is the total number of channels forming a cluster. The resulting formula provides a good estimate for the centre position, but has lower precision due to threshold discrimination applied in binary systems.

**Coordinate Transformation** In order to correlate the data between planes, the reconstructed clusters have to be translated into a common telescope coordinate system, with the corresponding processor being called Hit Maker in the EU Telescope framework. The Geometry API for Reconstruction (GEAR) [104] is used to define the geometry of the test beam setup. It uses configuration files to define the position and rotation of the sensor planes, the number of contained pixels and the sensor pitch. The global telescope reference frame is chosen in a way that the origin is located at the centre of Telescope Plane 0, see Figure 4.4. For historical reasons the cluster positions translated into the telescope reference frame are called hits in the EU Telescope framework, therefore the original sensor channel hits will be referred to as raw hits from here on.

**Alignment and Track Reconstruction** After particle hits are created in the previous step, the track fitting is to be performed. The precision to which the geometry is known is much lower than the desired micrometre resolution of the telescope, making an additional telescope alignment necessary. The process starts from a pre-alignment procedure, where the offsets of the telescope planes are calculated with respect to a single fixed plane by building the histograms containing distances between particle hits in the compared detector planes, with such histograms being referred to as hit residual histograms. This procedure corrects for shifts in the x- and y- coordinates and has a precision of the order of hundreds of micrometres.

A precise alignment involves the track reconstruction. From now on, a group of first three sensor planes will be referred to as upstream telescope planes, while the last three will be referred to as downstream telescope planes, see Figure 4.9. Initial track candidates are built by combining hits in the upstream and downstream telescope planes separately. Straight track lines are built using different hit combinations from the first and third planes in a group. Then the position of the hit in the second plane is interpolated using the track line. The distance between the interpolated and the real hit is referred to as hit residual and is labelled in Figure 4.9 as  $\Delta_u$  and  $\Delta_d$  for the upstream and downstream plane, respectively. If the hit residual is smaller than 400  $\mu\text{m}$ , the hit combination is accepted as the track candidate. The upstream and downstream track candidates are extrapolated to the nominal position of the DUT in between the telescope arms, allowing to calculate triplet-triplet residuals.

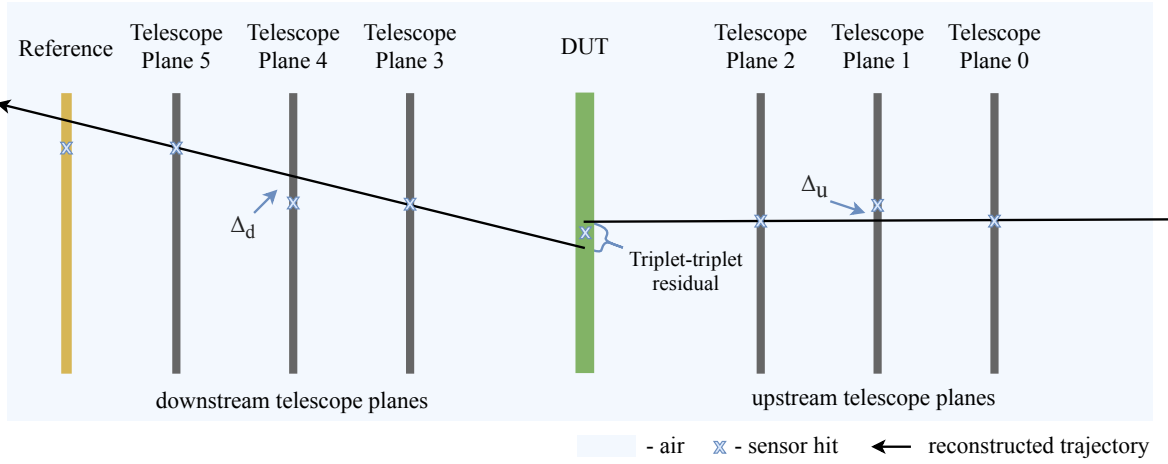


Figure 4.9.: Selection of track candidates.

All possible pairs of track candidates are checked for intersection and the matching ones are accepted for further analysis. Additionally, hit residuals for the DUT and the reference plane are calculated with respect to the upstream and downstream track candidate, respectively, and are also used to constrain the selection.

Charged particles are deflected when traversing the detector planes and the air between them, with the corresponding effect called multiple scattering and being mostly caused by Coulomb scattering off nuclei. The RMS of the particle angular distribution is defined by the parametric model [19]

$$\Theta^{RMS} = \frac{13.6 \text{ MeV}}{\beta c p} z \sqrt{\epsilon} \cdot \left[ 1 + 0.038 \ln \left( \frac{\epsilon z^2}{\beta^2} \right) \right], \quad (4.3)$$

where  $p$ ,  $\beta c$  and  $z$  are momentum, velocity and charge number of the incident particle, respectively, whereas  $\epsilon = \frac{x}{X_0}$  is the material budget of the scattering medium, which is defined as its thickness in units of the radiation length. Particle energy, type and the radiation length of a traversed material influence the amount of multiple scattering significantly, and the effect has to be considered for the 6.0 GeV DESY-II test beam. At the next track reconstruction step a more sophisticated model is therefore used to re-fit the earlier obtained track candidates. The General Broken Lines (GBL) algorithm [105, 106, 107] allows to build particle trajectories accounting for multiple Coulomb scattering. The track reconstruction procedure is schematically shown in Figure 4.10. There, the sensor planes are considered to be thin scatterers deflecting particle trajectories with an RMS defined by Equation 4.3. As the distance between the sensor planes is significantly larger than their thickness, the air gap is represented by two thin scatterers. The track fitting is the minimisation of a  $\chi^2$  function defined as [107]

$$\chi^2(\mathbf{q}) = \sum_{i=2}^{n_{\text{scat}}-1} \beta_i(\mathbf{q})^T \mathbf{V}_{\beta,i}^{-1} \beta_i(\mathbf{q}) + \sum_{i=1}^{n_{\text{meas}}} (m_i - \mathbf{P}_i u_i(\mathbf{q}))^T \mathbf{V}_{\text{meas},i}^{-1} (m_i - \mathbf{P}_i u_i(\mathbf{q})), \quad (4.4)$$

where  $\mathbf{q}$  is the track fit parameter vector,  $\beta_i$  and  $u_i$  are the predictions of scattering angles

and track hit positions, respectively, both depending linearly on the fit parameters. The hit residuals  $r_i = (m_i - \mathbf{P}_i u_i(\mathbf{q}))$  are defined as the difference between the measured values  $m_i$  and their predictions  $u_i$  projected in the measurement system using the projection matrix  $\mathbf{P} = \frac{\partial m}{\partial u}$ .  $\mathbf{V}$  are the co-variance matrices. The DUT and the reference plane are not included in the track finding procedure, and act only as scatterers.

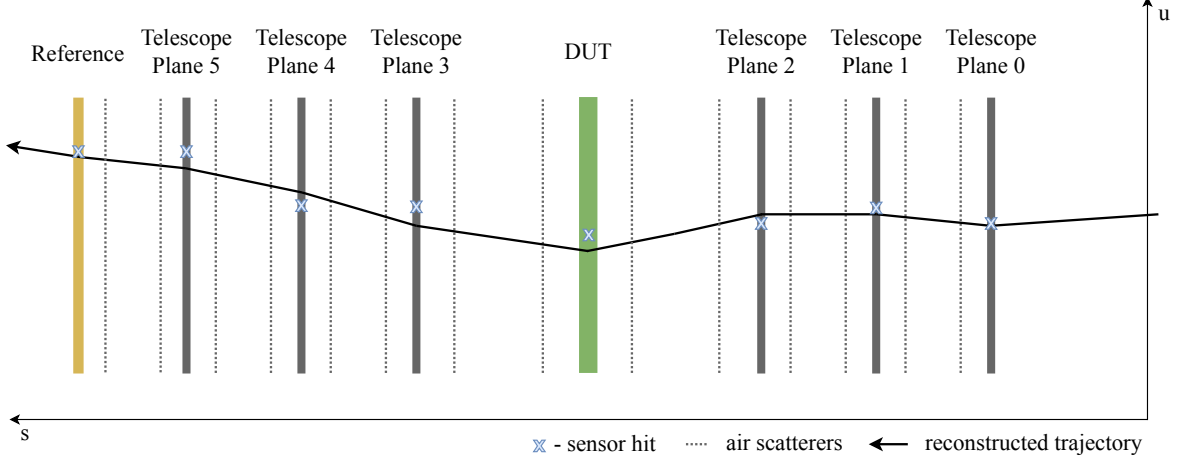


Figure 4.10.: Track reconstruction procedure involving GBL.

The reconstructed telescope tracks are used as the input to the Millepede-II algorithm [107], which minimises the global  $\chi^2$  and returns the alignment constants for each plane. Two out of six telescope planes are fixed due to the fact that the algorithm is insensitive to a common shift and rotation of all telescope planes. The alignment procedure usually has to be repeated several times, and the corrected hit positions are used as the input to the next track fitting and alignment iteration. Repeating this procedure with reducing the range of accepted residual values improves the precision of the alignment. In addition, the alignment constants for the DUT and the reference plane are calculated and applied at each alignment step.

After applying the alignment, the track reconstruction procedure has to be fully repeated to build the final tracks. The requirement on the matching hit presence in the reference plane is applied in order to account for the telescope track multiplicities of more than one track, as discussed earlier.

**Post Analysis** At each step of the data processing, the EUTelescope framework produces histograms, which are used for quality assurance during the reconstruction. Additionally, EUTelescope is able to output the reconstructed data into ROOT tuple files. This allows to use the ROOT framework for the post processing, such as extracting the detector resolution, efficiencies and other quantities after the reconstruction, without the requirement to repeat the reconstruction procedure itself. The analysis results will be presented in the following chapter.





## 5. Results of the Test Beam Measurements

In Chapter 2, the upgrade of the CMS detector was described introducing the concept of the  $p_T$  modules. Due to their complexity, a significant amount of different front-end prototypes has been produced. To facilitate testing of these prototypes, a flexible back-end system was developed and described in Chapter 3. Each prototype was tested in the laboratory in order to verify the functionality of the electronic circuits. A sequence of test beam campaigns was performed to proof the ability of the prototypes to efficiently detect particles and to operate synchronously with other detector systems. The results obtained from two of the measurements are presented in this chapter. Both measurements were carried out at the DESY-II facility, which was introduced along with the test setup and reconstruction algorithms in the previous chapter.

### 5.1. 2S Mini-Module Test Beam

The first test beam was focused on the evaluation of a 2S mini-module equipped with strip sensors of reduced-size and being the first outer tracker module prototype ever built at DESY. In addition, it was the first test beam involving the  $\mu$ DTC, therefore the verification of the DAQ system, as well as the study of the module assembly quality were the main goals of this campaign, which took place in November 2017. A set of measurements was acquired for different incidence angles of the impinging particles with approximately  $10^6$  events per point, and complemented with a detector threshold scan containing approximately 25 000 events per point.

#### 5.1.1. Module and Test Setup Description

The module is based on a hybrid prototype containing eight CBC2 chips. Each CBC2 has 254 read-out channels, half of which are connected to the top sensor and half to the bottom sensor. As mentioned earlier, each sensor of the final module will contain 1016 strips and will be sampled with eight CBC chips, whereas the tested prototype was built using reduced-size sensors with 127 strips each. In order to proof the efficiency of channels close to the inter-chip region, the sensors were bonded to two read-out chips, thus using only half of the channels

of each ASIC. Each sensor has a strip pitch of  $90\text{ }\mu\text{m}$ , matching the strip pitch of the final 2S sensors, whereas the thickness of the tested sensors is  $200\text{ }\mu\text{m}$ , in contrary to the final  $320\text{ }\mu\text{m}$  thickness [61]. The spacing between the two sensors is  $4.0\text{ mm}$  in this assembly. The module prototype is shown in Figure 5.1a, the bottom sensor is not visible in this top view. The module is powered through the interface board (not shown), whereas the high-voltage for the sensors is supplied through a separate connector. Based on probe station measurements in the laboratory, a bias voltage of  $350\text{ V}$  was determined to be optimal and sufficient to fully deplete the sensors. The  $\mu\text{DTC}$  was connected to the interface board using the VHDCI cable, the firmware was compiled to support the CBC2 hybrid containing eight chips.

The module support frame mounted on translation and rotation stages is shown in Figure 5.1b. Such a setup allows to compare the detector response for different incidence angles of the impinging particles. After finding the beam spot position and placing the module accordingly, both stages were disabled, due to the fact that they caused a significant increase in electromagnetic noise. During the measurements, the rotation stage was periodically powered in order to change the tilt angle of the module with respect to the particle beam.

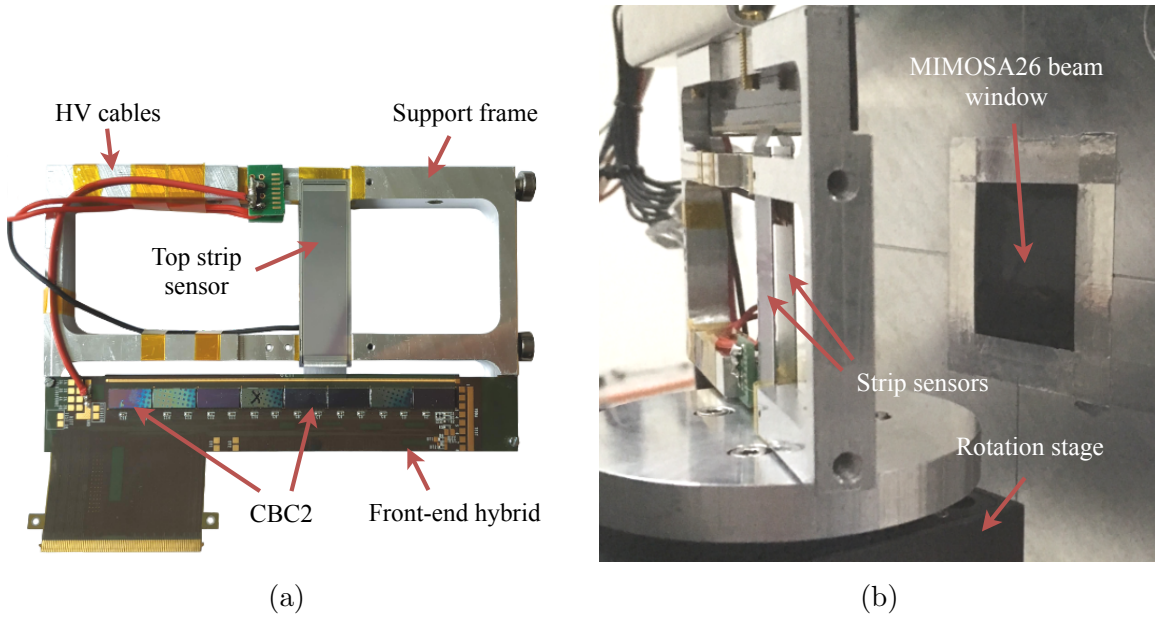


Figure 5.1.: 2S mini-module prototype shown standalone (a) and mounted on the rotation stage (b).

### 5.1.2. Calibration

Due to process variations during the ASIC production, the response of individual front-end channels within a single ASIC and between different ASICs is slightly varying. This means that the amplification and discrimination circuits have to allow the adjustment of the channel response, otherwise a charge sufficient to pass the discrimination stage would

vary from channel to channel and from ASIC to ASIC. In the CBC2, a common offset of the amplifier input allows to shift the electronic noise baseline, also known as pedestal, for all channels of a chip, whereas the individual channel response is set with per channel offsets. Both parameters have to be tuned in order to allow for an optimal front-end performance.

The tuning of the common amplifier offset is performed by scanning the threshold and measuring the average probability of having noise hits, also known as noise occupancy, defined as the number of noise hits in every channel normalised to the number of events collected at a given threshold. The threshold scan for one CBC2 channel is shown in Figure 5.2. The differential of the occupancy plot allows to determine the pedestal and its smearing caused by electronic noise. The pedestal is defined as the mean value of the differential distribution, whereas the electronic noise is determined as its standard deviation. The threshold scan is repeated for different amplifier offsets in order to find a point with an optimal pedestal level. In the outer tracker front-end modules the comparator threshold is measured in VCth (the **v**oltage **d**efining **c**omparator **t**hreshold) units, with one VCth unit being approximately equal to 380 electrons [108] and varying from chip to chip. In addition, in the CBC2 chip, a larger VCth value corresponds to a lower threshold. As mentioned above, the calibration is performed by extracting channel noise occupancy versus the comparator threshold. Due to the fact that the pedestal and noise are derived from the threshold scan, they are also measured in VCth units. During the operation in the test beam area, the pedestal was shifted to reside at a threshold of 153 VCth units. The individual channel response equalisation is performed by repeating the threshold scan and shifting the pedestal of divergent channels

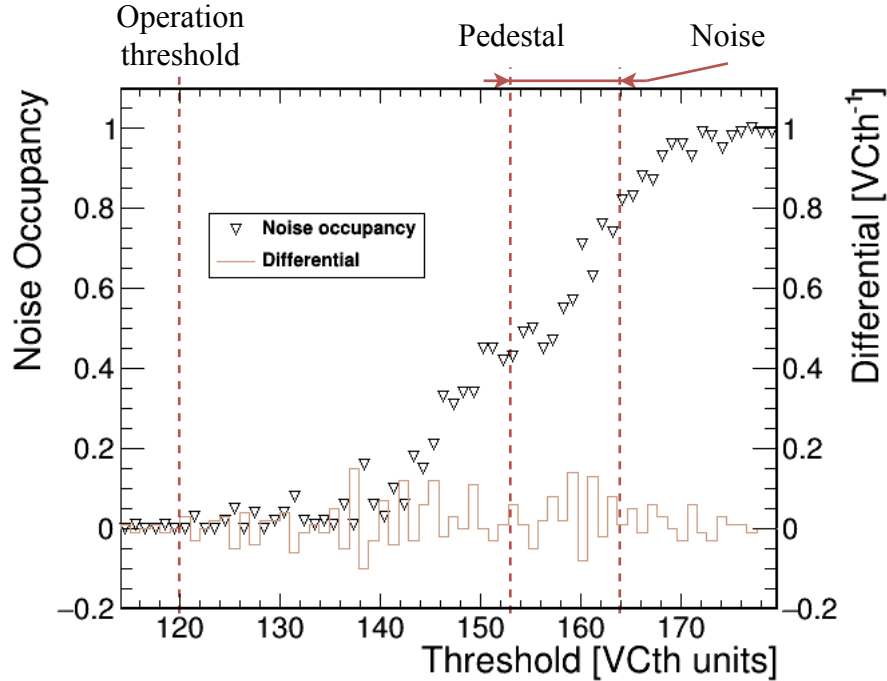


Figure 5.2.: Noise occupancy of one CBC2 channel for different thresholds. A higher VCth value corresponds to a lower threshold.

towards the tuned average value.

The measurement of the noise was performed after the equalisation and can be seen in Figure 5.3. The channels connected to the sensors show a standard deviation of about 11 VCth units for both chips, which corresponds to a charge of approximately 4200 electrons. Typical values for such front-ends are expected to be in the order of 1000 electrons [108]. The significantly higher value of the noise is caused mainly by the high electromagnetic noise in the test beam area and missing high-voltage filtering in the tested module.

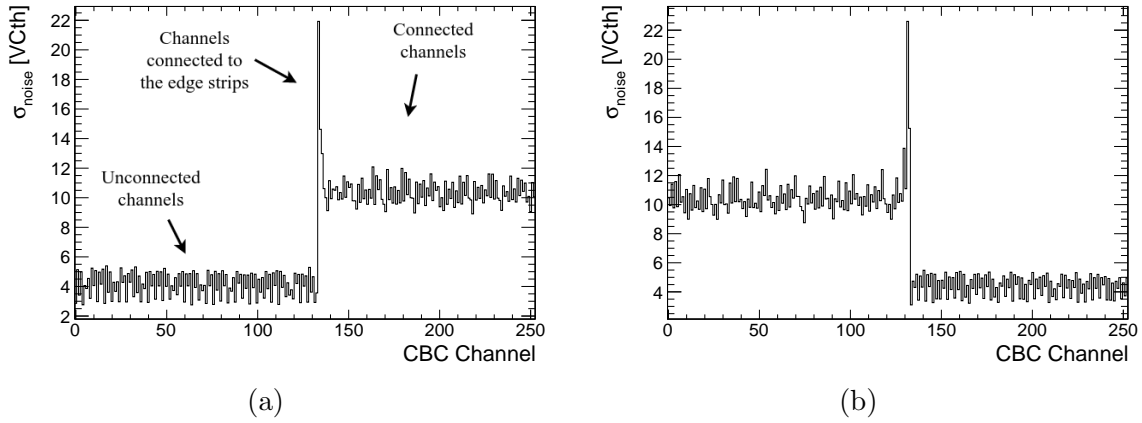


Figure 5.3.: Noise in the channels of the two CBC chips (a, b) used in the measurements. Odd channels represent the strips of the top sensor, while even channels correspond to the bottom sensor.

The hit detection threshold used in operation is typically configured approximately  $4 \cdot \sigma_{\text{noise}}$  above the pedestal in order to suppress noise hits. Around 70 electron-hole pairs are created by a minimum ionising particle per micrometre of Silicon [19], resulting in approximately

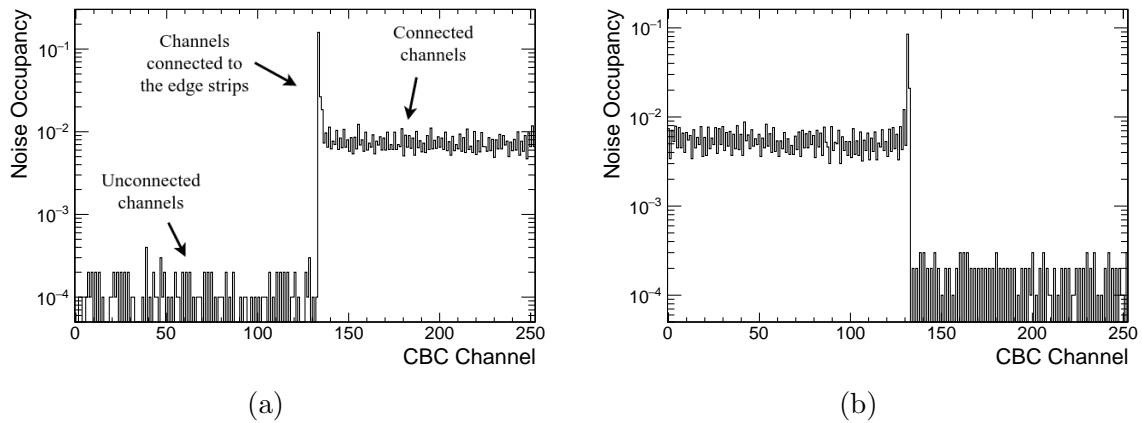


Figure 5.4.: Noise occupancy in the channels of two CBC chips (a, b) used in the measurements. Odd channels represent the strips of the top sensor, while even channels correspond to the bottom sensor.

14 000 pairs for the present 200  $\mu\text{m}$  thick sensors. Therefore, operating at a threshold of  $4 \cdot \sigma_{noise} \approx 16\,800$  electrons above the pedestal would significantly reduce efficiency for the present module. An operation threshold of 120 VCth units was chosen, being  $3 \cdot \sigma_{noise}$  above the pedestal. The resulting noise occupancy was measured for this threshold in the test beam area and can be seen in Figure 5.4, with the average occupancy of approximately 0.65% present in the front-end channels.

The unconnected channels and some of the edge channels were disabled before the data collection. The edge channels showed higher noise due to non-uniform electric field at the edges of the sensor active area. To eliminate such an effect, guard rings are typically used in semiconductor sensors. However, in the current setup the guard rings were left unconnected, resulting in a different capacitance of the edge sensor channels compared to the inner ones.

### 5.1.3. Results

**Noise performance in a particle beam** In Figure 5.5, fractions of events with different number of hits in one sensor are compared for two thresholds. The range of the histogram corresponds to the amount of enabled channels in the sensor. The measurement was performed without reconstructing telescope tracks, which results in the possibility to have events not containing any hits. As the threshold of 160 VCth units is below the tuned pedestal level, the distribution shows a significant fraction of channels firing for most events due to noise hits, whereas the measurement for a threshold of 120 VCth units shows, as expected, significantly lower noise hit fractions.

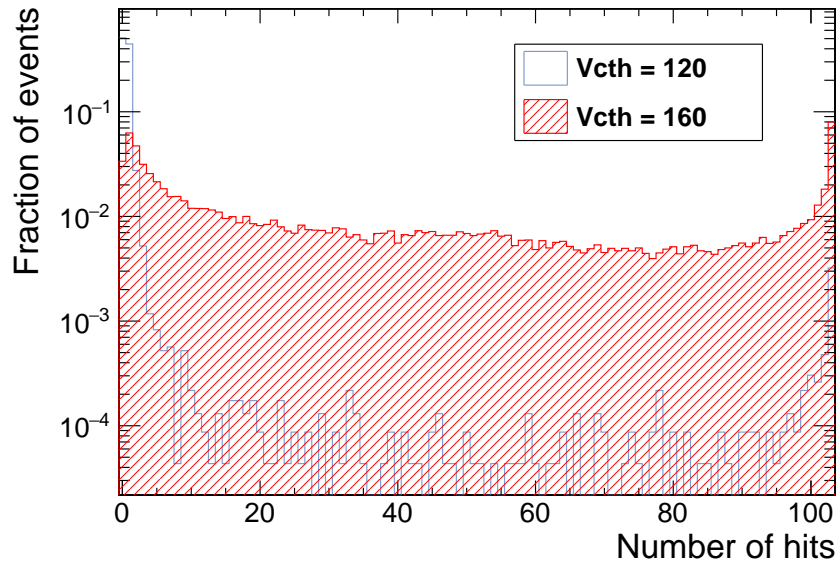


Figure 5.5.: Fraction of events with different amount of hits in one sensor for two threshold values.

For both thresholds an increased number of events, where all channels are firing, can be seen in the plots. This is caused by common mode noise, which is represented by a common shift of the pedestal for all channels in a given event, resulting in all channels passing the threshold. This typically happens when a module does not have filtering on the high-voltage line, which results in the pick-up of electromagnetic noise from the environment. In order to reduce the noise effect on the measurement results, events containing clusters with more than 16 hits were discarded during the analysis, whereas for future modules a high-voltage filtering circuit will be placed close to the sensors in order to resolve the existing problem.

**Track reconstruction** The overview on the alignment and track reconstruction procedures is given in Section 4.4. The alignment procedure of the EUTelescope framework does not allow to constrain the relative positions of tracking planes, while the 2S mini-module consists of two sensors with a fixed relative position. In order to overcome this challenge, a virtual sensor plane between the two physical sensors was introduced for the analysis. The cluster position on the virtual plane is calculated as the average cluster position between the two sensors

$$x_{DUT} = \frac{x_{top} + x_{bottom}}{2}. \quad (5.1)$$

Virtual clusters were created for all possible cluster combinations of the two sensors. The alignment procedure was then performed using the virtual plane and the alignment constants were applied to the physical sensors. The main drawback of this method is that it assumes a perfect alignment between the two sensors. Therefore, a correction on the relative sensor shift was applied based on assembly studies which will be presented further, whereas possible strip non-collinearity between the two sensors was not taken into account.

The final track reconstruction procedure was then performed using the hits from the telescope, the virtual sensor and the reference plane, see details in Section 4.4. The track reconstruction processor in the EUTelescope framework produces track hits defined as points at which reconstructed tracks cross sensor planes. The track hit positions on the physical DUT sensors were defined as the intersection points of the straight lines connecting the track hits on the closest telescope planes and the track hit on the virtual sensor with the DUT sensor planes. The resolution of the latter is calculated based on the resulting residual distribution

$$\sigma_{DUT} = \sqrt{\sigma_{meas}^2 - \sigma_t^2}, \quad (5.2)$$

where  $\sigma_t$  is the track pointing resolution of the telescope and  $\sigma_{meas}$  is the measured width of the residual distribution. The telescope track pointing resolution is calculated using the GBL Track Resolution Calculator [109] and results in a value of  $\sigma_t = 4.09 \mu\text{m}$  for both sensors. At a close to normal beam incidence angle a residual width of  $\sigma_{meas} = (26.09 \pm 0.06) \mu\text{m}$  was measured for the top sensor and corresponds to a detector resolution of  $\sigma_{DUT} = 25.77 \mu\text{m}$ . Charge sharing between neighbouring strips is minimal at small beam incidence angles, and therefore the expected resolution can be estimated from a simple geometrical calculation, resulting in  $\sigma = \frac{p}{\sqrt{12}} = 25.98 \mu\text{m}$  ( $p$  represents the sensor pitch), which matches the measured value.

**Cluster size** The cluster size distribution was measured in order to align the rotation stage. The module was tilted with respect to the beam axis in order to measure the mean cluster size at different particle incident angles, see Figure 5.6. The cluster size is the projection of a charge cloud on the strip surface, therefore for ideal point-like strips, the cluster size is defined by the geometrical relation

$$s(\theta) = s_0 + \frac{d_0}{p} \cdot |\tan(\theta - \theta_0)|, \quad (5.3)$$

where  $s_0$  is the cluster size at zero incident angle,  $d_0$  is the sensor thickness,  $p$  is the sensor pitch. Here,  $\theta_0$  is an angular offset between the setting of the rotation stage and the real beam incidence angle.

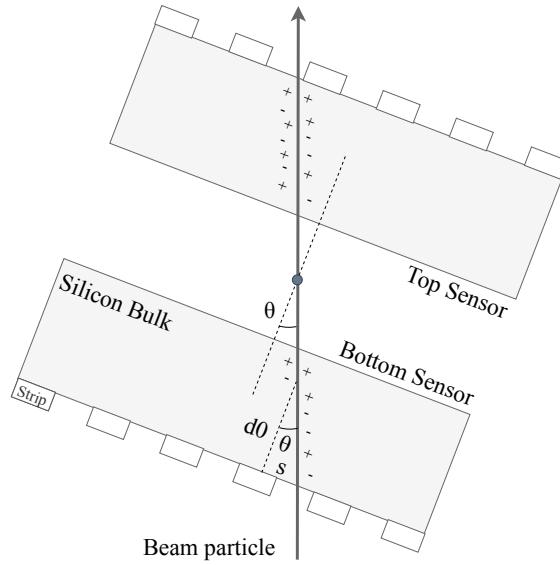


Figure 5.6.: Particle traversing the module at a non-zero incident angle.

For non-ideal sensors, the charge sharing between neighbouring strips depends on the sensor geometry, implant structure and electric field distribution. In addition, the discriminator threshold affects the distribution, reducing the cluster size. Therefore, the  $\frac{d_0}{p}$  relation in Equation 5.3 is replaced with a parameter  $\alpha$ , which accounts for all the above effects. The convolution with a normal distribution was performed in order to take into account charge diffusion in the Silicon bulk and other uncertainties. The final parametrisation is similar to the one in [110]

$$s(\theta) = \frac{1}{\sqrt{2\pi\sigma^2}} \cdot \int_{-\infty}^{\infty} [s_0 + \alpha |\tan(t - \theta_0)|] \cdot e^{-\frac{(t-\theta)^2}{2\sigma^2}} dt. \quad (5.4)$$

The corresponding cluster size distribution is shown in Figure 5.7 and includes only clusters matched with particles tracks. An average angular offset of the rotation stage of  $(1.07 \pm 0.18)^\circ$  was extracted from the fit. An uncertainty of around 17% is caused by the fact that the angular scan does not contain a sufficient amount of points to constrain the

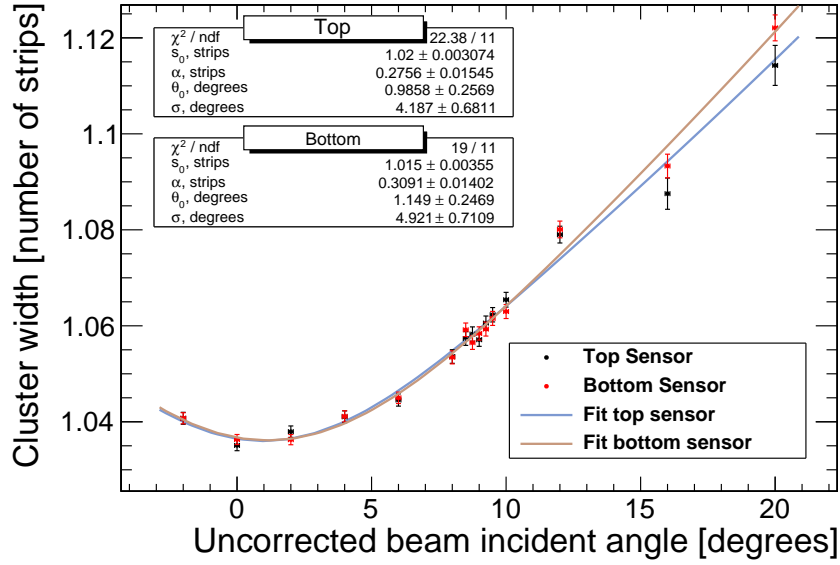


Figure 5.7.: Mean cluster width for different beam incident angles.

angular offset. The corrected beam incident angles obtained by subtraction of the measured angular offset were used in the following analysis.

The cluster width distribution for two different threshold values at the corrected  $1.07^\circ$  incident angle is shown in Figure 5.8. At angles close to normal incidence, most of the clusters are expected to have a size of one or two strips for such a strip pitch. Clusters with

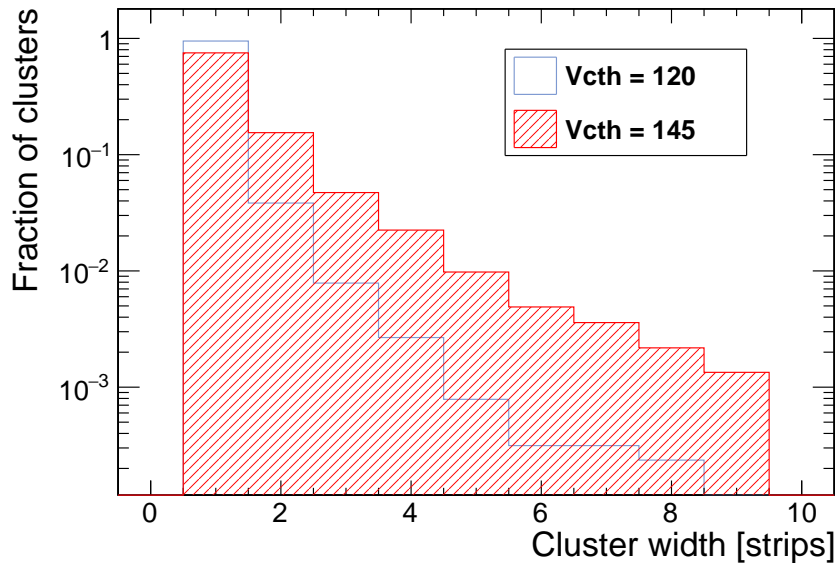


Figure 5.8.: Fraction of clusters with different size for two different threshold values. A lower digital VCth value corresponds to a higher threshold.



sizes of three strips and more are caused by high energetic secondary electrons, or delta-electrons, which can be generated inside the Silicon bulk and affect approximately 1 % of clusters. Such wide clusters can also be a result of the capacitive coupling between the strips leading to increased fractions of large clusters, as can be seen for the tested prototype for both thresholds in Figure 5.8.

**Assembly quality** In order to examine the module assembly quality, the distance between the corresponding clusters in the two sensors was calculated for each event. The mean values obtained by fitting the resulting distribution for each incident angle are presented in Figure 5.9. As in [72], the following equation was used as a fit function

$$\Delta_{clusters} = \Delta_0 + \frac{\delta}{p} \cdot \tan(\theta), \quad (5.5)$$

where  $\Delta_0$  defines the offset in strips between the two sensors along the sensitive axis,  $\delta$  is the spacing between sensors and  $p$  is the sensor pitch. A spacing of  $(4.01 \pm 0.02)$  mm is found between the sensors by the fit, which matches the design value of 4 mm. The offset between the two sensors is measured to be  $(0.38 \pm 0.04)$  strips or  $(33.82 \pm 3.19)$   $\mu\text{m}$ , and is a reasonable sensor misalignment after assembly.

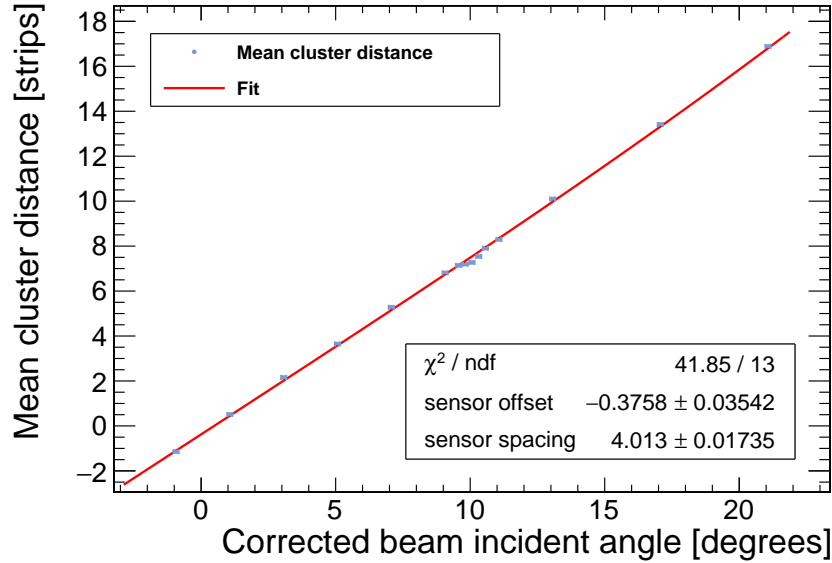


Figure 5.9.: Mean cluster distance between two sensors versus beam incident angle.

**Transverse momentum discrimination** The measurements performed at different module tilt angles with respect to the incident beam were used to verify the transverse momentum discrimination functionality. If a particle traverses a  $p_T$  module at zero incident angle without an external field applied, it hits both sensors of the module at the same place (neglecting missalignment between the sensors). If the module is tilted, a beam particle will traverse the

module at a non-zero angle, resulting in a stub creation, similar to the case with magnetic field in the CMS experiment also resulting in a non-zero incidence of particles.

As explained earlier in Section 3.1, the CBC2 chips are only able to mark the events containing stubs, in contrary to the final chip version which transfers address and bend information. Therefore, the efficiency of the stub generation was calculated based on the cluster data. The stub bending was defined as the distance between clusters in the top and bottom sensors, with a maximum allowed distance of 20 strips. The stub efficiency was defined as the ratio between events containing stub indication generated in the front-end chip and the total amount of stubs reconstructed during analysis. This calculation was performed for each beam incident angle and results in a stub efficiency turn-on curve, which is shown in Figure 5.10. Beam incident angles are corrected using the angular offset measured by the cluster width distribution, see Figure 5.7. The stub efficiency plot shows full efficiency at lower incident angles, meaning that all stubs reconstructed in software were matched with the stub presence indication from the CBC2 chips. The stub indication is not supposed to be generated anymore after a certain turn-off angle, which can be configured by setting a maximum allowed stub bending on the chip. A complementary error function

$$s_{eff}(\theta) = a_0 + a_1 \cdot \operatorname{erfc}\left(\frac{\theta - a_2}{a_3 \cdot \sqrt{2}}\right) \quad (5.6)$$

is used to fit the distribution. The resulting efficiency of  $(99.8 \pm 0.1) \%$  was measured at small beam incident angles. The CBC2 chips were configured to provide a stub discrimination window of  $\pm 7.5$  strips. This means, that a stub is generated only when the hit in the top sensor lies within a distance of seven strips from the hit in the bottom sensor. The reference strip is not taken into account, which extends the window by 0.5 strips in either direction.

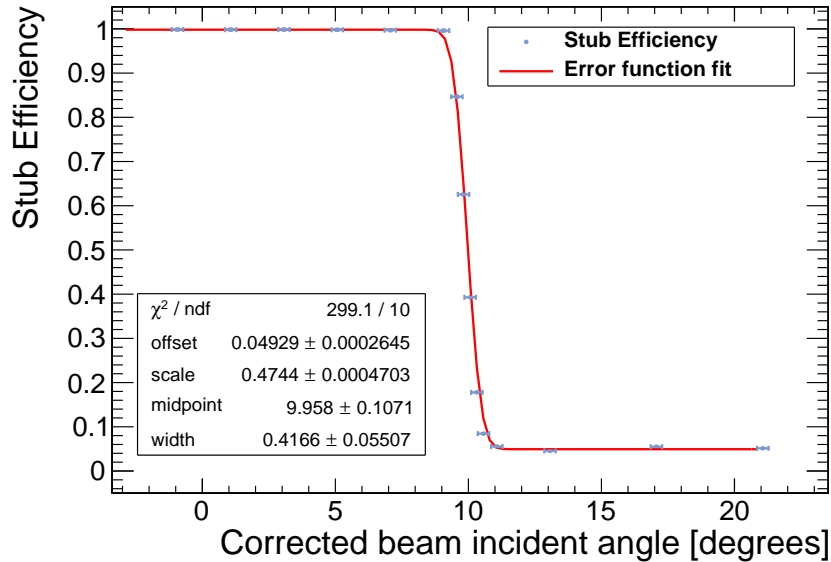


Figure 5.10.: Stub efficiency versus beam incident angle curve. The fit was performed using the complementary error function.

The transition point, or midpoint, of the curve was measured to be  $(9.96 \pm 0.42)^\circ$  and defines the average angle at which clusters on the two sensors do not form a stub anymore. The transition angle is converted into the distance between two clusters using the fit function from the mean cluster distance distribution (Figure 5.9), which also accounts for the sensor offset. A discrimination window of  $(7.45 \pm 0.11)$  strips was obtained and matches the configured window size within the measurement error.

In order to obtain a relation between the particle momentum and its incident angle in the magnetic field, a sequence of assumptions has to be made. The following calculations are performed assuming that a particle originates from a pre-defined point in space and the  $p_T$  module is oriented towards this point. In the real case, additional corrections have to be applied for each module in order to account for the fact that modules are tilted with respect to the assumed origin. The detailed calculations considering all the mentioned here are provided in [61].

As the magnetic field in the CMS detector is oriented along the z-axis, particles have helical trajectories rotating in the xy-plane. According to the Lorentz force equation, the particle trajectory bending radius in this plane is

$$r_T[\text{m}] \approx \frac{p_T[\text{GeV}/c]}{0.3 \cdot B[\text{T}]}, \quad (5.7)$$

where the charge of a particle is assumed to be  $\pm e$ . The relation between the particle incident angle  $\theta$  and the bending radius of the trajectory is given by the relation  $\sin(\theta) \approx \frac{R}{2 \cdot r_T}$ , where  $R$  is the radial position of the module. Thus, the Equation 5.7 is transformed into

$$p_T[\text{GeV}/c] \approx \frac{0.15 \cdot B[\text{T}] \cdot R[\text{m}]}{\sin(\theta)}. \quad (5.8)$$

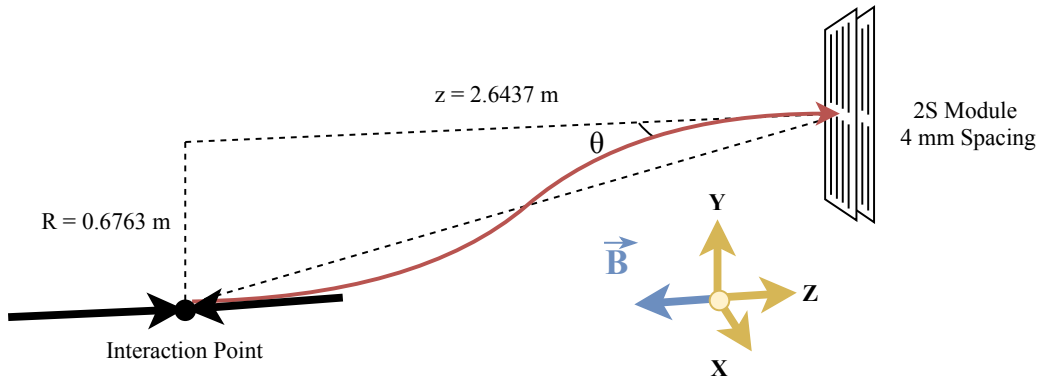


Figure 5.11.: Schematic representation of the particle moving in the magnetic field towards the 2S module placed in the end-cap disk.  $\theta$  represents the particle incident angle in the xz-plane.

The 2S modules with 4 mm spacing, corresponding to the geometry of the tested module, will be placed only on the end-cap disks of the outer tracker. One of these modules will be

placed on the end-cap disk at  $z = 2.6437$  m and a radial distance of  $R = 0.6763$  m, schematically shown in Figure 5.11. The earlier defined discrimination threshold of  $(9.96 \pm 0.42)^\circ$  would correspond to a transverse momentum cut of  $p_T \approx (2.23 \pm 0.09)$  GeV for positively charged particles. Due to the uncorrected offset between the sensors, a transverse momentum cut for negatively charged particles would be  $p_T \approx (2.46 \pm 0.11)$  GeV. Both values match the theoretically expected threshold of 2.3 GeV for the module with perfectly aligned sensors.

**Cluster efficiency** The cluster efficiency is defined as the ratio between the number of clusters matching particle tracks and the total number of tracks traversing the sensor. In order to match a track, the residual of a cluster has to be less than  $90 \mu\text{m}$ , which corresponds to the sensor pitch. The efficiency was averaged over the inner part of the sensors, excluding the edge strips. The cluster efficiency for different threshold values is shown in Figure 5.12. As for higher threshold values the probability to pass the discriminator is lower, the efficiency drops for lower values of VCth. The region of lower thresholds has close to the maximum efficiency, as the thresholds are sufficiently low to detect all particles passing through the detector. However, a slight drop of efficiency can be observed for lowest thresholds due to common mode noise, which was already discussed earlier, see Figure 5.5 and the corresponding explanations. The high number of noise hits leads to a shift of the reconstructed cluster centre positions, and causes the drop in cluster efficiency.

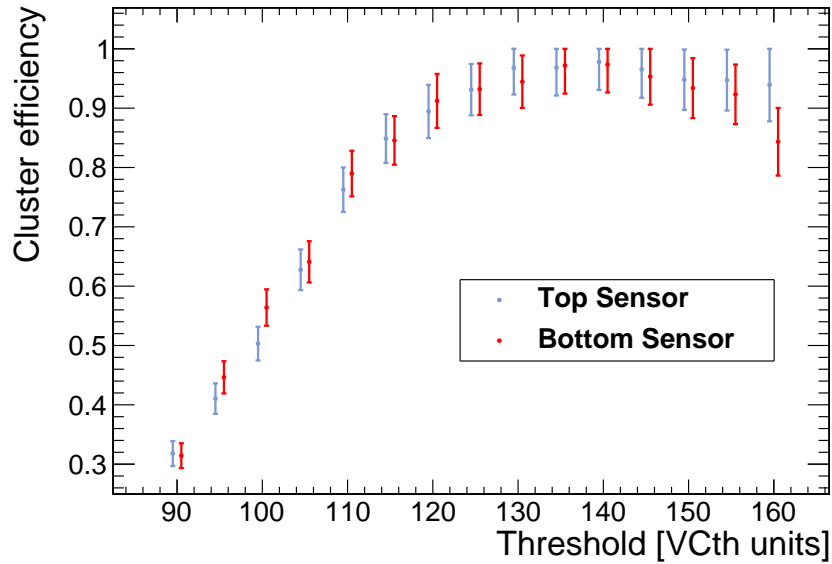


Figure 5.12.: Cluster efficiency for different VCth values for the two sensors. A higher VCth value corresponds to a lower threshold. An offset between the data points for the top and bottom sensors was introduced for better visibility.

The module is reaching efficiencies of only around 95 %, which is caused by a relatively small signal sampling window of 25 ns, see Figure 5.13a. During the data taking, a single

sampling interval (S1) is used for the read-out. Depending on the arrival time of a particle, the integrated charge may not be sufficient to pass the discriminator threshold. This happens if a particle arrives at the end of the integration window (red curve). In order to study this behaviour, the efficiency for different particle arrival phases was measured using the  $\mu$ DTC and is shown in Figure 5.13b. A drop of efficiency of up to 20 % is visible for the phases close to the end of the sampling window, which results in a smaller average efficiency. In order to reach a maximum average efficiency, the phase of the sampling clock has to be adjusted. This functionality is provided by the outer tracker modules, requiring an additional timing calibration during the installation of the system in the CMS experiment.

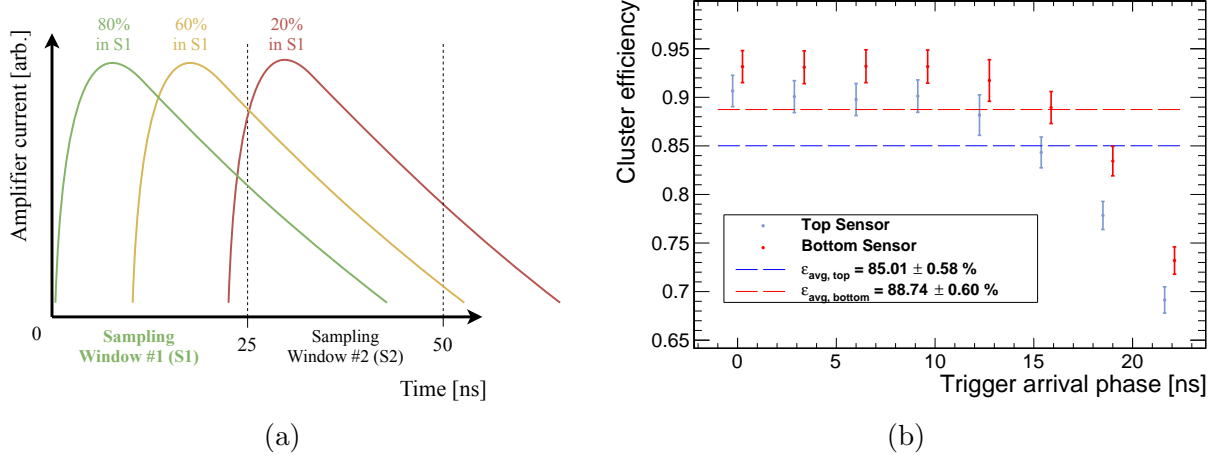


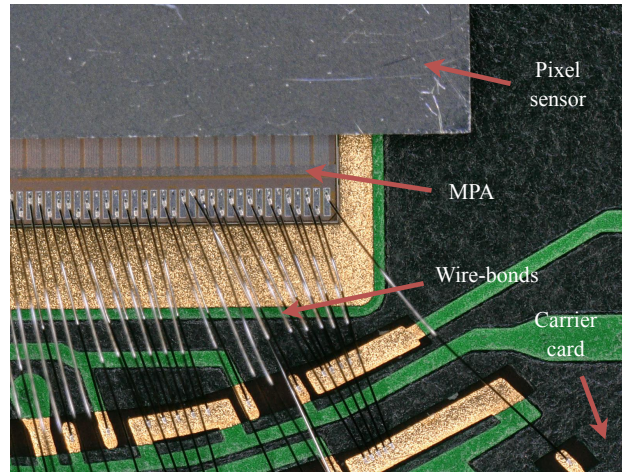
Figure 5.13.: Schematic illustration of the signal sampling (a) and the resulting cluster efficiency for different trigger arrival phases for the two sensors (b). The discriminator threshold is 120 VCth units. An offset between the data points for the top and bottom sensors was introduced for better visibility.

#### 5.1.4. Summary

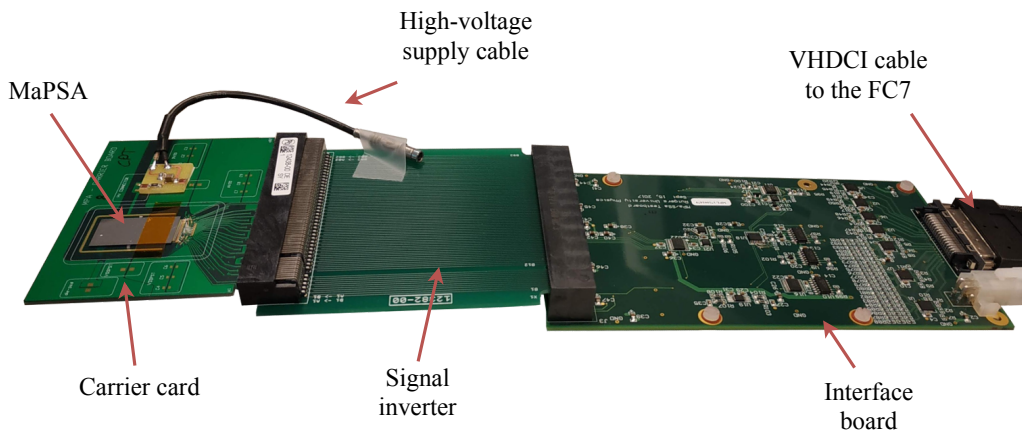
The  $\mu$ DTC board was used for the first time in a test beam. It has successfully proven the ability to acquire data and control the 2S mini-module, which was also successfully evaluated using a particle beam. The module shows a noise of 4200 electrons, which is significantly larger than expected and caused by common mode present in the data samples for all thresholds due to a high level of electromagnetic noise in the test beam environment and insufficient filtering on the high-voltage supply line. The filtering circuit has to be placed as close as possible to the sensors, which was not possible to implement for the current assembly. A relative offset of  $(33.82 \pm 3.19) \mu\text{m}$  was measured between the sensors in the direction of the sensitive axis. The transverse momentum discrimination functionality was verified by measuring a stub efficiency of  $(99.8 \pm 0.1) \%$  and a discrimination window of  $(7.45 \pm 0.11)$  strips, which matched the configured window size of 7.5 strips within the measurement error. The cluster efficiency was studied, showing a significant influence of both electromagnetic noise and particle arrival time on the efficiency for the present setup.

## 5.2. MaPSA Test Beam

The first samples of the MPA and SSA chips arrived at CERN in the beginning of 2018. Extensive testing was performed using the  $\mu$ DTC as the DAQ and Control system. The first test beam validation of the MPA chip was performed at CERN in April 2018. A set of Macro-Pixel Sub Assemblies (MaPSAs) was built at Karlsruhe Institute of Technology (KIT) and tested in a particle beam. In contrast to the final PS module, the tested MaPSAs consisted of only one reduced-size macro-pixel sensor connected to a single MPA chip. The functionality of the chip in a beam environment was confirmed using these assemblies. Sensor layout tests were performed during the subsequent beam measurement campaign in May 2018 at DESY, with the results being presented in this section. The results obtained from a set of angular, bias voltage and threshold scans are presented further, with an approximate number of  $10^6$  events per data point.



(a) Microscope picture of MaPSA wire-bonded to the carrier card.



(b) Carrier card connected to the interface board.

Figure 5.14.: Photographs of the setup.



### 5.2.1. Module and Test Setup Description

The tested prototype consists of the MPA chip connected to the macro-pixel sensor using dedicated solder-balls (bump-bonds), all together named Macro-Pixel Sub Assembly (MaPSA) and mounted on a chip carrier card, see microscope picture in Figure 5.14a. A n-on-p planar sensor with a thickness of  $200\text{ }\mu\text{m}$  and a pitch of  $100\text{ }\mu\text{m} \times 1467\text{ }\mu\text{m}$  was used. The MPA chip is connected to the carrier card using wire-bonds. In Figure 5.14b the prototype connected to the interface board through the signal inverter is shown, with the latter being used to compensate mirroring of the connector on the carrier card. During the beam measurements, the setup was mounted on a rotation stage in order to perform angular scans with the rotation axis being parallel to the long edge of the pixels.

### 5.2.2. Calibration

The calibration of the MPA chip is performed in two steps. At first, an internal chip bias voltage supply is calibrated in order to generate the threshold, calibration pulse and other internal voltages according to the chip specifications [111]. The equalisation of the individual channel response is performed thereafter by extracting hit occupancies at each point of the threshold scan. The calibration pulse is used to imitate a relativistic charged particle passing through the sensor. The offsets of the front-end channels are shifted in order to reach an equal response to the calibration pulse.

The threshold scan for one pixel is shown in Figure 5.15a. In comparison to the CBC chip, the MPA has a direct relation of VCth to the analog discriminator threshold - a larger digital value (VCth unit) corresponds to a larger threshold. The MPA chip has a differential front-end, which results in no signal below the baseline, as compared to the CBC chip. The baseline can be seen as a peak located close to a threshold of 62 VCth units. The second component of the curve is the signal from the calibration pulse. The measurement

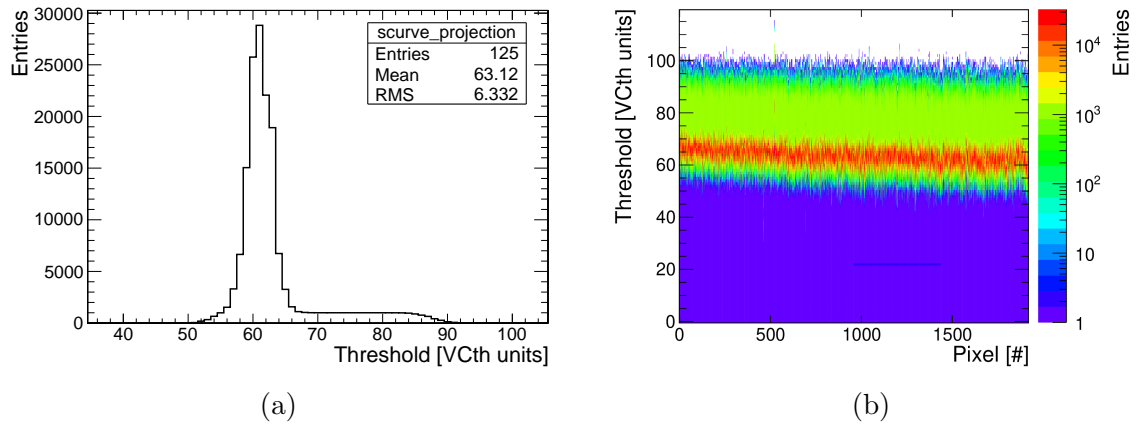


Figure 5.15.: Threshold scan for one pixel (a) and the combined plot for all pixels (b).

was performed by sending 1000 calibration pulses, and one can see the signal ending at a threshold of approximately 88 VCth units, which denotes the amplitude of the calibration pulse in threshold units. The signal transition point is smeared due to variations of the injected charge. The threshold scan combined for all pixels is presented in Figure 5.15b and shows that the equalisation procedure succeeded and the calibration pulse response is well-aligned for all channels. A slope can be seen for the pixel baseline position across the chip, which is caused by the fact that power is connected to one side of the chip, resulting in a voltage drop.

The noise is extracted from the threshold scan by fitting the baseline peak using a normalised Gaussian distribution. The distribution of the noise for all channels is shown in Figure 5.16. The average standard deviation of 1.95 VCth units corresponds to a charge of around 180 electrons and matches the expected value.

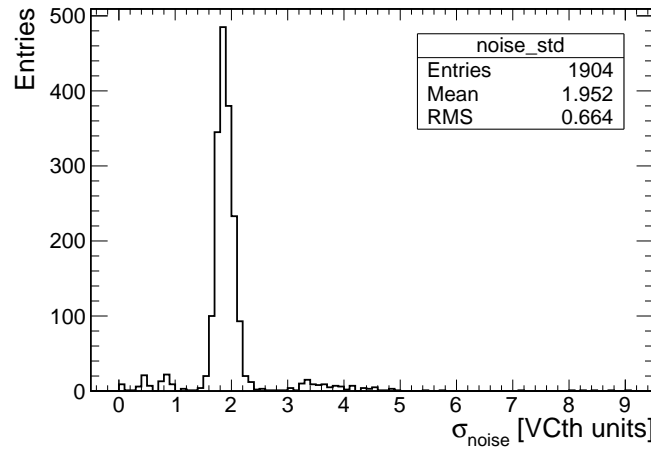


Figure 5.16.: Distribution of the electronic noise for all channels.

### 5.2.3. Results

**Timing performance** As already seen for the 2S mini-module, the timing performance of the detector becomes crucial for a sampling period of 25 ns and has to be verified. In the CMS experiment, the trigger signal arrives several microseconds after a physical event. Data are buffered in the front-end chips, and a so-called latency scan has to be performed in order to define which address in the buffer corresponds to the triggered physical event. Several thousands of events are collected for each address setting, statistically representing the shape of the signal at the output of the comparator. In order to reconstruct the signal shape, the memory address (latency) is used as the coarse time measurement (25 ns steps) and the trigger arrival phase is used as the fine time measurement (3.125 ns steps). Reconstructed signal shapes for two different thresholds are shown in Figure 5.17a. In order to suppress the contribution from delta-electrons, clusters with a size of more than two pixels were discarded during analysis. At larger thresholds (e.g. VCth = 250), less particles are able to pass the



discriminator, which leads to the shortening of the signal width. On the other side, at lower voltages the signal becomes wider.

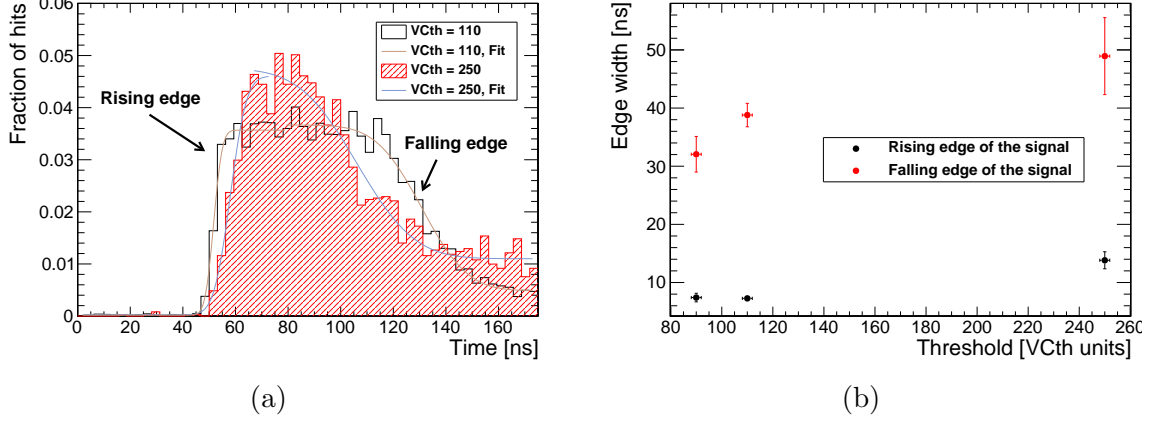


Figure 5.17.: Front-end signal shapes for two different thresholds (a) and widths of the rising and falling edges of the signal for several threshold values (b).

The signal shapes can be characterised using error functions. This allows to extract the average width of the rising and falling edges of the signals defined as  $\sigma$  in  $\text{erf} \frac{t-a}{\sigma\sqrt{2}}$ , where  $t$  is the time,  $a$  is the position of the edge. The dependence of the signal timing on the threshold is shown in Figure 5.17b. As mostly charge from highly ionising particles is sufficient to pass the discrimination stage at larger thresholds, the falling edge of the signal becomes longer. This can be explained by the fact that in order to minimise the charge variation influence on the timing performance, the analog stage of the chip was designed to have a constant peaking time. When the deposited charge is larger, it takes more time for the analog electronics to return to the zero current state, which leads to a longer falling edge of the signal. The rising edge shows only a slight increase of its width, which corresponds to the expected behaviour of the analog circuit.

**Digital path verification** The collected data also allow to characterise the digital performance of the chip. In the present assembly, the strip data input from the SSA chip is missing, thus the stub generation is not possible. However, in the MPA chip pixel cluster data can be forwarded to the stub data path directly. This gives the possibility to correlate the output of the stub and triggered data and to proof that both read-out interfaces are functional. In Figure 5.18, correlation plots between the cluster addresses transferred through the triggered and stub data paths are shown. The stub logic has been set to discard clusters larger than three pixels, therefore the corresponding cut on the triggered cluster size was applied in the analysis. The plots show a perfect correlation between the hit and stub data paths, thus allowing to conclude that both of them are functional.

In the current version of the chip a memory unit behaves unstable at the nominal supply voltage, and the third column was excluded from the analysis, as can be seen in Figure 5.18b.

An increase of the digital supply voltage solves the problem, but in order to confirm the memory issue the voltage was not raised during the accumulation of this data set.

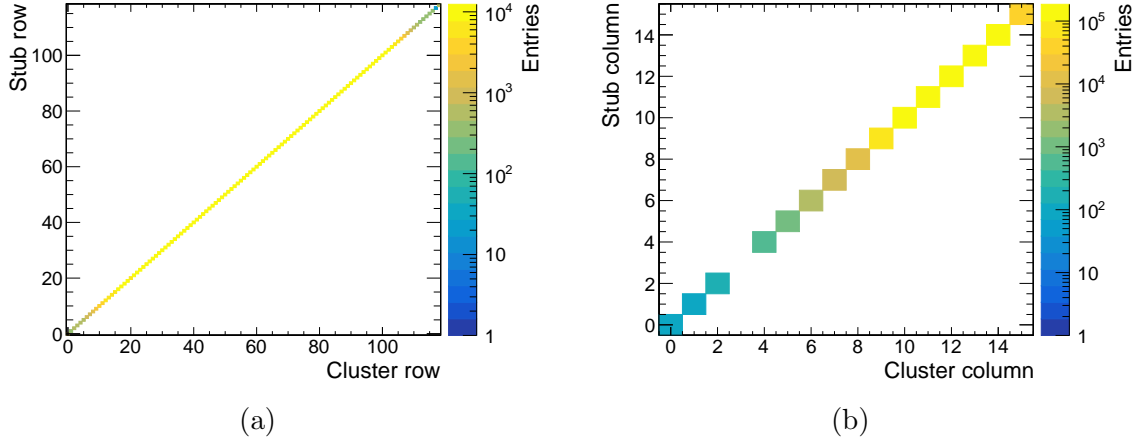


Figure 5.18.: Correlation plots between the cluster row (a) and column (b) addresses transferred through the triggered and stub data paths.

**Cluster size** In order to calibrate the rotation stage, an angular scan was performed. The mean cluster width distribution for different beam incident angles is shown in Figure 5.19. The rotation axis is parallel to the long edge of the pixel. Same as for the CBC2 analysis, the equation

$$s(\theta) = \frac{1}{\sqrt{2\pi\sigma^2}} \cdot \int_{-\infty}^{\infty} [s_0 + \alpha |\tan(t - \theta_0)|] \cdot e^{-\frac{(t-\theta)^2}{2\sigma^2}} dt. \quad (5.9)$$

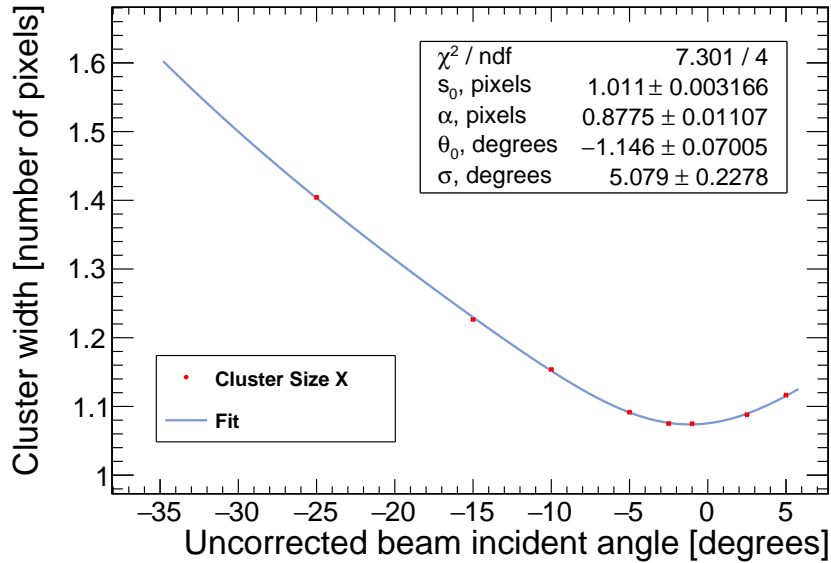


Figure 5.19.: Mean cluster width for different beam incident angles.

is used to fit the cluster width distribution. An angular offset of  $(-1.15 \pm 0.07)^\circ$  was extracted and the corresponding correction was applied to further calculations.

**Cluster efficiency** The prototype performance can be verified by calculating cluster efficiency, which is defined as the ratio of clusters matched with telescope tracks to the total amount of tracks passed through the sensor. In contrast to the setup comprised of strip sensors and described earlier, a two dimensional measurement is obtained from the pixel detector. Therefore, a matched cluster is defined as the cluster having a maximum distance of  $100\ \mu\text{m}$  and  $1467\ \mu\text{m}$  to the reconstructed track in the x- and y- directions, respectively. This distance is also referred to as cluster residual, with the selected acceptance window corresponding to the dimensions of the pixels.

The cluster efficiency averaged across the sensor and measured for different thresholds is shown in Figure 5.20. As expected, the efficiency drops towards larger threshold values. This happens as the clusters with lower deposited energy are discarded by the discriminator. A zoomed view shows that the efficiency reaches  $(98.26 \pm 0.06)\%$  at a threshold of 85 VCth units. Even though at this threshold the efficiency is higher, a value of 110 VCth units was chosen in the measurement campaign in order to suppress noise.

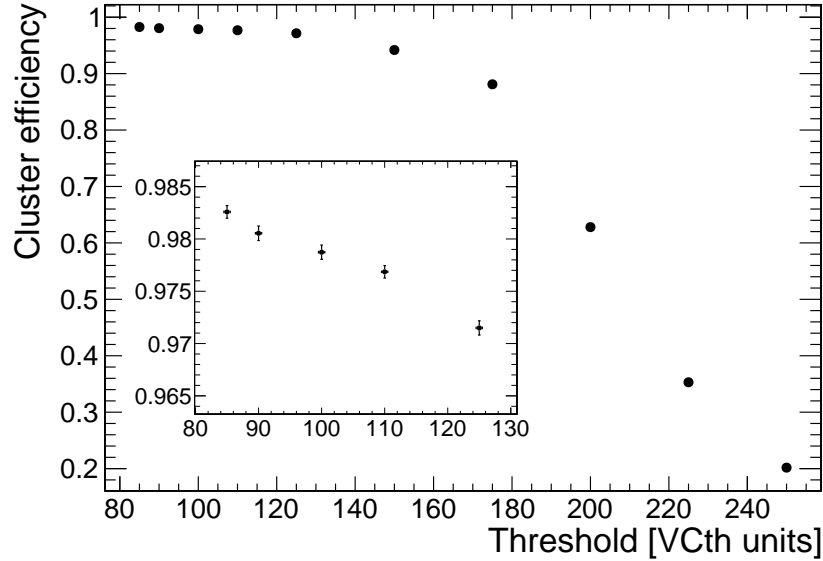


Figure 5.20.: Cluster efficiency for different thresholds. The bias voltage is  $V_{bias} = 200\text{ V}$ .

The cluster efficiency for different sensor bias voltages is shown in Figure 5.21. At lower voltages the sensor is not fully depleted, resulting in smaller charge being collected by the pixels. An efficiency value of  $(97.69 \pm 0.06)\%$  measured at  $V_{bias} = 200\text{ V}$  matches to the result obtained for a threshold of 110 VCth units during the threshold scan.

A cluster efficiency map measured with the sensor biased at  $V_{bias} = 20\text{ V}$  is shown in Figure 5.22a and is in agreement with the result obtained from the bias voltage scan discussed

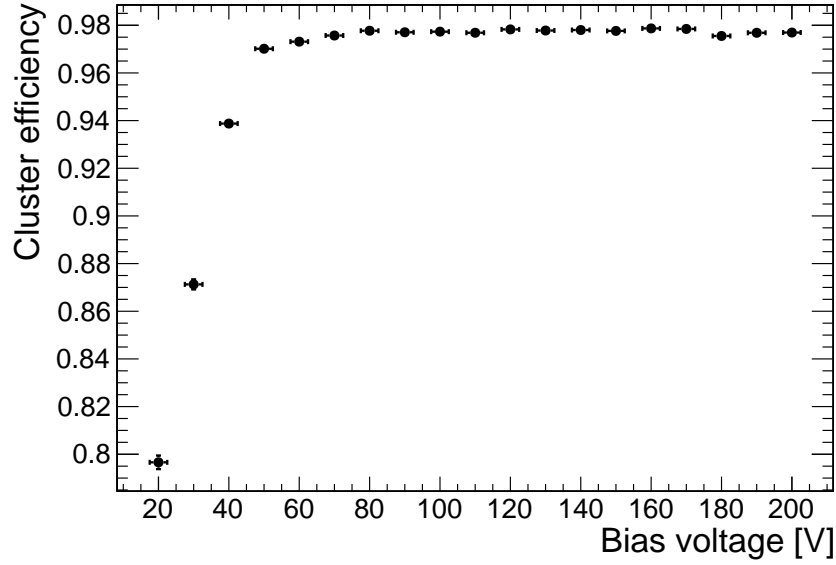


Figure 5.21.: Cluster efficiency for different bias voltages. The threshold is 110 VCth units.

above. At a voltage of  $V_{bias} = 200$  V, see Figure 5.22b, the pixels are fully efficient with a periodic inefficiency (horizontal lines) being present in the map and caused by the sensor bias voltage distribution scheme, which will be described further. Some of the pixels are disconnected in this module prototype which can be seen in both maps.

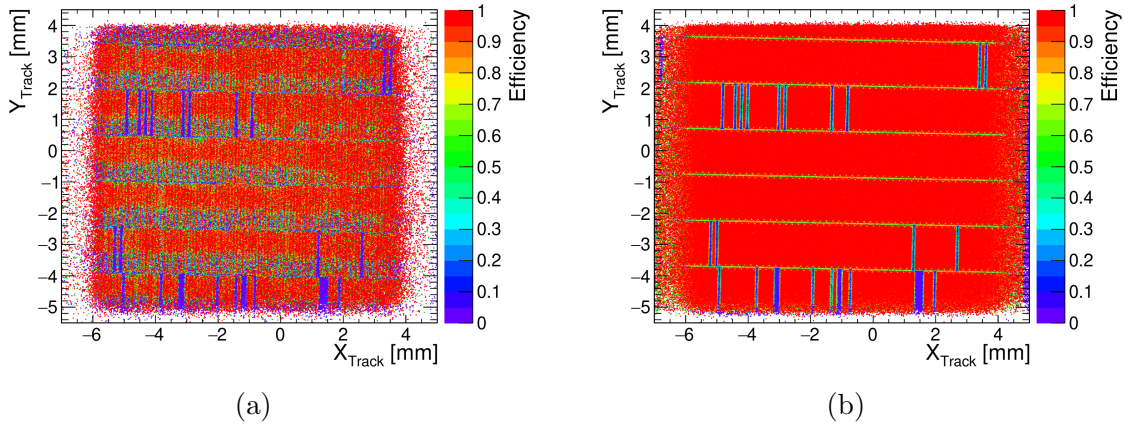


Figure 5.22.: Cluster efficiency maps for bias voltages of 20 V (a) and 200 V (b). The threshold is 110 VCth units.

**Sensor layout** The layout of the sensor is shown in Figure 5.23a, where four pixels are marked with thick red boundaries. The sensor is DC-coupled, meaning that each pixel is connected directly to the corresponding channel, which allows to bias the sensor through the front-end chip. For sensor testing purposes, a bias grid is integrated in the sensor allowing to bias it without a front-end ASIC. In this scheme, which was also used during

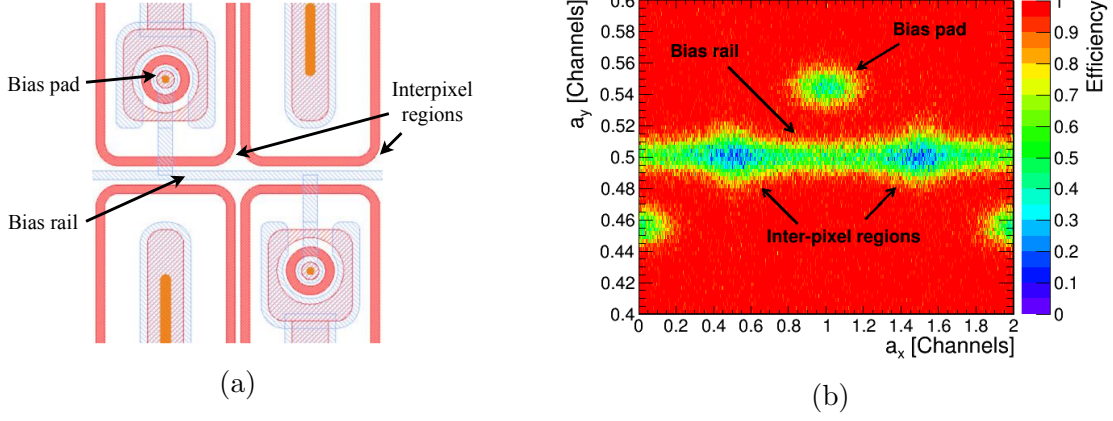


Figure 5.23.: Layout of the sensor (a) and the efficiency map for several neighbouring pixels measured at the bias voltage of  $V_{bias} = 200$  V and the threshold of 110 VCth units (b).

the measurements, the bias voltage is distributed across the sensor through bias rails. Each pixel has a bias pad, which exploits the punch-through technology, where voltage is being distributed to the read-out electrode through the Silicon bulk without a direct connection. In order to study the effect caused by the biasing scheme, a combined hit efficiency map was produced by converting the track positions with the equation

$$a_{x(y)} = t_{x(y)} \bmod (2 \cdot p_{x(y)}), \quad (5.10)$$

where  $t$  is the track position in global coordinates,  $p$  is the sensor pitch in the x- and y-directions. The resulting map is shown in Figure 5.23b and allows to combine the data from the complete sensor surface in the distribution for several neighbouring pixels. Three inefficiency regions can be seen in the map:

- The bias rails collect charge competing with pixels. Therefore, when a particle passes through the region of a bias rail, a drop in efficiency is observed.
- The bias pads, which have a chequerboard-like pattern on the sensor, cause the same effect as the bias rails.
- Reduced electric field is present in the inter-pixel regions, which causes a lower charge collection efficiency there. This region also overlaps with the bias rail inefficiency region.

In order to calculate the total inefficiency caused by the biasing scheme, the projections of the combined efficiency map were studied. The projection plots to the x- and y- axis are shown in Figures 5.24a and 5.24b, respectively. Both plots represent the averaged across the sensor drop of efficiency caused by the effects described above. All the efficiency drops can

be fitted using a normalised Gaussian distribution

$$\mathcal{N}(a_{x(y)}) = \frac{f}{\sqrt{2\pi}\sigma} \cdot e^{-\frac{(a_{x(y)}-a_0)^2}{2\sigma^2}}, \quad (5.11)$$

where  $\sigma$  characterises the width of the inefficiency region,  $a_0$  represents its centre and  $f$  represents the total inefficiency. The resulting efficiency drops that can be seen in Figure 5.24a are 0.3 % for both pads (one of them is split half in this projection) and 0.3 % for each of the inter-pixel regions. The efficiency drop estimated from the projection to the y-axis is 0.1 % for each bias pad and 1 % for the combined inter-pixel and bias rail regions, see Figure 5.24b. In order to get the cumulative effect from all the regions, all the inefficiency values have to be summed up, resulting in a value of 2.4 %. This calculation allows to conclude that the earlier measured efficiency of  $(97.69 \pm 0.06) \%$  at the threshold of 110 VCth units is lower than 100 % due to the sensor biasing scheme, with the effect decreasing at lower thresholds.

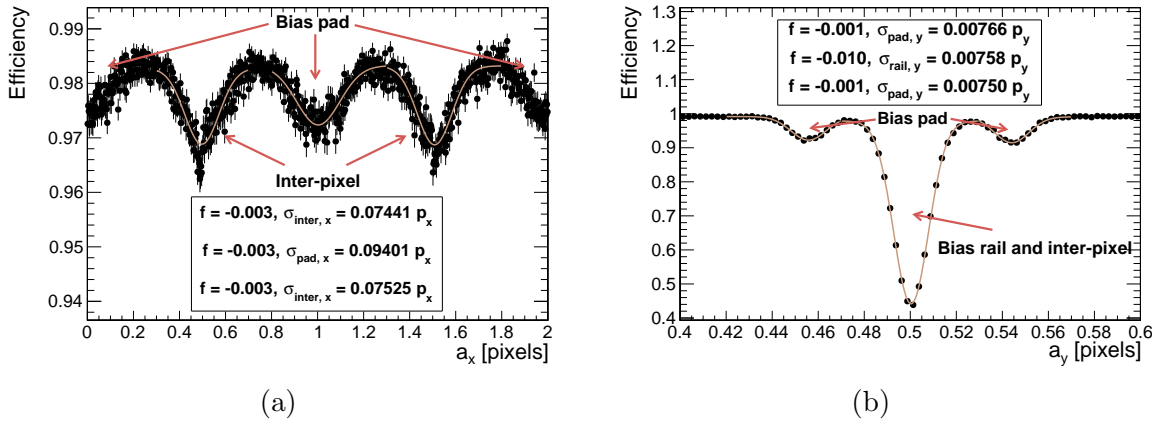


Figure 5.24.: Projections to the x-axis (a) and y-axis (b) of the efficiency map. The measurement was performed at the threshold of 110 VCth units and the sensor bias voltage of 200 V.

### 5.2.4. Summary

The timing performance of the MPA front-end was studied at three different thresholds, and the chip shows the expected for discriminators with a constant peaking time behaviour. The data from the stub and triggered digital paths were compared, showing the expected performance of both. The sensor efficiency was measured, and a value of  $(97.69 \pm 0.06) \%$  was obtained for the nominal threshold and bias voltage. The inefficiency caused by the biasing scheme of the sensor was calculated to be 2.4 %. A maximum efficiency of  $(98.26 \pm 0.06) \%$  was measured for low thresholds.

# Summary and Outlook

The high luminosity upgrade is an important step in the evolution of the LHC as it will provide the possibility to deliver higher interaction rates to its experiments. Due to the increase of radiation flux and degradation of the existing detector systems, the CMS detector will be upgraded. The new systems which will be installed in the CMS detector were described in the present manuscript with a focus on the upgrade of the CMS outer tracker. The concept of the  $p_T$  modules was introduced, with such modules being able to provide information about high transverse momentum tracks to the triggering system.

The back-end system responsible for the configuration, control, read-out and monitoring of the front-end modules during the prototyping and production stages was developed within the scope of this thesis. This system, also known as  $\mu$ DTC, is currently used for testing of the front-end ASIC prototypes and the front-end modules. So far, the  $\mu$ DTC has been used for the qualification of the prototype modules containing CBC, SSA, MPA and CIC chips in different hardware configurations, allowing to control the prototypes using electrical or optical interfaces. The resource utilisation was estimated for the existing firmware implementation indicating the possibility to control up to 8 front-end modules simultaneously. The resource utilisation was also projected towards the DTC, showing the importance of further optimisation.

Along with numerous laboratory tests, a sequence of beam test measurement campaigns was carried out at CERN, DESY and FNAL exploiting the developed read-out system. All of them have shown the stability of the  $\mu$ DTC during data taking, which qualifies it as a reliable experimental tool for the outer tracker prototype verification and future module production. The results of the beam test measurements performed at the DESY-II accelerator were presented in the manuscript.

The first ever test beam involving the  $\mu$ DTC was described in Section 5.1. The back-end system showed stable performance, whereas very high noise was seen in the channels of the 2S mini-module, caused by missing high voltage filtering. The corresponding improvements will be implemented during the assembly of future modules. The assembly studies show an offset of only  $(33.82 \pm 3.19) \mu\text{m}$  between the sensors. A stub efficiency of  $(99.8 \pm 0.1) \%$  and a discrimination window of  $(7.45 \pm 0.11)$  strips were measured for the module prototype, showing the expected performance of the transverse momentum discrimination logic for the configured window size of 7.5 strips. The cluster efficiency was studied, showing a dependence of the efficiency on the particle arrival time and electromagnetic noise.

The qualification of the MPA-based pixel assembly was described in Section 5.2. The timing performance was verified by reconstructing the shapes of the signals induced by charged particles passing through the sensor, whereas the performance of the digital stub data path was tested by forwarding the cluster data through it and further correlating them with the triggered cluster data. The influence of the biasing structure on the sensor efficiency was studied, showing an effect of approximately 2.4% at the threshold of 110 VCth units and resulting in efficiency of  $(97.69 \pm 0.06) \%$ . A maximum efficiency of  $(98.26 \pm 0.06) \%$  was measured for low thresholds. As an outcome of the measurement campaign, the MaPSA has shown good and well-predictable performance in a particle beam.

A further optimisation of the  $\mu$ DTC is foreseen by performing the resource optimisation of several firmware components with a focus on the ones that can be re-used in the future DTC system. Implementation of the multipurpose command processor block is ongoing and will allow to move a set of calibration and monitoring algorithms to the FPGA thus reducing the load on the communication channel between the FPGA and the user software. A set of new hardware prototypes, as well as the final modules, are expected to be delivered in the nearest future and will require additional verification infrastructure to be developed within the  $\mu$ DTC.



## A. TLU Interface

The Trigger Logic Unit (TLU) [96] was designed to distribute triggers among different detectors in a test beam environment. It is actively used with EUDET-type telescopes by high energy physics collaborations.

The TLU provides four scintillator channel inputs with configurable threshold. This allows to connect the TLU directly to the scintillating detectors and require coincidence between different channels. The coincidence of four scintillators is used to trigger a typical EUDET-type telescope. In order to distribute triggers to detector systems, six RJ-45 connectors are provided on the front panel of the device. Four additional channels are available to distribute triggers using coaxial connectors.

In order to distribute triggers using the RJ-45 connectors, a dedicated interface is defined. The RJ-45 connector and the corresponding Ethernet cable contain four differential pairs to transfer data. Depending on the operation mode, the TLU may exploit from one to three differential lines for triggering. The available modes are:

- **No handshake** - the trigger is distributed over a differential trigger line.
- **Simple handshake** - the trigger is distributed over a differential trigger line, a detector has to raise a busy signal in order to acknowledge the received trigger. The TLU is not able to send further triggers until the busy signal becomes low.
- **Data handshake** - same as simple handshake, but allows to receive an identification number of the current event. An additional clock line is used for the data transfer. The mode definition is shown in Figure A.1. Once the trigger signal is received, a detector has to raise the busy signal and start sending the clock signal with a frequency up to 10 MHz. When both busy and clock signals are identified by the TLU, the transmission of the trigger identification number starts. After the end of the transaction, the detector has to pull the busy signal low.

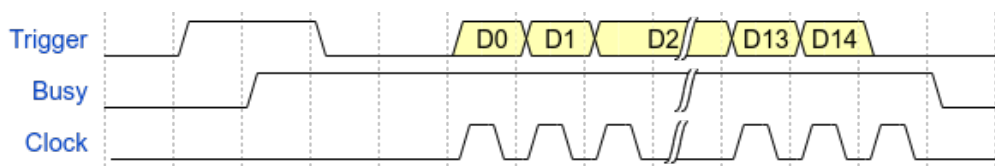


Figure A.1.: Data handshake mode of the TLU.

The data handshake mode is the most reliable one for test beam operations. It helps to make sure, that all detectors including a telescope, a device under test and additional timing detectors are operating synchronously. Moreover, trigger identification numbers received by each detector can later be used to recover the synchronisation if it was lost at some point during data taking.

The FC7 board does not have any RJ-45 connectors and most of the FMC cards available on the market do not provide direct access to differential lines. Therefore, a dedicated converter had be designed in order to establish an interface between the TLU and the  $\mu$ DTC. The converter is shown in Figure A.2.



Figure A.2.: TLU RJ-45 to LEMO Converter.

As mentioned before, the Ethernet cable contains four differential lines, and in the present application the lines are used as two outputs from the TLU (trigger and reset) and two inputs (busy and clock). The converter performs a translation between differential and single-ended signals accessible by coaxial connectors. The electrical schematics are shown in Figure A.3. The produced converter allows to use the DIO5 FMC to connect the TLU to any FPGA board containing FMC connectors. The converter was successfully tested in the laboratory and later used during the beam test campaigns at CERN and DESY.

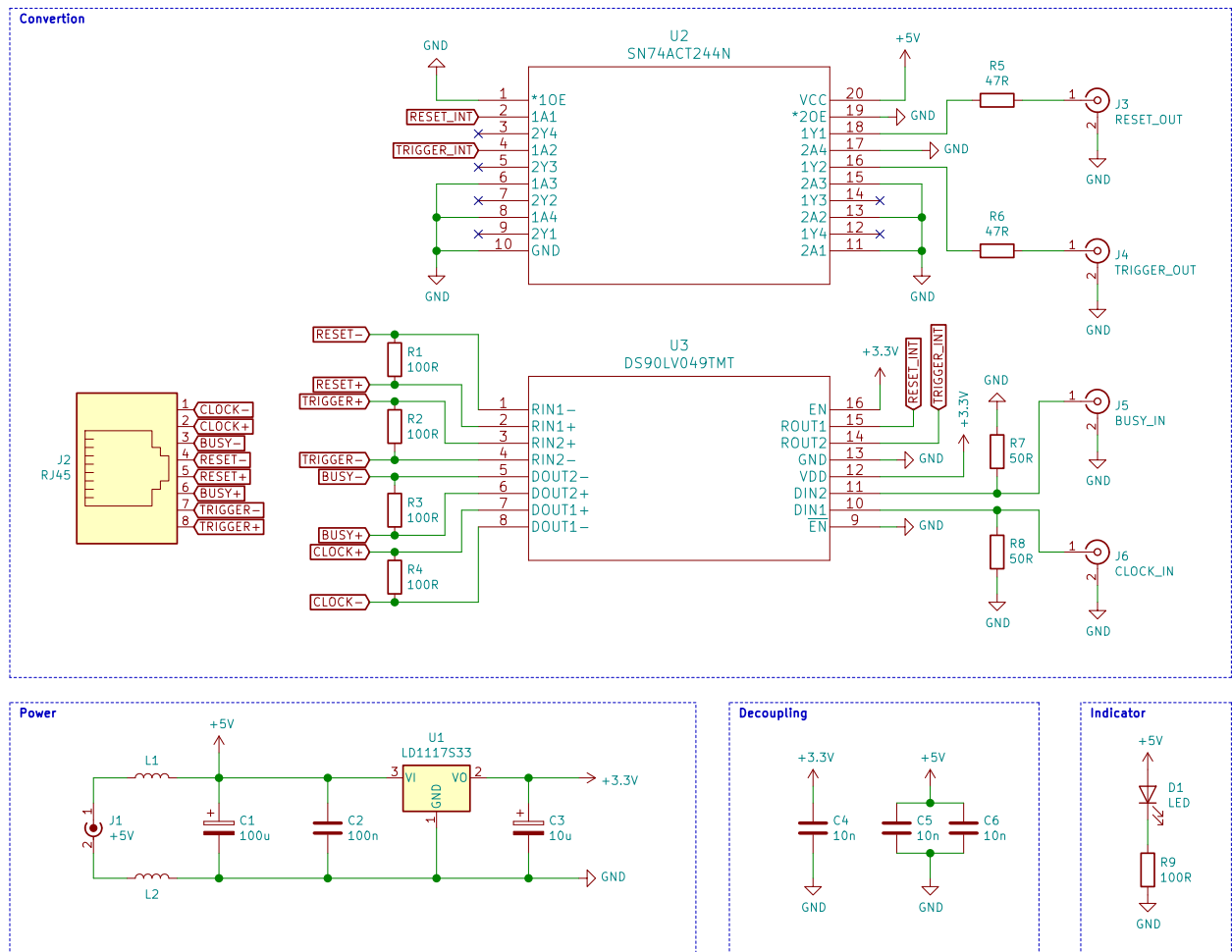


Figure A.3.: Electrical schematics of the RJ-45 to LEMO Converter.



# List of Acronyms

|           |   |
|-----------|---|
| $\mu$ DTC | Micro-DTC, DAQ system based on the FC7 board; pp. V, VII, 2, 32, 35, 37–39, 41–51, 53, 58, 59, 65, 66, 77, 78, 87, 88, 90     |
| $\mu$ TCA | Micro Telecommunications Computing Architecture; pp. 35, 39–41, 43  |
| 2S        | Two-Strip Module; pp. 28–31, 35–37, 47–49, 53, 65, 66, 70, 75, 77, 80   |
| ADC       | Analog-to-Digital Converter; pp. 61   |
| Al-CF     | Carbon Fibre Reinforced Aluminium; pp. 31   |
| ALICE     | A Large Ion Collider Experiment; pp. 7  |
| AMC       | Advanced Mezzanine Card; pp. 39   |
| ASIC      | Application Specific Integrated Circuit; pp. 10, 14, 35, 37, 38, 40–42, 45, 66, 67, 84, 87                                    |
| ATLAS     | A Toroidal LHC ApparatuS; pp. 4, 7, 24  |
| CBC       | CMS Binary Chip; pp. 29, 35, 36, 38, 45, 46, 53, 65–67, 74, 79, 82, 87  |
| CERN      | European Organisation for Nuclear Research; pp. 2, 6, 78, 90  |
| CFRP      | Carbon Fibre Reinforced Polymer; pp. 31   |
| CIC       | Concentrator Integrated Circuit; pp. 30, 36, 45, 49, 87   |
| CMOS      | Complementary Metal-Oxide-Semiconductor; pp. 14, 56   |
| CMS       | Compact Muon Solenoid; pp. V, VII, 1–4, 7–11, 15, 17, 19–21, 23–28, 31, 33, 35, 41–43, 46, 49, 50, 58, 65, 74, 75, 77, 80, 87 |
| CoG       | Centre-of-Gravity; pp. 60, 61   |
| CPU       | Central Processing Unit; pp. 10, 31, 44, 50   |
| CSC       | Cathode Strip Chambers; pp. 26  |
| DAQ       | Data Acquisition; pp. V, 10, 15, 28, 31, 38, 42, 44, 46, 49–51, 58, 65, 78  |
| DDR3      | Double-Data-Rate Three Synchronous Dynamic Random Access Memory; pp. 40, 46–48  |
| DESY      | Deutsches Elektronen-Synchrotron; pp. 2, 36, 53–57, 62, 65, 78, 90  |

|                  |  |
|------------------|--|
| DIO5             | 5-channel Digital I/O FMC module; pp. 43, 90                                     |
| DONUT            | Direct Observation of NU Tau; pp. 5  |
| DORIS            | Double-Ring Storage; pp. 53  |
| DTB              | Digital Test Board; pp. 58   |
| DTC              | DAQ, Trigger and Control Board; pp. 2, 31, 32, 35, 44, 46, 49, 50, 87, 88        |
| DUT              | Device Under Test; pp. 55, 57, 58, 61–63, 70                                     |
| ECAL             | Electromagnetic Calorimeter; pp. 9   |
| ERG              | Existence, Relatedness and Growth; pp. 1   |
| FC7              | FMC carrier board based on Xilinx Kintex 7 FPGA; pp. 35, 38–42, 46, 48, 49, 90   |
| FF               | Flip-Flop; pp. 40, 47–49   |
| FIFO             | First In First Out; pp. 47   |
| FMC              | FPGA Mezzanine Card; pp. 39, 41, 42, 44, 45, 90                                  |
| FNAL             | Fermi National Accelerator Laboratory; pp. 2                                     |
| FPGA             | Field Programmable Gate Array; pp. V, VII, 10, 31, 32, 35, 39, 40, 42–49, 88, 90 |
| GBL              | General Broken Lines; pp. 62, 63, 70   |
| GBT              | Giga-Bit Transceiver; pp. 45   |
| GBT-SCA          | GBT Slow Control Adapter; pp. 37   |
| GBTx             | Giga-Bit Transceiver Chip; pp. 36, 37, 45  |
| GEAR             | Geometry API for Reconstruction; pp. 61  |
| GEM              | Gas Electron Multiplier; pp. 26  |
| HCAL             | Hadron Calorimeter; pp. 9  |
| HERA             | Hadron-Electron Ring Accelerator; pp. 53   |
| HGCAL            | High Granularity Calorimeter; pp. 26   |
| HL-LHC           | High Luminosity Large Hadron Collider; pp. 2, 23–27, 29                          |
| HLT              | High Level Trigger; pp. 10   |
| I <sup>2</sup> C | Inter-Integrated Circuit; pp. 41, 44, 45   |

|         |  |
|---------|--|
| I/O     | Input and Output; pp. 39                                     |
| IEL     | Ionising Energy Loss; pp. 16                                 |
| KIT     | Karlsruhe Institute of Technology; pp. 78                    |
| L1      | Level-1 Trigger; pp. 10, 15, 27, 28, 33                      |
| L1A     | Level-1 Accept; pp. 28, 29, 31                               |
| LCIO    | Linear Collider I/O; pp. 60                                  |
| LEP     | Large Electron-Positron Collider; pp. 6                      |
| LGAD    | Low Gain Avalanche Detector; pp. 26                          |
| LHC     | Large Hadron Collider; pp. V, 1–3, 5–8, 15–18, 23–26, 42, 87 |
| LHCb    | Large Hadron Collider Beauty; pp. 7                          |
| LINAC   | Linear Accelerator; pp. 6, 24, 54                            |
| LIU     | LHC Injectors Upgrade; pp. 24                                |
| lpGBT   | Low Power Giga-Bit Transceiver; pp. 30, 36, 37, 45, 48, 49   |
| LUT     | Look-Up Table; pp. 39, 40, 47–49                             |
| MaPSA   | Macro-Pixel Sub Assembly; pp. 78, 79, 88                     |
| MCH     | $\mu$ TCA Control Hub; pp. 39                                |
| MIMOSA  | Minimum Ionising MOS Active pixel sensor; pp. 56, 57, 61     |
| MIP     | Minimum Ionising Particle; pp. 26                            |
| MPA     | Macro-Pixel ASIC; pp. 30, 37, 38, 46, 53, 78, 79, 81, 86–88  |
| MTD     | MIP Timing Detector; pp. 26                                  |
| MUX     | Multiplexer; pp. 40, 47, 49                                  |
| NIEL    | Non-Ionising Energy Loss; pp. 16                             |
| PC      | Personal Computer; pp. 39, 41, 42, 46, 47, 50                |
| PETRA   | Positron-Electron Tandem Ring Accelerator; pp. 53            |
| Ph2 ACF | CMS Phase 2 Acquisition and Control Framework; pp. 50        |
| PIAL    | Physical Interface Abstraction Layer; pp. 42, 44, 45         |
| PMT     | Photomultiplier Tube; pp. 58                                 |
| PS      | Proton Synchrotron; pp. 6, 24                                |
| PS      | Pixel-Strip Module; pp. 28–31, 37, 38, 78                    |

|       |   |
|-------|---|
| PSB   | Proton Synchrotron Booster; pp. 6, 24             |
| QCD   | Quantum Chromodynamics; pp. 4                     |
| QED   | Quantum Electrodynamics; pp. 4                    |
| QFT   | Quantum Field Theory; pp. 4                       |
| RAM   | Random Access Memory; pp. 40, 47, 49              |
| RMS   | Root Mean Square; pp. 62                          |
| RPC   | Resistive Plate Chambers; pp. 27                  |
| SEU   | Single Event Upset; pp. 16                        |
| SiPM  | Silicon Photomultiplier; pp. 26                   |
| SM    | Standard Model; pp. 3–5, 8, 23                    |
| SPS   | Super Proton Synchrotron; pp. 4, 6, 24            |
| SSA   | Short-Strip ASIC; pp. 30, 37, 38, 46, 78, 81, 87  |
| SUSY  | Super Symmetry; pp. 23                            |
| TCA   | Telecommunications Computing Architecture; pp. 42 |
| TCDS  | Trigger Distribution and Control System; pp. 43   |
| TEC   | Tracker End-Cap; pp. 19                           |
| TF    | Track Finder; pp. 28, 31, 32, 46, 49              |
| TFP   | Track Finding Processor; pp. 32, 33               |
| TIB   | Tracker Inner Barrel; pp. 19                      |
| TID   | Tracker Inner Disks; pp. 19                       |
| TLU   | Trigger Logic Unit; pp. 58, 89, 90                |
| TOB   | Tracker Outer Barrel; pp. 19                      |
| VHDCI | Very High Density Cable Interconnect; pp. 66      |
| VTRx+ | Versatile Link Plus Transceiver; pp. 30           |



# Bibliography

- [1] C. P. Alderfer. “An empirical test of a new theory of human needs”. *Organizational Behavior and Human Performance* 4.2 (1969), pp. 142–175. DOI: 10.1016/0030-5073(69)90004-x.
- [2] L. Evans and P. Bryant. “LHC Machine”. *JINST* 3 (2008). DOI: 10.1088/1748-0221/3/08/S08001.
- [3] CMS Collaboration. “The CMS experiment at the CERN LHC. The Compact Muon Solenoid experiment”. *JINST* 3 (2008).
- [4] M.Y. Hussein. “Higgs Boson Production at the LHC”. *Nuclear Physics B - Proceedings Supplements* 207-208 (2010), pp. 110–113. DOI: 10.1016/j.nuclphysbps.2010.10.029.
- [5] T. Arabatzis. “Cathode Rays”. *Compendium of Quantum Physics* (2009), pp. 89–92. DOI: 10.1007/978-3-540-70626-7\_27.
- [6] J. J. Thomson. “XL. Cathode Rays”. *The London, Edinburgh, and Dublin Philosophical Magazine and Journal of Science* 44.269 (1897), pp. 293–316. DOI: 10.1080/14786449708621070.
- [7] E. Rutherford. “The scattering of alpha and beta particles by matter and the structure of the atom”. *Phil. Mag. Ser. 6* 21 (1911), pp. 669–688. DOI: 10.1080/14786440508637080.
- [8] N. Bohr. “I. On the constitution of atoms and molecules”. *The London, Edinburgh, and Dublin Philosophical Magazine and Journal of Science* 26.151 (1913), pp. 1–25. DOI: 10.1080/14786441308634955.
- [9] M. Gell-Mann. “The Eightfold Way: A Theory of strong interaction symmetry”. *Office of Scientific and Technical Information* (1961). DOI: 10.2172/4008239.
- [10] G. Zweig. “An  $SU_3$  model for strong interaction symmetry and its breaking; Version 1”. *CERN-TH.401* (1964).
- [11] S. L. Glashow. “Partial Symmetries of Weak Interactions”. *Nucl. Phys.* 22 (1961), pp. 579–588. DOI: 10.1016/0029-5582(61)90469-2.
- [12] S. Weinberg. “A Model of Leptons”. *Phys. Rev. Lett.* 19 (1967), pp. 1264–1266. DOI: 10.1103/PhysRevLett.19.1264.
- [13] A. Salam. “Weak and Electromagnetic Interactions”. *Proceedings, 8th Nobel Symposium* C680519 (1968), pp. 367–377.

- [14] G. 't Hooft and M. J. G. Veltman. “Regularization and Renormalization of Gauge Fields”. *Nucl. Phys. B* 44 (1972), pp. 189–213. DOI: 10.1016/0550-3213(72)90279-9.
- [15] University of Zurich. “Standard Model” (2018). Accessed: 14.10.2019. URL: <https://www.physik.uzh.ch/en/researcharea/lhcb/outreach/StandardModel.html>.
- [16] M. E. Peskin and D. V. Schroeder. “An Introduction to quantum field theory”. *Addison-Wesley* (1995).
- [17] G. Arnison et al. “Experimental observation of isolated large transverse energy electrons with associated missing energy at  $s = 540$  GeV”. *Phys. Lett. B* 122.1 (1983), pp. 103–116. DOI: 10.1016/0370-2693(83)91177-2.
- [18] UA2 Collaboration. “Evidence for  $Z^0 \rightarrow e^+ e^-$  at the CERN anti-p p Collider”. *Phys. Rev. Lett. B* 129 (1983), pp. 130–140. DOI: 10.1016/0370-2693(83)90744-X.
- [19] Particle Data Group. “Review of Particle Physics”. *Phys. Rev. D* 98 (2018), p. 030001. DOI: 10.1103/PhysRevD.98.030001.
- [20] P.W. Higgs. “Broken Symmetries and the Masses of Gauge Bosons”. *Phys. Rev. Lett.* 13 (1964), pp. 508–509. DOI: 10.1103/PhysRevLett.13.508.
- [21] ATLAS Collaboration. “The ATLAS Experiment at the CERN Large Hadron Collider”. *JINST* 3 (2008), S08003–S08003. DOI: 10.1088/1748-0221/3/08/S08003.
- [22] CMS Collaboration. “Observation of a new boson at a mass of 125 GeV with the CMS experiment at the LHC”. *Phys. Rev. Lett. B* 716 (2012), pp. 30–61. DOI: 10.1016/j.physletb.2012.08.021. arXiv: 1207.7235 [hep-ex].
- [23] ATLAS Collaboration. “Observation of a new particle in the search for the Standard Model Higgs boson with the ATLAS detector at the LHC”. *Phys. Rev. Lett. B* 716 (2012), pp. 1–29. DOI: 10.1016/j.physletb.2012.08.020. arXiv: 1207.7214 [hep-ex].
- [24] K. Kodama et al. “Observation of tau neutrino interactions”. *Phys. Lett. B* 504.3 (2001), pp. 218–224. DOI: 10.1016/S0370-2693(01)00307-0.
- [25] S. Myers. “The LEP Collider, from design to approval and commissioning”. *CERN* (1991). DOI: 10.5170/CERN-1991-008.
- [26] J. Gruschke. “Observation of Top Quarks and First Measurement of the  $t\bar{t}$ - Production Cross Section at a Centre-Of-Mass Energy of 7 TeV with the CMS Experiment at the LHC”. *IEKP-KA-2011-04, CERN-THESIS-2011-030, CMS-TS-2011-009* (2011).
- [27] M. Benedikt et al. “LHC Design Report”. *CERN* (2004). DOI: 10.5170/CERN-2004-003-V-3.
- [28] M. Grazzini et al. “Higgs boson pair production at NNLO with top quark mass effects”. *JHEP* 05 (2018), p. 059. DOI: 10.1007/JHEP05(2018)059. arXiv: 1803.02463 [hep-ph].
- [29] ALICE Collaboration. “The ALICE experiment at the CERN LHC”. *JINST* 3 (2008), S08002. DOI: 10.1088/1748-0221/3/08/S08002.

- 
- [30] LHCb Collaboration. “The LHCb Detector at the LHC”. *JINST* 3 (2008), S08005. DOI: 10.1088/1748-0221/3/08/S08005.
- [31] CMS Collaboration. “Interactive Slice of the CMS detector”. *CMS-OUTREACH-2016-027* (2016).
- [32] CMS Collaboration. “The CMS tracker system project: Technical Design Report”. *CERN-LHCC-98-006* (1997).
- [33] CMS Collaboration. “The CMS tracker: addendum to the Technical Design Report”. *CERN-LHCC-2000-016* (2000).
- [34] CMS Collaboration. “CMS Technical Design Report for the Pixel Detector Upgrade”. *CERN-LHCC-2012-016* (2012).
- [35] CMS Collaboration. “The CMS electromagnetic calorimeter project: Technical Design Report”. *CERN-LHCC-97-033* (1997).
- [36] CMS Collaboration. “The CMS hadron calorimeter project: Technical Design Report”. *CERN-LHCC-97-031* (1997).
- [37] CMS Collaboration. “The CMS muon project: Technical Design Report”. *CERN-LHCC-97-032* (1997).
- [38] CMS Collaboration. “CMS TriDAS project: Technical Design Report, Volume 1: The Trigger Systems”. *CERN-LHCC-2000-038* (2000).
- [39] V. Gori. “The CMS high level trigger”. *International Journal of Modern Physics: Conference Series* 31 (2014), p. 1460297. DOI: 10.1142/s201019451460297x.
- [40] W. Pauli. “Über den Zusammenhang des Abschlusses der Elektronengruppen im Atom mit der Komplexstruktur der Spektren”. *Zeitschrift für Physik* 31.1 (1925), pp. 765–783. DOI: 10.1007/bf02980631.
- [41] P. P. Altermatt et al. “Reassessment of the intrinsic carrier density in crystalline silicon in view of band-gap narrowing”. *Journal of Applied Physics* 93.3 (2003), pp. 1598–1604. DOI: 10.1063/1.1529297.
- [42] W. Shockley. “Currents to Conductors Induced by a Moving Point Charge”. *Journal of Applied Physics* 9.10 (1938), pp. 635–636. DOI: 10.1063/1.1710367.
- [43] W. Snoeys. “CMOS monolithic active pixel sensors for high energy physics”. *Nucl. Instrum. Meth. Phys. Res. A* 765 (2014), pp. 167–171. DOI: 10.1016/j.nima.2014.07.017.
- [44] W.E. Price and J.R. Coss. “Single event phenomena: A summary”. *Nucl. Instrum. Meth. Phys. Res. B* 40-41 (1989), pp. 1306–1309. DOI: 10.1016/0168-583x(89)90645-9.
- [45] B. Verlaet, M. Van Beuzekom, and A. Van Lysebetten. “CO2 cooling for HEP experiments”. *CERN* (2008). DOI: 10.5170/CERN-2008-008.328.
- [46] L. Caminada. “Performance and operation of the CMS Phase 1 pixel detector”. *Nucl. Instrum. Meth. Phys. Res. A* (2018). DOI: 10.1016/j.nima.2018.10.084.

- [47] CMS Collaboration. “CMS Tracking POG Performance Plots For 2017 with PhaseI pixel detector” (2017). Accessed: 14.10.2019. URL: <https://twiki.cern.ch/twiki/bin/view/CMSPublic/TrackingPOGPerformance2017MC>.
- [48] G. Unal. “Higgs boson measurements at the LHC”. *Proceedings, 38th International Symposium on Physics in Collision (PIC 2018)* (2018). arXiv: 1811.10215 [hep-ex].
- [49] V. Khachatryan et al. “Observation of the rare  $B_s^0 \rightarrow \mu^+ \mu^-$  decay from the combined analysis of CMS and LHCb data”. *Nature* 522 (2014).
- [50] CMS Collaboration. “Measurement of  $t\bar{t}H$  production in the  $H \rightarrow b\bar{b}$  decay channel in  $41.5 \text{ fb}^{-1}$  of proton-proton collision data at  $\sqrt{s} = 13 \text{ TeV}$ ”. *CMS-PAS-HIG-18-030* (2019).
- [51] K. Hanke et al. “The LHC Injectors Upgrade (LIU) Project at CERN: Proton Injector Chain”. *Proceedings, 8th International Particle Accelerator Conference (IPAC 2017)* (2017), WEPVA036. DOI: 10.18429/JACoW-IPAC2017-WEPVA036.
- [52] G. Apollinari et al. “High-Luminosity Large Hadron Collider (HL-LHC): Technical Design Report V. 0.1”. *CERN* (2017).
- [53] B. Schmidt. “The High-Luminosity upgrade of the LHC: Physics and Technology Challenges for the Accelerator and the Experiments”. *Journal of Physics: Conference Series* 706 (2016), p. 022002. DOI: 10.1088/1742-6596/706/2/022002.
- [54] G. Apollinari et al. “High-Luminosity Large Hadron Collider (HL-LHC): Preliminary Design Report”. *CERN* (2015). DOI: 10.5170/CERN-2015-005.
- [55] CMS Collaboration. “Technical Proposal for the Phase-II Upgrade of the CMS Detector”. *CERN-LHCC-2015-010* (2015).
- [56] CMS Collaboration. “The Phase-2 Upgrade of the CMS Endcap Calorimeter”. *CERN-LHCC-2017-023* (2017).
- [57] CMS Collaboration. “The Phase-2 Upgrade of the CMS Barrel Calorimeters”. *CERN-LHCC-2017-011* (2017).
- [58] CMS Collaboration. “A MIP Timing Detector for the CMS Phase-2 Upgrade”. *CERN-LHCC-2019-003* (2019).
- [59] CMS Collaboration. “The Phase-2 Upgrade of the CMS Muon Detectors”. *CERN-LHCC-2017-012* (2017).
- [60] E. Brondolin. “Expected Performance of Tracking in CMS at the HL-LHC”. *EPJ Web of Conferences* 150 (2017), p. 00001. DOI: 10.1051/epjconf/201715000001.
- [61] CMS Collaboration. “The Phase-2 Upgrade of the CMS Tracker”. *CERN-LHCC-2017-009* (2017).
- [62] A. Harb, A. Mussgiller, and J. Hauk. “Test beam results of the first CMS double-sided strip module prototypes using the CBC2 read-out chip”. *Nucl. Instrum. Meth. Phys. Res. A* 845 (2017), pp. 93–96. DOI: 10.1016/j.nima.2016.06.027.

- 
- [63] A. Caratelli et al. “Short-Strip ASIC (SSA): A 65nm silicon-strip readout ASIC for the Pixel-Strip (PS) module of the CMS Outer Tracker detector upgrade at HL-LHC”. *Proceedings, Topical Workshop on Electronics for Particle Physics (TWEPP17)* (2018), p. 031. DOI: 10.22323/1.313.0031.
  - [64] D. Ceresa et al. “Macro Pixel ASIC (MPA): The readout ASIC for the pixel-strip (PS) module of the CMS outer tracker at HL-LHC”. *CMS-CR-2014-139* (2014).
  - [65] C. Soós et al. “Versatile Link PLUS transceiver development”. *JINST* 12.03 (2017), pp. C03068–C03068. DOI: 10.1088/1748-0221/12/03/c03068.
  - [66] R. Aggleton et al. “An FPGA based track finder for the L1 trigger of the CMS experiment at the High Luminosity LHC”. *JINST* 12.12 (2017), P12019–P12019. DOI: 10.1088/1748-0221/12/12/p12019.
  - [67] CMS Collaboration. “The Phase-2 Upgrade of the CMS L1 Trigger Interim Technical Design Report”. *CERN-LHCC-2017-013* (2017).
  - [68] T. James. “A hardware track-trigger for CMS at the High Luminosity LHC”. *CMS-TS-2018-025, CERN-THESIS-2018-241* (2018).
  - [69] M. Pesaresi et al. “The FC7 AMC for generic DAQ & control applications in CMS”. *JINST* 10.03 (2015), pp. C03036–C03036. DOI: 10.1088/1748-0221/10/03/c03036.
  - [70] W. Ferguson et al. “The CBC microstrip readout chip for CMS at the high luminosity LHC”. *JINST* 7 (2012). DOI: 10.1088/1748-0221/7/08/C08006.
  - [71] G. Hall et al. “CBC2: A CMS microstrip readout ASIC with logic for track-trigger modules at HL-LHC”. *Nucl. Instrum. Meth. Phys. Res. A* 765 (2014), pp. 214–218.
  - [72] CMS Tracker Collaboration. “Test beam demonstration of silicon microstrip modules with transverse momentum discrimination for the future CMS tracking detector”. *JINST* 13.03 (2018), P03003–P03003. DOI: 10.1088/1748-0221/13/03/p03003.
  - [73] CMS Collaboration. “Functional tests of 2S modules for the CMS Phase-2 Tracker Upgrade with a MicroTCA-based readout system”. *CMS-CR-2017-367* (2017).
  - [74] M. Prydderch et al. “CBC3: a CMS microstrip readout ASIC with logic for track-trigger modules at HL-LHC”. *Proceedings, Topical Workshop on Electronics for Particle Physics (TWEPP17)* (2018). DOI: 10.22323/1.313.0001.
  - [75] P. Moreira et al. “The GBT Project”. *Proceedings, Topical Workshop on Electronics for Particle Physics (TWEPP09)* (2009). DOI: 10.5170/CERN-2009-006.342.
  - [76] V. Bobillier et al. “MicroTCA and AdvancedTCA equipment evaluation and developments for LHC experiments”. *JINST* 11.02 (2016), pp. C02022–C02022. DOI: 10.1088/1748-0221/11/02/c02022.
  - [77] “IEEE Standard for Ethernet”. *IEEE* (2016). DOI: 10.1109/ieeestd.2016.7428776.
  - [78] Xilinx. “Kintex-7 FPGA Family” (2019). Accessed: 14.10.2019. URL: <https://www.xilinx.com/products/silicon-devices/fpga/kintex-7.html#productTable>.

- [79] National Instruments. “FPGA Fundamentals” (2019). Accessed: 14.10.2019. URL: <https://www.ni.com/de-de/innovations/white-papers/08/fpga-fundamentals.html>.
- [80] NXP Semiconductors. “UM10204 I2C-bus specification and user manual” (2014). Accessed: 14.10.2019. URL: <https://www.nxp.com/docs/en/user-guide/UM10204.pdf>.
- [81] C. Ghabrous Larrea et al. “IPbus: a flexible Ethernet-based control system for xTCA hardware”. *JINST* 10.02 (2015), pp. C02019–C02019. DOI: 10.1088/1748-0221/10/02/c02019.
- [82] E. Hazen et al. “The AMC13XG: a new generation clock/timing/DAQ module for CMS MicroTCA”. *JINST* 8.12 (2013), pp. C12036–C12036. DOI: 10.1088/1748-0221/8/12/c12036.
- [83] CERN Open Hardware Repository. “DIO5” (2012). Accessed: 14.10.2019. URL: <https://www.ohwr.org/project/fmc-dio-5chtla/wikis/home>.
- [84] Xilinx. “UltraScale+ FPGA Family” (2019). Accessed: 14.10.2019. URL: <https://www.xilinx.com/products/silicon-devices/fpga/kintex-ultrascale-plus.html#productTable>.
- [85] G. Hemmie. “DESY II, a New Injector for the Desy Storage Rings PETRA and DORIS II”. *IEEE Transactions on Nuclear Science* 30.4 (1983), pp. 2028–2030. DOI: 10.1109/tns.1983.4332706.
- [86] W. Ebeling and J. R. Maidment. “The proton synchrotron DESY III”. *Proceedings, 17th IEEE Particle Accelerator Conference (PAC 97)* C970512 (1997), pp. 985–987.
- [87] DESY. “HERA - A Proposal for a Large Electron Proton Colliding Beam Facility at DESY”. *DESY-HERA-81-10* (1981).
- [88] R. Diener et al. “The DESY II test beam facility”. *Nucl. Instrum. Meth. Phys. Res. A* 922 (2019), pp. 265–286. DOI: 10.1016/j.nima.2018.11.133.
- [89] K. Balewski et al. “PETRA III: A low emittance synchrotron radiation source. Technical design report”. *DESY-2004-035* (2004).
- [90] DESY. “Beam generation at DESY II facility” (2019). Accessed: 14.10.2019. URL: [http://particle-physics.desy.de/test\\_beams\\_at\\_desy/beam\\_generation/index\\_ger.html](http://particle-physics.desy.de/test_beams_at_desy/beam_generation/index_ger.html).
- [91] DESY. “EUDET-type beam telescopes, Main Page” (2019). Accessed: 14.10.2019. URL: [https://telescopes.desy.de/Main\\_Page](https://telescopes.desy.de/Main_Page).
- [92] H. Jansen et al. “Performance of the EUDET-type beam telescopes”. *EPJ Tech. Instrum.* 3.1 (2016), p. 7. DOI: 10.1140/epjti/s40485-016-0033-2. arXiv: 1603.09669 [physics.ins-det].
- [93] J. Baudot et al. “First test results Of MIMOSA-26, a fast CMOS sensor with integrated zero suppression and digitized output”. *IEEE Nuclear Science Symposium Conference Record (NSS/MIC)* (2009). DOI: 10.1109/nssmic.2009.5402399.

- 
- [94] S. Spannagel. “Test Beam Measurements for the Upgrade of the CMS Pixel Detector and Measurement of the Top Quark Mass from Differential Cross Sections”. *DESY-THESIS-2016-010* (2016). DOI: 10.3204/desy-thesis-2016-010.
- [95] S. Spannagel. “Status of the CMS Phase I pixel detector upgrade”. *Nucl. Instrum. Meth. Phys. Res. A* 831 (2016), pp. 71–75. DOI: 10.1016/j.nima.2016.03.028.
- [96] D. Cussans. “Description of the JRA1 Trigger Logic Unit (TLU), v0.2c”. *EUDET-MEMO-2009-04* (2009).
- [97] G. Claus et al. “IPHC & NI Flex RIO DAQ for EUDET Mimosa 26 Beam Telescope”. *EUDET-Memo-2010-25* (2010).
- [98] S. Spannagel, B. Meier, and H. Perrey. “The pxarCore Library - Technical Documentation, Reference Manual, and Sample Applications”. *CMS-NOTE-2016-001* (2015).
- [99] H. Perrey. “EUDAQ and EU Telescope: Software Frameworks for Test Beam Data Acquisition and Analysis”. *Proceedings, 3rd International Conference on Technology and Instrumentation in Particle Physics (TIPP 2014)* (2014), p. 353. DOI: 10.22323/1.213.0353.
- [100] R. Brun and F. Rademakers. “ROOT — An object oriented data analysis framework”. *Nucl. Instrum. Meth. Phys. Res. A* 389.1-2 (1997), pp. 81–86. DOI: 10.1016/S0168-9002(97)00048-X.
- [101] DESY. “About EU Telescope” (2019). Accessed: 14.10.2019. URL: <http://eutelescope.web.cern.ch/content/about-eutelescope>.
- [102] DESY. “LCIO Homepage” (2016). Accessed: 14.10.2019. URL: <http://lcio.desy.de/>.
- [103] R. Turchetta. “Spatial resolution of silicon microstrip detectors”. *Nucl. Instrum. Meth. Phys. Res. A* 335.1-2 (1993), pp. 44–58. DOI: 10.1016/0168-9002(93)90255-G.
- [104] DESY. “GEAR Homepage” (2007). Accessed: 14.10.2019. URL: [http://ilcsoft.desy.de/portal/software\\_packages/gear/](http://ilcsoft.desy.de/portal/software_packages/gear/).
- [105] C. Kleinwort. “General broken lines as advanced track fitting method”. *Nucl. Instrum. Meth. Phys. Res. A* 673 (2012), pp. 107–110. DOI: 10.1016/j.nima.2012.01.024.
- [106] V. Blobel. “A new fast track-fit algorithm based on broken lines”. *Nucl. Instrum. Meth. Phys. Res. A* 566.1 (2006), pp. 14–17. DOI: 10.1016/j.nima.2006.05.156.
- [107] V. Blobel, C. Kleinwort, and F. Meier. “Fast alignment of a complex tracking detector using advanced track models”. *Computer Physics Communications* 182 (2011). DOI: 10.1016/j.cpc.2011.03.017.
- [108] D. Braga. “Development of the readout electronics for the high luminosity upgrade of the CMS outer strip tracker”. *Braga-D-2016-PhD-Thesis* (2016).
- [109] S. Spannagel and H. Jansen. “GBL Track Resolution Calculator v2.0” (2016). Accessed: 14.10.2019. URL: <http://doi.org/10.5281/zenodo.48795>.

- [110] ATLAS Collaboration. “Operation and performance of the ATLAS semiconductor tracker”. *JINST* 9.08 (2014), P08009–P08009. DOI: 10.1088/1748-0221/9/08/p08009.
- [111] CERN. “Macro-Pixel ASIC Specifications” (2016). Accessed: 23.10.2019. URL: [https://espace.cern.ch/CMS-MPA/SiteAssets/SitePages/Documents/MPA\\_specs\\_V1\\_1.pdf](https://espace.cern.ch/CMS-MPA/SiteAssets/SitePages/Documents/MPA_specs_V1_1.pdf).



# Acknowledgements

This thesis would not be possible without a group of people who helped, supported and inspired me. Among them, I would like to express my special gratitude to my supervisor, Dr. Andreas Mußgiller. From the very beginning, I have gotten the freedom in research along with the courteous, honest and fair steering from his side. I appreciate this very much, as well as the time he had spent helping improve this manuscript. I am also very thankful to Prof. Dr. Elisabetta Gallo for reading the thesis and supporting me in the final submission steps.

Thank you, my project colleagues: Dr. Alessandro Caratelli, Dr. Davide Ceresa, Jarne De Clercq, Dr. Thomas Eichhorn, Dr. Stefano Mersi, Dr. Sarah Seif El Nasr-Storey and many others. The time that I have spent working with you was very interesting, pleasant and entertaining. You are all brilliant and inspiring people and I wish to stay in contact with you.

I am grateful to these brave and patient people who expressed their interest in reading and reviewing my thesis: Dr. Doris Eckstein, Prof. Dr. Elisabetta Gallo, Dr. Moritz Guthoff, Dr. Ali Harb, Dr. Andreas Mußgiller, Dr. Sarah Seif El Nasr-Storey, Andrej Saibel and Dr. Paul Schütze. I have learned a lot from you during the time of writing.

During these years, I have acquired a lot of close friends. They were supporting me and made the time here unforgettable. Special credit goes to my girlfriend Liubov, to my close friends Anastasia, Illia, Mykola, Oleksandr, Oleksii and Rustam, and my flatmate Antonio. We have had a lot of great moments, let it continue like this.

I would also like to mention my close university friends: Andrii, Daniil, Ivan and Oleksii. I am very glad that we are still in touch and meet together, even though not as often as I wish.

Last but not least, it is hard to express these warm feelings and gratitude to my family. My parents, my grandparents, my aunts and my cousins - they have always been there to talk to me and to teach me the most important things that I know. You made me the person that I am.